SPATIAL AND TEMPORAL VARIABILITY OF LATENT HEATING IN THE TROPICS USING TRMM OBSERVATIONS

by

Tracey A. Dorian

A thesis submitted in partial fulfillment of

the requirements for the degree of

Master of Science

(Atmospheric and Oceanic Sciences)

at the

UNIVERSITY OF WISCONSIN-MADISON

2014

Declaration of Authorship

I, Tracey A. Dorian, declare that this thesis titled, ' SPATIAL AND TEMPORAL VARIABILITY OF LATENT HEATING IN THE TROPICS USING TRMM OBSERVATIONS' and the work presented in it are my own.

Tracey A. DORIAN
Author

Signature

I hereby approve and recommend for acceptance this work in partial fulfillment of the requirements for the degree of Master of Science:

Dr. Tristan S. L'ECUYER
Committee Chair

Signature

Dr. Larissa E. BACK
Faculty Member

Signature

Dr. Daniel J. VIMONT
Faculty Member

Signature

Abstract

Tropical rainfall is estimated to make up $\frac{2}{3}$ of global rainfall yet the factors that govern its spatial distribution and diurnal and seasonal variations are still not completely understood. Because of these uncertainties, it is a challenge for global climate models (GCMs) to accurately represent rainfall and to predict future changes in rainfall. Since rainfall variability is intimately connected to the microphysical processes and associated latent heat released in the formation of rain, an improved understanding of these processes may provide valuable insights for improving the representation of tropical rainfall in models. This research utilizes Tropical Rainfall Measuring Mission (TRMM) satellite estimates of atmospheric latent heating rates from 1998 to 2010 to explore the vertical structure of latent heating in precipitating regions. In particular, we seek to understand how heating structures vary regionally, seasonally, and diurnally. By applying Fourier Transform Analysis to the 13-year dataset, we find amplitudes that represent the strength of the diurnal cycle of the total integrated latent heating and phases that represent the local time of day when maximum latent heat release occurs. A similar analysis is applied to land regions using a separate dataset that uses TRMM precipitation radar observations.

Acknowledgements

I would like to thank Dr. Tristan L'Ecuyer for the opportunity to complete this research. His guidance has proven invaluable to me and I am very appreciative of his helpful advice and continued support. I am very appreciative of the constructive feedback and recommendations that I received from the two professors who reviewed my thesis, Dr. Larissa Back and Dr. Dan Vimont. I would also like to acknowledge my entire research group, particularly Mark Smalley for his assistance in programming. I would like to recognize the RADARS-UW group for providing valuable insight and useful suggestions for the interpretation and presentation of my results. This research would not have been possible without the Atmospheric and Oceanic Sciences Department of University of Wisconsin-Madison. I am especially grateful to the NASA Energy and Water Cycle Sponsored Research Program (NEWS) for the availability of their data. Finally, I would like to express gratitude to my parents and family for their endless support and encouragement during the various stages of my education, particularly during my graduate school studies.

Contents

Abbreviations

APE	**A**vailable **P**otential **E**nergy
CERES	**C**louds and **E**arth's **R**adiant **E**nergy **S**ystem
DPR	**D**ual-**F**requency **P**recipitation **R**adar
ENSO	**E**l-**N**iño **S**outhern **O**scillation
GCM	**G**lobal **C**limate **M**odel
GMI	**G**PM **M**icrowave **I**mager
GPM	**G**lobal **P**recipitation **M**easurement
HERB	**H**ydrologic **C**ycle and **E**arth's **R**adiative **B**udget
ITCZ	**I**nter-**T**ropical **C**onvergence **Z**one
JAXA	**J**apan **A**erospace E**x**ploration **A**gency
LIS	**L**ightning **I**maging **S**ensor
MCS	**M**esoscale **C**onvective **S**ystem
MJO	**M**adden-**J**ulian **O**scillation
NASA	**N**ational **A**eronautics and **S**pace **A**dministration
NEWS	**N**ASA's **E**nergy and **W**ater Cycle **S**tudy
NEXRAD	**Nex**t Generation Weather **Rad**ar
NH	**N**orthern **H**emisphere
PR	**P**recipitation **R**adar
SH	**S**outhern **H**emisphere
SLH	**S**pectral **L**atent **H**eating
SPCZ	**S**outh **P**acific **C**onvergence **Z**one
SSM/I	**S**pecial **S**ensor **M**icrowave **I**mager
SST	**S**ea **S**urface **T**emperature
TMI	**T**RMM **M**icrowave **I**mager
TRMM	**T**ropical **R**ainfall **M**easuring **M**ission
UTC	**C**oordinated **U**niversal **T**ime
VIRS	**V**isible **I**nfra**r**ed **S**canner

Chapter 1

Introduction

1.1 Motivation

Excess heat and energy in the tropics trigger atmospheric and oceanic heat transport poleward so that the tropics do not continually heat up. Latent heating is the primary source for the tropical convective heat engine since heat is released into the atmosphere via the formation of precipitation (Reihl and Malkus, 1958). Precipitation drives the hydrologic cycle and plays an important role in influencing weather and climate around the world through the release of tremendous amounts of latent heat energy into the atmosphere. The tropics account for roughly $\frac{2}{3}$ of global precipitation, which makes the tropics one of the

most energetic regions on the planet. Even today, rainfall is challenging to monitor and model because of its large spatial and temporal variability. Based on climatological records, the heaviest rainfall in the tropics tends to occur in the Inter-Tropical Convergence Zone (ITCZ), the South-Pacific Convergence Zone (SPCZ), the western Pacific, and southeast Asia. It is estimated that about $\frac{3}{4}$ of the energy that drives atmospheric circulation originates from the latent heat that is released by precipitation in the tropics (Kummerow and coauthors, 2000).

Latent heating is thought to play a very important role in weather and climate; for example, the propagation speed of the Madden-Julian Oscillation (MJO) is thought to depend critically on the level of maximum latent heating (Lau and Peng, 1987). Additionally, latent heating is responsible for the creation of available potential energy (APE), and is directly related to the horizontal wind divergence as well as to vertical motion (Tao and coauthors, 2006). The atmospheric response to heating is sensitive to the vertical structure of latent heating (Schumacher et al., 2004), that is, it is the vertical distribution of diabatic heating and not surface rainfall that drives atmospheric circulation (Tao and coauthors, 2006). For example, the vertical gradient in diabatic heating is directly proportional to the generation of potential vorticity in the tropics (Schumacher et al., 2004). The Walker Circulation, a steady zonal tropical circulation, is thought to be sensitive to the assumed vertical distribution of latent heating (Grecu et al., 2009). In general, it is well known that variations in the vertical

structures of diabatic heating result in changes in the dynamical "response" to that heating (Schumacher et al., 2004).

Global climate models (GCMs) used to predict future changes in rainfall require both rainfall estimates and the associated vertical profiles of latent heating estimates for verification, and for this reason it is important to accurately represent the vertical diabatic heating structure in GCMs in order to increase the model's reliability. Despite the vast improvements in estimating tropical rainfall from satellite observations, it is still a challenge to observe tropical rainfall because it varies greatly in both time and space. In fact, the standard deviation of monthly rainfall amounts in some tropical regions is estimated to be comparable to the mean value (Simpson et al., 1988). Furthermore, latent heating and rainfall cannot be observed directly from satellite observations, but must be estimated based on available satellite measurements such as brightness temperatures or reflectivities. GCMs have been shown to be very sensitive to the profiles of latent heating, especially in the tropics (Hartmann et al., 1984). In fact, recent studies suggest that GCMs exhibit biases in the representation of tropical clouds and rainfall and their variation and struggle to accurately predict the amounts of heat that are being released into the atmosphere. In particular, the physical understanding of the diurnal cycle of precipitation and convective intensity is currently limited, and numerical model simulation deficiencies do not allow for an accurate representation of the diurnal cycle of precipitation

(Nesbitt and Zipser, 2003). It is anticipated that more realistic depictions of diabatic heating profiles in numerical models could provide constraints on several aspects of climate model physics and could help to improve the prediction of rainfall events.

1.2 Past Studies

There have been numerous studies that involved latent heating algorithms to estimate heating profiles using measurements from satellites. Tao et al (2001), for example, used separate algorithms to approximate the heating profiles for February 1998 using Tropical Rainfall Measuring Mission satellite (TRMM) rainfall observations for the first time. He found agreement in the magnitude and distribution of maximum heating profiles but found differences in the altitudes of heating maxima between the models (Tao et al., 2001). In another study, a convective-stratiform classification based on surface rain rates was used to estimate vertical latent heating profiles (Tao et al., 1993). The conclusions of that study were that large-scale models need both global surface rainfall patterns as well as the associated vertical distribution. Another conclusion of that study was that the vertical distributions of heating in stratiform regions are very different from the profiles in convective regions of mesoscale convective systems (MCSs) (Tao et al., 1993). El-Nino Southern Oscillation (ENSO) also plays an

important role in tropical latent heat distribution because of the changes in observed stratiform rain fraction as seen from TRMM Precipitation Radar (PR) data (Schumacher et al., 2004). Other studies on atmospheric diabatic heating profile estimates have been on regional scales and have involved in-situ sounding networks and field campaigns (e.g. Reed and Recker 1971; Frank 1996; Zhang et al, 2001; Johnson and Cielieski, 2002). Diabatic heating estimates on global scales have until recently mainly relied on global climate models and reanalyses (e.g. Negri et al, 2002; Ling 2012) (L'Ecuyer and McGarragh, 2010).

The diurnal cycle of rainfall in the tropics has also been studied to try to understand the factors that govern changes throughout the day. Using measurements from the TRMM Precipitation Radar (PR) and the TRMM Microwave Imager (TMI) from December 1997 to November 2000, Nesbitt et al (2003) not only found differences between tropical land and ocean diurnal cycles, but also regional differences in the rainfall diurnal cycle over multiple ocean regions. In the same study, they used calculated amplitudes and phases from a Fourier fit function to concisely characterize the diurnal cycle characteristics for different areas (Nesbitt and Zipser, 2003). The explanation for the observed diurnal cycles in precipitation over open oceans remains relatively unknown, likely due to the lack of direct observations over oceans and also because of the smaller diurnal cycles over ocean as compared to land (Nesbitt and Zipser, 2003). They also discovered that there seems to be a maximum in total rainfall near sunrise

around 6am local time over ocean regions and that this early morning maximum is likely due to an increase in the number of systems, and not due to an actual increase in the rain rates within the systems (Nesbitt and Zipser, 2003).

1.3 This Study

In this study, diabatic heating estimates are derived from an algorithm and are based on 13 years of satellite data from the TRMM PR and TMI instruments between 1998 and 2010, which provides a period of sufficient sampling. This research is unique in that the global datasets of diabatic heating estimates come exclusively from satellite observations. Prior to this dataset, atmospheric heating has been estimated on regional scales using information from sounding networks (Johnsons and Cieielski 2002, and Zhang et al 2001). The TRMM satellite is a joint mission between the National Aeronautics and Space Administration (NASA) and the Japan Aerospace Exploration Agency (JAXA) and was launched in November 1997. The satellite is still transmitting information down to Earth today, but has recently been joined by the more advanced Global Precipitation Measurement (GPM) satellite. TRMM was boosted in August 2001 from an altitude of 350 km to 402.5 km in order to save fuel and prolong the mission. At its new altitude, TRMM revisits a given area at the same local time

roughly every 47.5 days, which changed from the 46.4 days that it previously required (Negri et al., 2002).

Taking advantage of TRMM's sampling of the complete diurnal cycle every 47 days, eight pre-defined 47-day periods are created for each of the 13 years between 1998 and 2010 and are later combined for each individual period. The main focus of this study is on these 47-day periods to examine both the seasonal cycle of tropical diabatic heating as well as the diurnal cycle variations. Specifically, this research analyzes both the differences in the diabatic heating distribution and the variations in time over various land and ocean regions in the tropics and subtropics. Differences in the diurnal cycle between seasons and regions are examined by calculating amplitude fractions (amplitude divided by mean values over a grid box) and phases from a Fourier transform fit, both of which succinctly describe the diurnal cycles and will be further explained in the *Methods* section. The goal of the study is to better understand the diurnal cycle of diabatic heating and perhaps even the physical processes that could be influencing changes in diabatic heating. By better understanding these processes, the processes could be better represented in global climate models, which have a difficult time reproducing the spatial distribution of tropical clouds and precipitation and are believed to have systematic biases.

Chapter 2

Data and Methodology

2.1 Tropical Rainfall Measuring Mission (TRMM)

The Tropical Rainfall Measuring Mission (TRMM) satellite's primary purpose has been to study tropical rainfall variation in both time and space. Tropical rainfall variation, before TRMM data became available, was poorly understood and modeled due to diverse rainfall estimates from both infrared and microwave algorithms (Kummerow and coauthors, 2000). In fact, it is estimated that the errors in tropical rainfall decreased from 50% to 20% after TRMM was launched (TRM, 2006). Tropical rainfall is the product of the release of latent heat into the atmosphere during condensation. Therefore, integrated latent heating is a proxy to surface rainfall. Another objective of TRMM has been

to determine the intensity and three-dimensional structure of latent heating in the tropics (Hou et al., 2014). Vertical latent heating structures have been estimated on global scales from global climate models and renanalyses or on regional scales from spatially and temporally limited radiosonde networks before TRMM observations were readily available. Other estimates of diabatic heating profiles have been derived from calculations of the apparent heating from sounding wind and temperature data using the dry static energy budget, or as a residual of the heat budget (Ling and Zhang, 2013).

The TRMM satellite, which has been referred to as "the flying rain gauge", was launched on November 27, 1997 and was planned for a 3-year mission (Simpson et al., 1988). TRMM covers latitudes between 38°S and 38°N and is located above Earth's surface at an altitude of 402.5 km with an inclination of 35° to Earth's equatorial plane. Studies have been conducted on possible effects of the August 2001 boost on TMI and PR measurements. For example, DeMoss et al (2007) found that the TMI instrument was biased low relative to gauges during the preboost period, but the bias was essentially zero during the postboost period. For the PR, they found that the radar was biased significantly low relative to the gauges during both boost periods, but that the change from pre to post boost period was not statistically significant (DeMoss and Bowman, 2007). TRMM's precessing orbit samples the complete diurnal cycle approximately every 47 days. The low-inclination was specifically chosen to improve

the sampling of the tropics and to allow the satellite to visit locations during different local times of day (Negri et al., 2002). TRMM orbits Earth about 16 times per day and each orbit takes approximately 90 minutes. TRMM has five instruments onboard including the TRMM Microwave Imager (TMI), the Precipitation Radar (PR), the Visible Infrared Scanner (VIRS), the Lightning Imaging Sensor (LIS), and the Clouds and Earth's Radiant Energy System (CERES). The primary instruments for measuring rainfall are the TMI, PR, and VIRS, and all three instruments provide measurements that are complementary. The focus of this research is on rainfall and latent heating estimates generated from TMI and PR observations. The PR and TMI can both provide estimates of the convective and stratiform components of rain rates that are central to approximating the vertical latent heating structures (Hou et al., 2014).

2.2 TRMM Microwave Imager (TMI)

The TRMM microwave imager is a multi-frequency passive microwave sensor that measures water vapor, cloud water content, rainfall intensity, and other non-hydrological parameters such as sea surface temperature and ocean surface wind speeds. The instrument consists of a 9-channel, 5-frequency, elliptically-scanning passive radiometer with a swath width of 878 km that provides sufficient daily global sampling. It is the broad sampling of the TMI that makes it the

"workhorse" of the rain-measuring package on TRMM. However, TMI's wider swath leads to a lower spatial resolution than what would be with a narrower swath. There have been instruments similar to the TMI from satellites prior to TRMM, such as the SSM/I, but the TMI provides higher resolution data measurements than the SSM/I because of the lower altitude of TRMM's orbit, and also has an additional 10.7 GHz channel designed to provide increased sensitivity to the higher rain rates found in the tropics (TMI, 2011). Because the TMI brightness temperatures are a function of surface emissivity, the microwave imager has an inherent difficulty in measuring atmospheric water vapor and rainfall over land surfaces due to the high and variable emissivities of land. The challenge lies in the inability of the microwave imager to distinguish between the signals of rainfall and the land surface due to the lack of contrast between their emissivities. Over the oceans, the microwave imager can more easily detect precipitation because the underlying ocean emits only about half of what it absorbs and therefore serves as a "cold" background to the "warmer" atmospheric rainfall. Over land surfaces it is necessary to use higher frequency microwaves, about 85 GHz, to measure ice scattering at the top of raining clouds in order to detect precipitation. Consequently, latent heating estimates from the TMI are currently only available over land surfaces imposing a similar restriction on the analysis that follows.

2.3 Precipitation Radar (PR)

The precipitation radar is an active sensor that provides more detailed information on the vertical structure of a storm than the microwave imager provides. The radar measures the distribution and intensity of rain, rain type, storm depth, melting layer, and precipitation-top height. The radar instrument was built by Japan and is the most innovative instrument onboard TRMM as it is the first radar dedicated to measuring rainfall from space. The instrument operates at 13.8 GHz, a radar frequency that is about four times higher than that of a typical ground-based radar (i.e. NEXRAD). The PR has a swath width at the surface of about 247 km, which is much more narrow than the TMI swath width (about $\frac{1}{3}$ the width). The narrow swath provides higher spatial resolution data, but with poorer sampling than the TMI provides. The spatial resolution of the PR was 4.3 km before the boost in August 2001 and is now approximately 5 km. As is demonstrated in Figure 2.1, it takes about three days for the precipitation radar to cover the global tropics, whereas it takes only about one day for the passive microwave imager. The complementary characteristics of the TMI (better sampling) and the PR (higher spatial resolution and accuracy) provide the motivation to analyze and compare latent heating estimates from both instruments in this study.

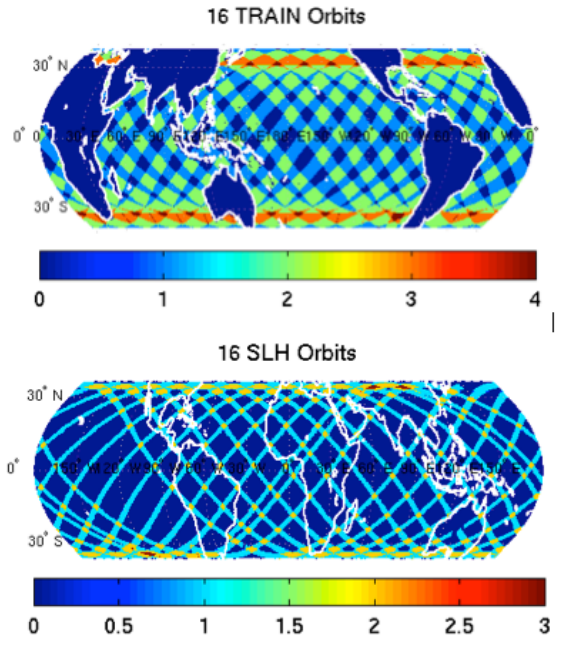

FIGURE 2.1: Satellite coverage for January 13, 1998 represented by total number of observations for the TMI (top) and the PR (bottom).

2.4 TRAIN Algorithm

The dataset used in this research was created based on TMI observations over 13 years of data since TRMM's launch in November 1997. The dataset includes retrievals of clouds and precipitation, which are then used in two different algorithms to approximate the vertical profiles of atmospheric radiative heating and latent heating, the two major sources of diabatic heating in the atmosphere. The database is produced starting with information from the precipitation radar such as rain rates, stratiform proportions, and echo tops for heating. This information is combined with consistent diabatic heating profiles from heating lookup tables produced from cloud model simulations to estimate

rain rates and heating profiles. These estimated rain rates and heating rates are then collocated with TMI radiances and put into a training database within the TRAIN algorithm to produce the final estimates of rain rates and heating profiles. Consequently, the TMI algorithm is referred to as "TRAIN" because it is trained to find the best estimates of rainfall and diabatic heating profiles based on the PR information using a Bayesian-estimation approach. The motivation behind such a procedure is that the PR has higher resolution but limited sampling compared to that of the TMI. The approach therefore allows the TMI observations to help extend the PR sampling to the broader TMI swath. The latent heating rates estimated in this latent-heating product only apply to precipitating regions. Another algorithm called Hydrologic Cycle and Earth's Radiation Budget (HERB) derives the radiative contribution of heating in both precipitating and non-precipitating regions through the vertical profile of radiative heating, however this analysis focuses on data originating from the TRAIN algorithm.

The TRAIN dataset (which may also be referred to as the Q1 or TMI dataset in this paper) includes data between 38°S to 38°N and 0°E to 359.5°E every 0.5°. The heating estimates are instantaneous, spatial averages based on TMI rainfall estimates over 0.5° x 0.5° grid boxes. The individual 0.5° x 0.5° box averages have considerable random error, and so it was necessary to perform spatial and temporal averaging of instantaneous half-degree grid box heating estimates. In

fact, within NASA's Energy and Water Cycle Study (NEWS) product overview, it is stated that even 0.5° x 0.5° grid box averages of TMI estimates have considerable error that can be as high as 100% for light rain rates. For this reason, the creators of the dataset recommend spatial and temporal averaging of the data to at least monthly scales to obtain more statistically-reliable results. Additionally, it is important to note that the TRAIN algorithm does not include warm shallow convection. The producers of the dataset caution that the algorithm may have convective biases in the lower troposphere and in lighter rain, which is particularly prevalent in the Eastern Pacific where frequent shallow warm convection is observed (Grecu et al., 2009). In general, because there is not a 1:1 relationship between brightness temperatures and latent heating, there are uncertainties in the estimates of latent heating from the TRAIN algorithm. The uncertainties derive from the non-unique relationship between surface rain rate and the ice-scattering signature in the strongly-coupled 37 GHz and 85 GHz brightness temperatures (L'Ecuyer and Stephens, 2002). The same study describes how brightness temperatures themselves are sensitive to errors in sea-surface temperature (SST), surface wind speed, and column water vapor (L'Ecuyer and Stephens, 2002). Despite the uncertainties, the estimates of latent heating are essential to study since they derive from global observations and not exclusively from GCMs.

There are some known data gaps in the TRMM record – the longest stretch

of missing data in the TRAIN dataset is between September 5, 2002 and October 16, 2002. As noted previously, the TRAIN dataset does not have any data available over continents due to the lack of sensitivity of the passive microwave radiances to precipitation over land. The latest version of the data files (V1.1) were generated on April 3, 2010, and are arranged orbit by orbit. The files contain multiple profiles that make up portions of one satellite orbit. Each individual profile contains latitude and longitude coordinates, the date and time in Coordinated Universal Time (UTC) of the observations, the number of TMI footprints in the grid box, and the total and stratiform rain rates. Additionally, the solar flux (Wm^{-2}) and cloud information that was used in the calculations of radiative heating are included, followed by convective boundary layer calculations. Finally, liquid water content (gm^{-3}), total diabatic heating ($Khour^{-1}$), radiative heating ($Khour^{-1}$), stratiform latent heating ($Khour^{-1}$), and sensible heating ($Khour^{-1}$) are reported on 29 atmospheric levels from the surface to 18 km. The 29 levels listed in the data files are in order of descending height every 1 km from 18 km down to 10 km and then every 0.5 km from 10 km down to the surface. Variables that are not reported on levels are latitude, longitude, time, TMI footprints, rain rate, stratiform rain rate, incident solar flux, diurnally-averaged solar flux, number of clear, high-cloud, low-cloud, high-and-low-cloud, and raining elements, surface altitude, and boundary-layer top altitude. With the available data, it was possible to calculate convective latent heating, total latent

heating, fractions of convective and stratiform latent heating or rain rates, fraction of high and low clouds, and more, although the analysis presented below focuses on latent heating.

The first step in approaching the TRAIN atmospheric diabatic heating dataset was to convert all of the UTC times to local time integer values based on longitudes within each profile of the full orbit swath. Data were gridded into integer hour bins between 0 and 24, where Hours 0 and 24 correspond to midnight, and Hour 12 corresponds to noon. The next step was to convert all of the latitudes into latitude indices between 1 and 154 by adding 38.25° to the raw latitudes in the files, and then dividing by 0.5°. For the longitudes, the raw longitudes within the files were divided by 0.5° to create longitude indices between 1 and 720. A counter variable was generated in order to monitor each time a new observation was found for a specific combination of indices. Data were then summed based on those indices into the eight 47-day periods (defined in Table 2.1) for each year between 1998 and 2010 since, as previously stated, the diurnal precession rate of TRMM is approximately 47 days. Once the data were combined for 13 years of each individual period, averages were calculated by dividing those sums by the counter variable that was created. Period 1 starts on January 13th instead of January 1st so that the seasons could be better captured within the eight periods. There was a slight overlap of Period 8 into Period 1 for January 13-23; this was done purposely to include the first 12 days of January

in the summations and to stay consistent with the 47-day periods. Period 8 in 2010 included data from December 8 to December 31 and data from January 1 to January 23 in 1998 so that the data essentially started and ended with the same time period. Finally, it is important to note that during leap years the eight periods were defined very similarly, but offset by one day. The reason behind organizing the data into these eight periods was to examine both the diurnal cycle and the seasonal cycle of rainfall and latent heating.

TABLE 2.1: User-created 47-day periods that cover every day of the year for years 1998-2010. These same exact periods were used for every year from 1998 to 2010, but the 8th period in 2010 goes from December 8, 2010 back to January 23rd of 1998.

Period 1	January 13-February 28
Period 2	March 1-April 16
Period 3	April 17-June 2
Period 4	June 3-July 19
Period 5	July 20-September 4
Period 6	September 5-October 21
Period 7	October 22-December 7
Period 8	December 8-January 23

2.5 Spectral Latent Heating (SLH) Algorithm

Another dataset of diabatic heating estimates was produced by an algorithm called the Spectral Latent Heating (SLH) algorithm. This particular dataset uses precipitation radar information using model-generated look-up tables for both land and ocean regions (Shige et al., 2007). The information taken from the

precipitation radar includes convective and stratiform classification, precipitation-top height, surface precipitation rates, the melting layer, and more. There are heating profile look-up tables for three different rain categories – convective, shallow stratiform, and anvil rain, which is essentially deep stratiform with a melting level. As a reminder, the dataset derived from the TRAIN algorithm does not include shallow convection. The three rain categories for the SLH algorithm are derived from tropical cloud simulations, which were generated by a cloud-resolving model. For convective and shallow stratiform rain types, the look-up table based on precipitation-top height was used. For anvil rain, however, the precipitation radar has a difficult time observing precipitation-top heights due to its insensitivity to smaller ice particles high in the atmosphere, and consequently the look-up table used for anvil rain is based on precipitation rates at the melting level.

The SLH dataset consists of a grid of 720x148 longitude-latitude elements corresponding to 0.5° x 0.5° spatial resolution and covers the region between 37°S to 37°N. The SLH dataset is not restricted to oceans like the TRAIN dataset is since the radar onboard TRMM is capable of measuring reflectivities over land. The variables included in the SLH files are latent heat convective conditional means ($Khour^{-1}$x100), latent heat deep-stratiform and shallow-stratiform conditional means ($Khour^{-1}$x100), convective pixel counts, deep-stratiform and shallow-stratiform pixel counts, and all pixel counts which includes clear pixels

(sum of latent heating in raining convective, raining stratiform, and non-raining pixels). The latent heat conditional means are in units of Khour^{-1}x100 so that the variables could be stored as integers. The latent heating conditional means contain 19 levels between the surface and 17 km.

The purpose of analyzing the SLH dataset was to compare the diurnal cycles of latent heating over land and oceans, and to compare the diurnal cycles of latent heating from the microwave imager and the precipitation radar over oceans for a consistency check. Before summing the SLH data, it was necessary to introduce time into the variables since a time variable was not included in this dataset. Time was incorporated into the SLH dataset by using the local times calculated from the UTC times within the TRAIN orbit files and matching those times onto the SLH grid (longitude grid in TRAIN and SLH datasets were defined differently). Once the local hour from the TRAIN dataset was identified and put into the SLH grid, it was necessary to interpolate the hours over land regions based on surrounding local hours for specific orbits over oceans since the available data from the TRAIN dataset did not include land data. For this interpolation, equation 2.1 was used to calculate a time fraction to add to or subtract from nearby ocean SLH time values in order to "fill in" the missing land values in between known ocean values. The division by 15° comes from the fact that 15° corresponds to 1 hour (360° divided by 24 hours in a day).

$$Time\ fraction = \frac{Longitude\ before\ a\ missing\ value - Longitude\ of\ a\ missing\ value}{15^{\circ}} \tag{2.1}$$

Once local time was assimilated into the SLH dataset, the data was ready to be summed into the 47-day periods. The summations were calculated by summing the product of the convective conditional mean and the convective pixel counts with the product of the stratiform conditional mean and the stratiform pixel counts. Once the summations from the SLH files were written to output files, the next step was to composite files from all years between 1998 and 2010 for each of the individual eight periods (refer back to Table 2.1), similar to what was done with the TRAIN files. Latent heating averages were calculated by dividing the sums of the convective and stratiform conditional latent heating means by the sum of the variable for all pixel counts. Total mean latent heating was calculated by adding together the convective and stratiform latent heating means.

2.6 Integrated Heating

For both the SLH and TRAIN datasets, a standard tropical atmosphere known as the McClatchey atmospheric profile was used to solve for the integrated total heating through the depth of the atmosphere. The McClatchey standard tropical atmosphere consists of heights from the surface to 100 km with corresponding pressures from 1013 millibars to .0003 millibars. The McClatchey profile was necessary to apply appropriate pressure-weighting to heating at each level. The McClatchey tropical atmospheric heights and pressures were used in accordance with the data in equation (2.2) to solve for integrated latent heating.

$$Q_{1,total} = \frac{\sum Q_{1,i} * \Delta p_i}{\sum \Delta p_i} \tag{2.2}$$

Where Δp is pressure differences for several layers of our tropical atmosphere and $Q_{1,i}$ is the latent heating values for the particular layers. The resulting integrated heating is consistent with the rain rates in millimeters per day via equation (2.3).

$$Rain\ rates = \frac{Integrated\ total\ latent\ heating * \Delta p * C_p * 0.0864 * 0.408}{86,400 * g} \tag{2.3}$$

where Δp is 93,410 $\mathrm{kgm^{-1}s^{-2}}$, C_p is 1,005 $\mathrm{Jkg^{-1}K^{-1}}$, and g is 9.8 $\mathrm{ms^{-2}}$. This equation was applied to the mean heating derived for all periods to test the validity of assuming a constant pressure profile for all profiles and the rain rates matched up very nicely with the estimated rain rates contained in the original TRAIN data files.

2.7 Fourier Analysis

Fourier Transform analysis was used in order to isolate the strength of the diurnal variations of latent heating in different regions and during different times of year. The data were decomposed into sums of sine curves and the amplitude and phase of the first and second harmonic were extracted as in the example shown in Figure 2.2. The fast Fourier transform (fft) function in MATLAB was used to solve for the amplitudes of the first harmonic, which represents the diurnal cycle. The second harmonic represents a semi-diurnal cycle, with two maxima and minima in a day (seen in Figure 2.3), and can be thought of as providing a rough check on the existence of non-diurnal oscillations in the dataset. The amplitudes of the different modes were found by using the absolute value (magnitude) function in MATLAB. After the diurnal amplitude of the data was computed, it was necessary to divide the amplitude by 12 since the output of the fft function in MATLAB by default is multiplied by a factor

of $\frac{L}{2}$ where L is the length of the vector used in the Fourier analysis (which in our case is 24 for all hours of the day). The appropriate phase was calculated by finding the phase that gave the minimum sum of the differences between the diurnal cycle of the data and the diurnal cycle of a particular sine wave for each hour of the day. This value was represented by the phase difference for all hours of the day and was computed by using equation (2.4) in order to solve for the best-fit phase of the data.

$$Phase\ difference = \sqrt{\sum diurnal_h - data_h} \tag{2.4}$$

Where $diurnal_h$ is a pre-defined sine curve with a phase between 1 and 24 and with the same diurnal amplitude that was calculated from the data.

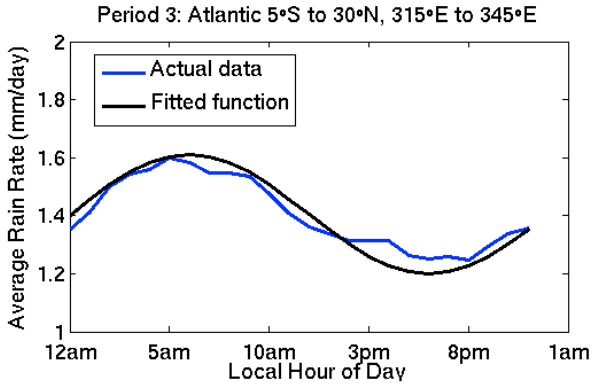

FIGURE 2.2: Example Fourier fit (black) to the average diurnal cycle of rain rates (blue) for a defined Atlantic Ocean boxed region in Period 3 (April 17th to June 2nd) between 1998 and 2010. Actual data is smoothed for comparison.

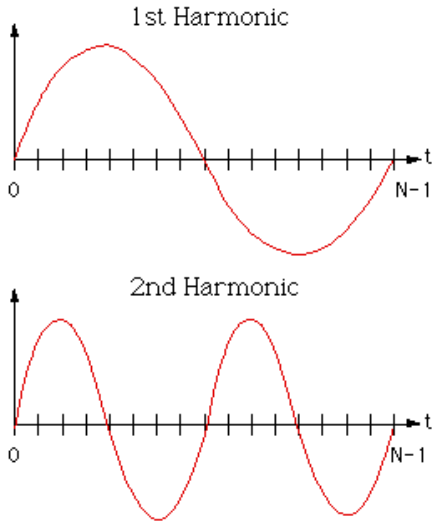

FIGURE 2.3: The first harmonic and the second harmonic of a Fourier series. Assuming a period of 24 hours, the first harmonic would represent a diurnal cycle with one maximum and one minimum in one day. The second harmonic would represent a semi-diurnal cycle with two maximums and two minimums in one day.

Once the appropriate phase was determined, the data could be labeled with the characteristic diurnal amplitudes and phases and then the diurnal variations could be compared between different regions and seasons. In summary, the fit of a sine function to the diurnal cycle of the averaged data gives the strength of the diurnal cycle through the amplitude and the local hour of maximum through the phase. The phases and amplitudes found in this research represent perfect sine curves, and so it is important to remember that the phases and amplitudes are only approximations for the real data. Another important point is that the amplitudes were calculated as percentages by dividing the amplitudes (in the same units as the variable of interest) by the average of the

variable of interest (e.g. latent heating) over the grid boxes and then multiplying by 100. Any amplitude percentages that were less than 2% of the maximum global value were masked – this removes regions with very small average rainfall amounts from the results since they can produce false indications of strong diurnal cycles.

Chapter 3

Global Distribution of Latent Heating

3.1 Spatial Characteristics

After organizing the TRAIN data into eight 47-day periods averaged between 1998 and 2010, it was possible to create a 13-year composite of average total rainfall in the tropical and subtropical oceans for each individual period. Surface rainfall is essentially the product of the integrated heating in an atmospheric column that is released into the atmosphere through condensation and the associated formation of rain drops. By viewing Figure 3.1, one can get a

sense for the spatial distribution of mean tropical rainfall and how that spatial distribution changes on average throughout the course of a year between different seasons. It is important to keep in mind that the tropics have much less seasonality than the higher latitudes due to small changes in solar heating throughout the annual cycle. Not surprisingly, the Inter-Tropical Convergence Zone (ITCZ) stands out in the tropics as the region with the heaviest rainfall relative to the rest of the subtropics and tropics all year-round. The ITCZ is an area of persistent uplift generated from the convergence of the easterly trade winds. This convergence zone migrates northward between January and September and drifts back equatorward between October and January. The latent heat that is released in the precipitation within this convergence zone is what essentially drives large-scale meridional overturning circulation. According to Figure 3.1, on average rain rates strengthen to as high as 15 millimeters per day in the eastern Pacific as the ITCZ travels northward and weaken as the ITCZ travels southward. The South-Pacific Convergence Zone (SPCZ) is another region of extensive heavy rainfall that is located northeast of Australia in December and January and shrinks in size and intensity substantially between March and November. Other features seen in Figure 3.1 include a secondary ITCZ that develops off of the west coast of South America in the Southern Hemisphere in March and April. This secondary ITCZ is supported by studies such as Masunaga et al (2011) where they discovered a seasonal double ITCZ that appeared

in austral fall (Masunaga and L'Ecuyer, 2011). There is also an increase in precipitation in the summer monsoon season in Southeast Asia during the Northern Hemisphere (NH) summer months. According to the TMI, there is very little rainfall on average off of the west coasts of continents during all times of year. These "ocean desert" regions will often be masked due to low overall rain rates in the results that follow.

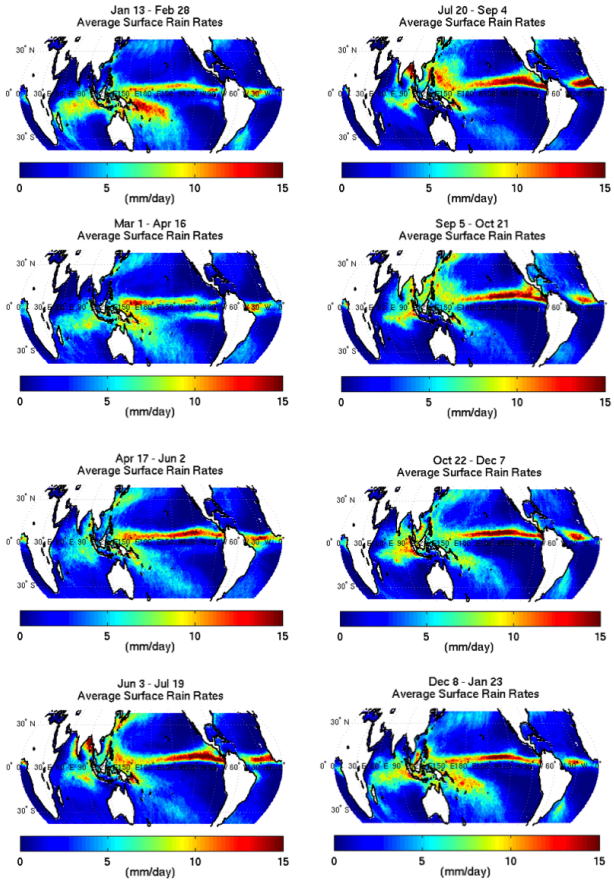

FIGURE 3.1: 13-year composite of average total rainfall over oceans in TRMM coverage region between 38°S and 38°N for eight pre-defined 47-day periods between 1998 and 2010. Rainfall estimates originate from a dataset that was generated from the TRAIN algorithm. Units are in millimeters per day.

3.2 Vertical Structures

The two major atmospheric circulations that shape the climate in the tropics and subtropics are the Walker Circulation and the Hadley Circulation. The Hadley Circulation consists of rising motion near the equator and sinking motion near 30° latitude. This large-scale meridional circulation transports tropical heat and moisture vertically into the atmosphere and poleward towards higher latitudes. Latent heat release is a necessary source of energy for sufficient atmospheric instability to support convection. The boundaries of TRMM conveniently cover the complete Hadley Circulation, and so it is possible to use the two datasets in this study to examine the vertical latent heating profiles that are associated with the rainfall within this large-scale meridional circulation. Figure 3.2 displays the average vertical profiles of total latent heating associated with the Hadley Cell and the seasonal evolution over the eight periods averaged between 1998 and 2010 from both the TRAIN and SLH algorithms. Based on the cross-sections, there is an apparent deep layer of total heating between 1 km and 10 km concentrated close to the equator in the TRAIN heating profiles. The heating layer is not as deep in the SLH heating profiles, which show maximum heating between 5 km and 10 km. Differences in the location of the maximum average total latent heating between Period 1 and Period 5 in both algorithms illustrate the seasonal migration of the ITCZ northward in July and

August and southward in January and February. The level of maximum heating is not easily discernible in the TRAIN profiles in December, January and February, but is clearly at an altitude of about 7 km during all other times of year. Finally, the SPCZ and the secondary ITCZ appear in the vertical cross-section in Periods 8, 1, and 2 located around 5°S-10°S, but do not appear in all other periods.

Recall that total latent heating is the combination of stratiform and convective latent heating. Latent heating profiles in convective regions look very different from the heating profiles in stratiform regions. For example, (Grecu et al., 2009) stated that convective latent heating profiles "exhibit positive maximum in lower-to-mid troposphere because of condensation-deposition of water vapor in moist updrafts." Stratiform latent heating profiles, on the other hand, have "positive maximum in the upper troposphere and negative minimum due to evaporation of precipitation in the lower troposphere" (Grecu et al., 2009). The cooling beneath the melting layer in stratiform heating profiles is mainly caused by evaporation, but may also be caused by melting within a kilometer below the 0°C level (Tao et al., 1993).

Figure 3.3 shows the convective component of the total latent heating associated with the Hadley Circulation. Based on this figure, it appears that the TRAIN convective heating is deeper and stronger than the SLH convective heating, similar to what was seen in the total latent heating. The height of maximum

convective latent heating is higher in the TRAIN vertical profiles than it is in the SLH vertical profiles. The stratiform component of the total latent heating associated with the Hadley Circulation is presented in Figure 3.4. In this case, the stratiform component looks larger in magnitude in SLH than in TRAIN. Nevertheless, the general spatial distribution of the stratiform heating and the height of maximum stratiform heating look similar between both algorithms.

The Walker Circulation is the other large-scale circulation that influences zonal variability in the tropics, most notably across the equatorial Pacific Ocean. (Hartmann et al., 1984) showed that this mean zonal tropical circulation "is sensitive to the assumed vertical distribution of latent heating by equatorial cloud systems" (Simpson et al., 1988). Normal conditions in the Pacific Ocean comprise of easterly trade winds that transport solar-heated surface waters from the east Pacific to the west Pacific that then pile up against the Indonesian landmass. Strong eastward energy transport by the Walker Circulation results from the rising motion (warmer waters and lower pressure) in the west Pacific and the sinking motion (cooler waters and higher pressure) in the east Pacific (L'Ecuyer et al., 2006).

Figure 3.5 illustrates the typical seasonal variations of the zonal distribution of average total latent heating averaged over all TRMM latitudes and over all hours of the day for the eight periods based on the 13 years analyzed. According to both algorithms, larger amounts of latent heating are concentrated

over the warm pool region in the west Pacific where rainfall and convection are prevalent. There is also virtually no latent heating in the east Pacific where there tends to be little rainfall consistent with cooler waters and sinking atmospheric motion. The vertical extent of latent heating from the TRAIN algorithm is between 4 km and 7 km, and there are greater amounts of atmospheric heating in the equatorial-central Pacific in January and February than in July, August, and September. There is, however, a persistent layer of larger latent heating values in the TRAIN heating profiles centered between 3 km and 4 km and present over the entire longitudinal-range of the Pacific Ocean during all times of year. The level of maximum heating is situated at approximately 7 km during most times of year, with the strongest maximum latent heating occurring in October to April (Periods 7, 8, 1, and 2). The heating structures derived from the SLH algorithm show similar levels of maximum latent heating and also similar patterns of annual strengthening and weakening of latent heating.

One difference between the TRAIN and SLH vertical cross-sections is that there is weaker lower-level total latent heating in the SLH algorithm than in the TRAIN algorithm; that is, there is no persistent horizontal layer of larger latent heating values throughout the annual cycle in the SLH heating structures that was present in the TRAIN heating structures. According to a previous study on the difference between TMI and PR measurements over the East China Sea, the TMI detects light rainfall that the PR does not, and the authors concluded

that this may be due to high sulfate aerosol-optical depths which increases the liquid water content in the atmosphere. They explain further that the PR is "insensitive to clouds and light drizzle", and this might explain why the PR misses precipitation in the west Pacific (Berg et al., 2006). An additional conclusion of this study was that the main difference between the TMI and PR rainfall estimates likely resulted from differences in estimated rainfall intensity. They addressed this issue by using total column water vapor as a proxy variable for TMI and PR differences (Berg et al., 2006).

Figure 3.6 displays the convective component of the latent heating associated with the Walker Circulation. Similar to what was observed in the Hadley Cell convective latent heating profiles, the convective heating is stronger in the TRAIN vertical structures than in SLH. Again, there is stronger convective heating closer to the surface in SLH than in TRAIN around 2-3 km. In general, the TRAIN profiles have stronger convective heating across all longitudes of the Pacific. The stratiform component of latent heating associated with the Walker Circulation is illustrated in Figure 3.7, and there appears to be much stronger stratiform latent heating in the SLH profiles than in the TRAIN profiles. The layer of higher stratiform latent heating values is also vertically thicker in SLH than it is in TRAIN. The deeper layer of total latent heating in TRAIN can therefore be explained by the convective portion of the latent heating.

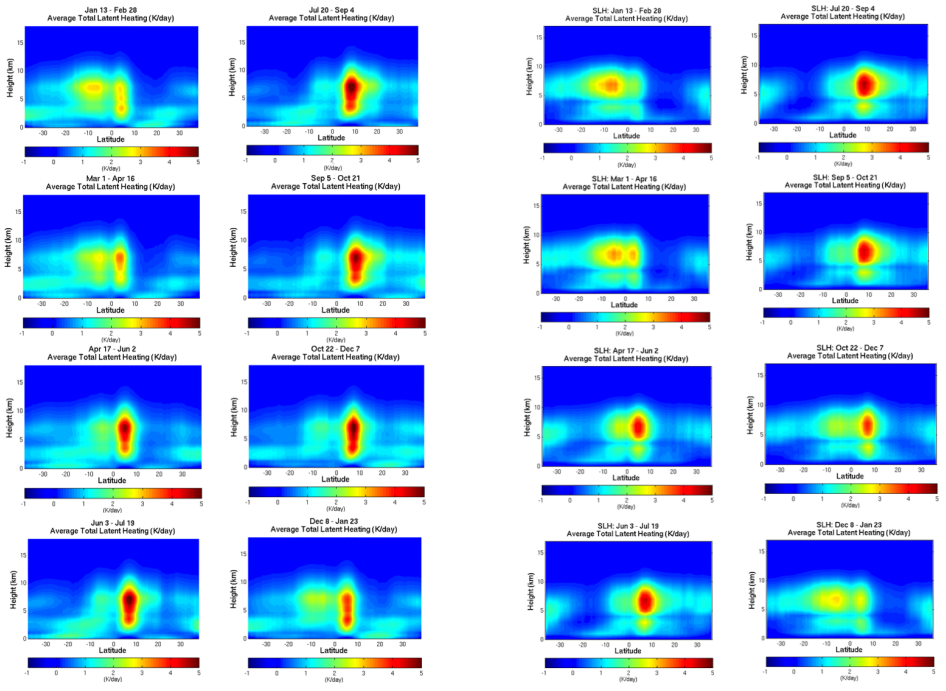

FIGURE 3.2: 13-year composite of average vertical structure of total (stratiform + convective) latent heating associated with the mean meridional circulation in the tropics for all hours of the day for all eight pre-defined periods between 1998 and 2010 from TRAIN algorithm *(left)* and SLH algorithm *(right)*. Units are in Kelvin per day.

3.3 Integrated Heating

Keeping in mind that integrated heating is directly related to accumulated surface rainfall on long timescales, Figure 3.8 depicts the computed global integrated total heating for all eight periods and from both TRAIN and SLH. The integrated latent heating was calculated by pressure-weighting and summing the latent heating profiles as discussed in Section 2.6. The spatial distribution of global integrated heating matches quite well between both algorithms and correlates nicely with the surface rain rates in Figure 3.1. However, there are

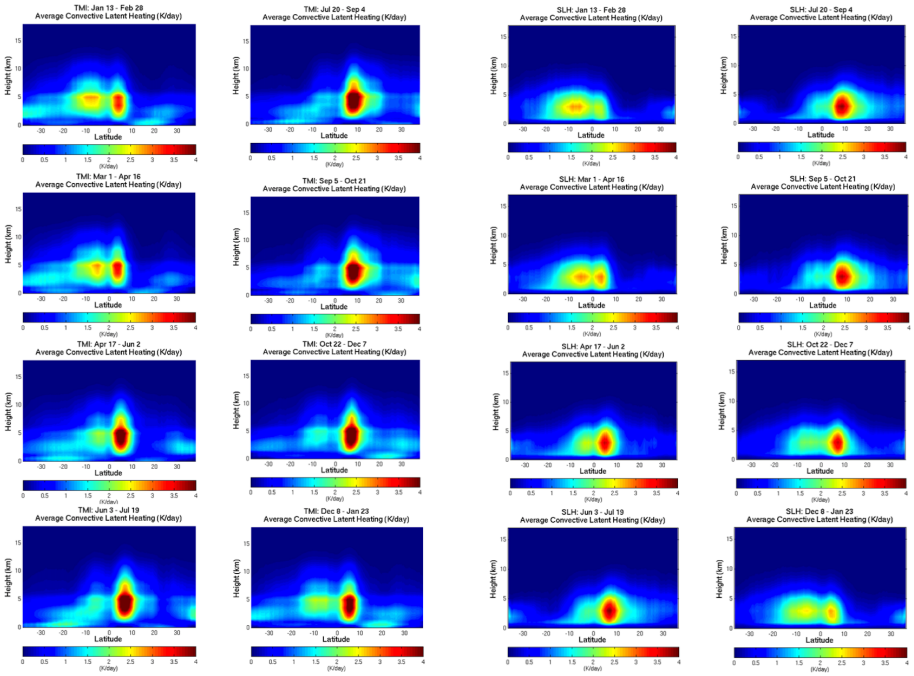

FIGURE 3.3: 13-year composite of average vertical structure of convective latent heating associated with the mean meridional circulation in the tropics for all hours of the day for all eight pre-defined periods between 1998 and 2010 from TRAIN algorithm *(left)* and SLH algorithm *(right)*. Units are in Kelvin per day.

differences between the two algorithms in the magnitudes of the latent heating. For example, the spatial area of larger values of integrated heating is more extensive in the ITCZ region and in the Maritime Continent region in the TRAIN algorithm than it is in the SLH algorithm. There also appears to be stronger integrated heating in the east Pacific in TRAIN compared to SLH. This finding agrees with the past study that was mentioned in the previous section in which they found that TMI estimates showed the largest bias relative to the PR over the central and eastern Pacific Ocean ITCZ (Berg et al., 2006). In general,

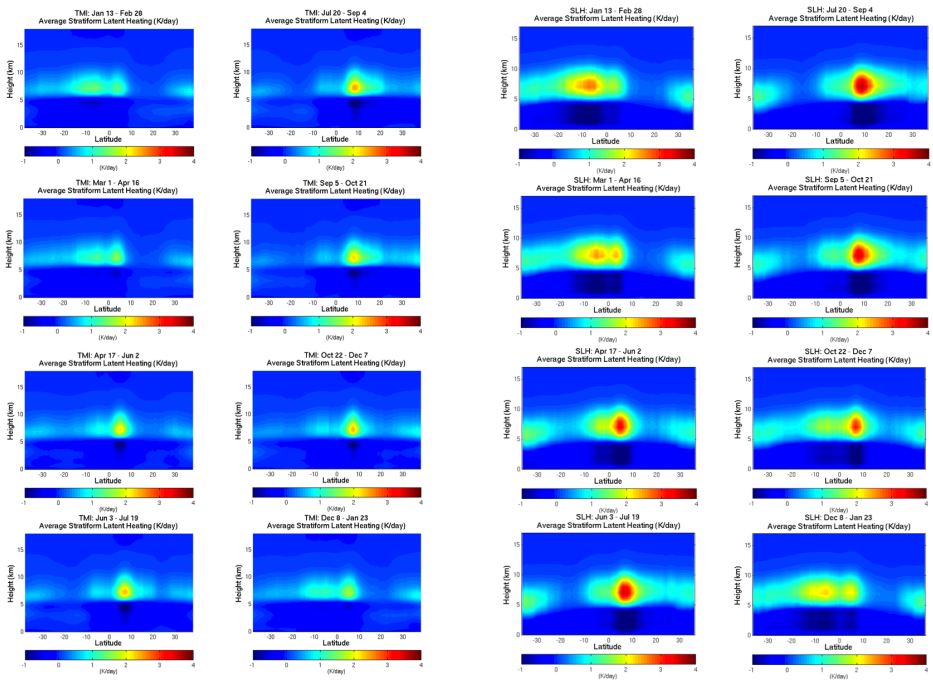

FIGURE 3.4: 13-year composite of average vertical structure of stratiform latent heating associated with the mean meridional circulation in the tropics for all hours of the day for all eight pre-defined periods between 1998 and 2010 from TRAIN algorithm *(left)* and SLH algorithm *(right)*. Units are in Kelvin per day.

the SLH integrated heating looks more noisy and sporadic than the TRAIN integrated heating – this is a clear indication of the improved sampling of the TMI instrument over the PR instrument. Higher latent heating values are more likely to influence the PR averages but tend to be averaged out by surrounding lower values in the TRAIN heating profiles.

The SLH global plots provide integrated heating over land that is not available from TRAIN. The greatest integrated heating values over land tend to be found over north-central South America and move meridionally with the ITCZ. There are also noticeably larger integrated heating values over the southern half

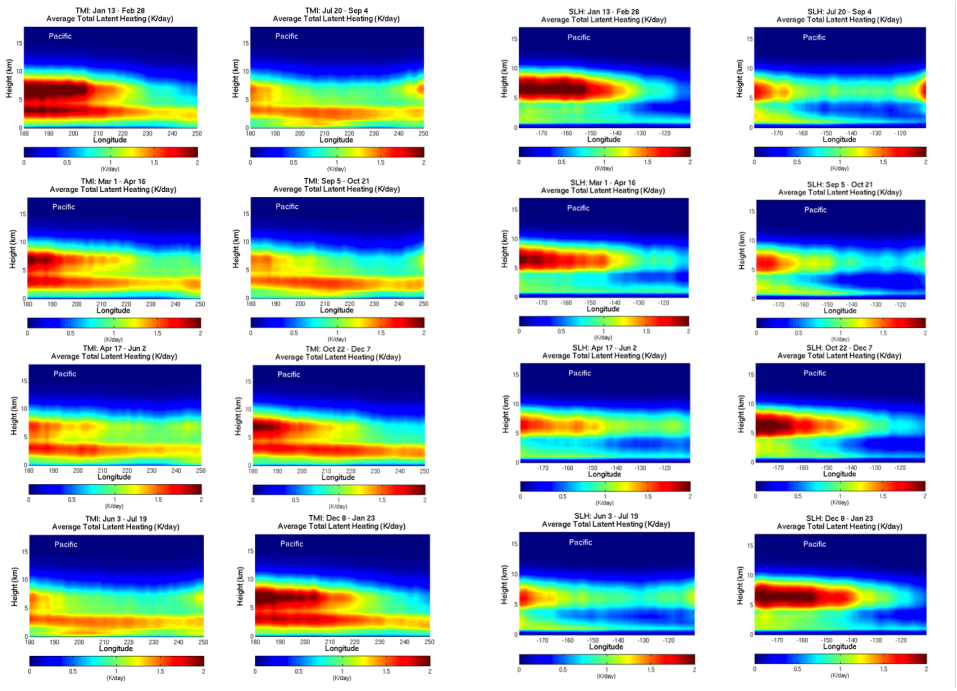

FIGURE 3.5: 13-year composite of average vertical structure of total (stratiform + convective) latent heating in the Pacific Ocean associated with the mean zonal circulation in the tropics for all hours of the day for all eight pre-defined periods between 1998 and 2010 from TRAIN algorithm *(left)* and SLH algorithm *(right)*. Units are in Kelvin per day.

of Africa. Knowledge of major geographical features over land regions that are analyzed in this study may be beneficial for understanding heating distributions over land. Northern Africa includes the Sahara Desert, and the southern tip of Africa includes the Kalahari Desert. The western half of Australia features dry and arid conditions across multiple deserts. Northern South America consists of rainforests as part of the Amazon Rainforest. Higher elevations are found in the southern half of Africa, and the Andes Mountains are located along the west coast of South America. South-central Asia has much higher elevations as a part of the Himalayas, with some drier regions to the west and

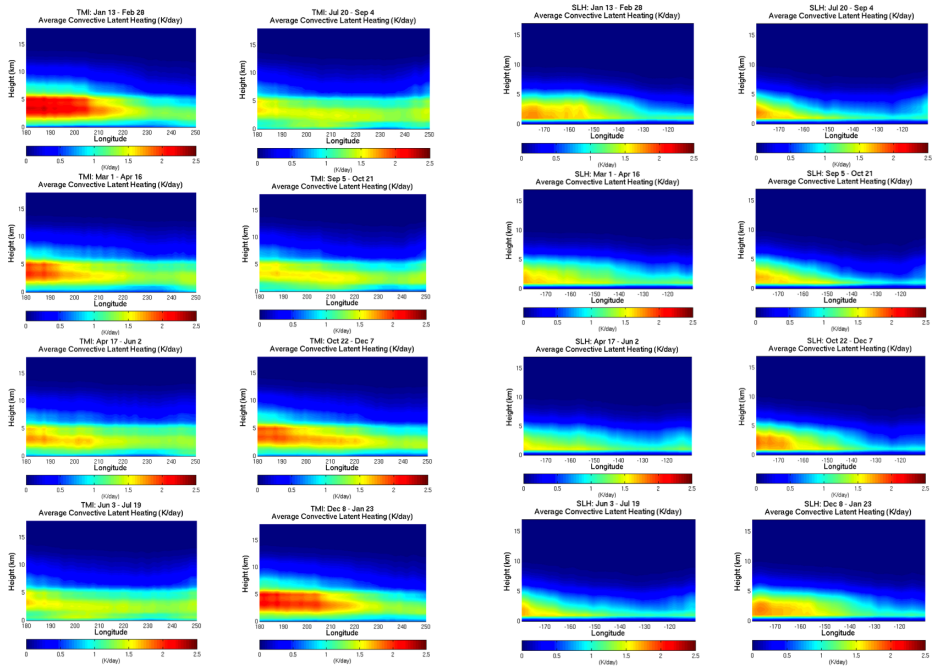

FIGURE 3.6: 13-year composite of average vertical structure of convective latent heating in the Pacific Ocean associated with the mean zonal circulation in the tropics for all hours of the day for all eight pre-defined periods between 1998 and 2010 from TRAIN algorithm *(left)* and SLH algorithm *(right)*. Units are in Kelvin per day.

northwest of the Himalayas. Finally, the North American West Coast contains higher elevations and dry, desert regions.

3.4 Diurnal Cycles

Diurnal amplitudes over land and oceans were calculated on a lower spatial-resolution grid of 5° x 5° grid boxes for each of the eight periods in order to provide sufficient sampling when the dataset is further divided according to the

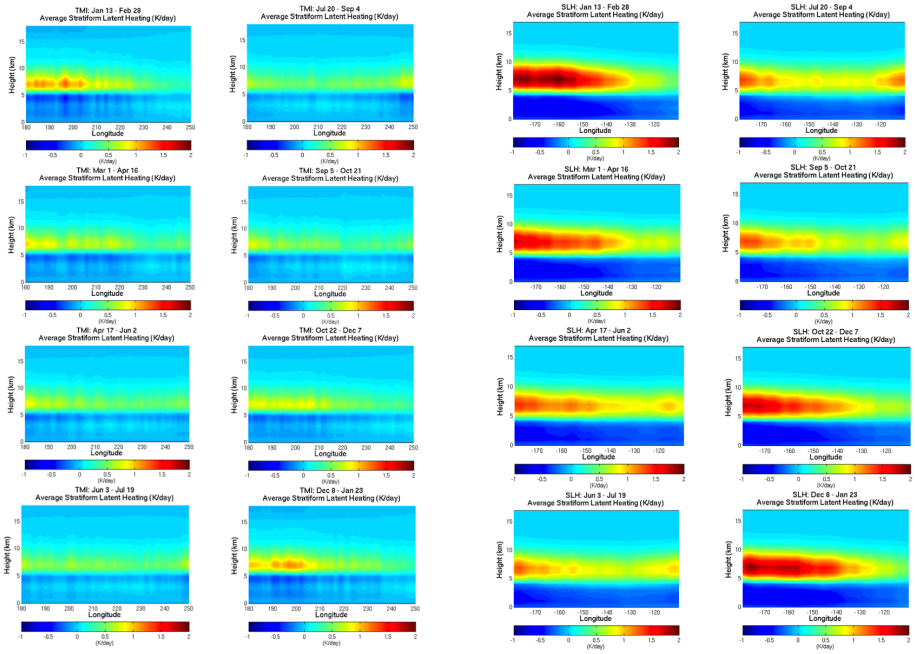

FIGURE 3.7: 13-year composite of average vertical structure of stratiform latent heating in the Pacific Ocean associated with the mean zonal circulation in the tropics for all hours of the day for all eight pre-defined periods between 1998 and 2010 from TRAIN algorithm *(left)* and SLH algorithm *(right)*. Units are in Kelvin per day.

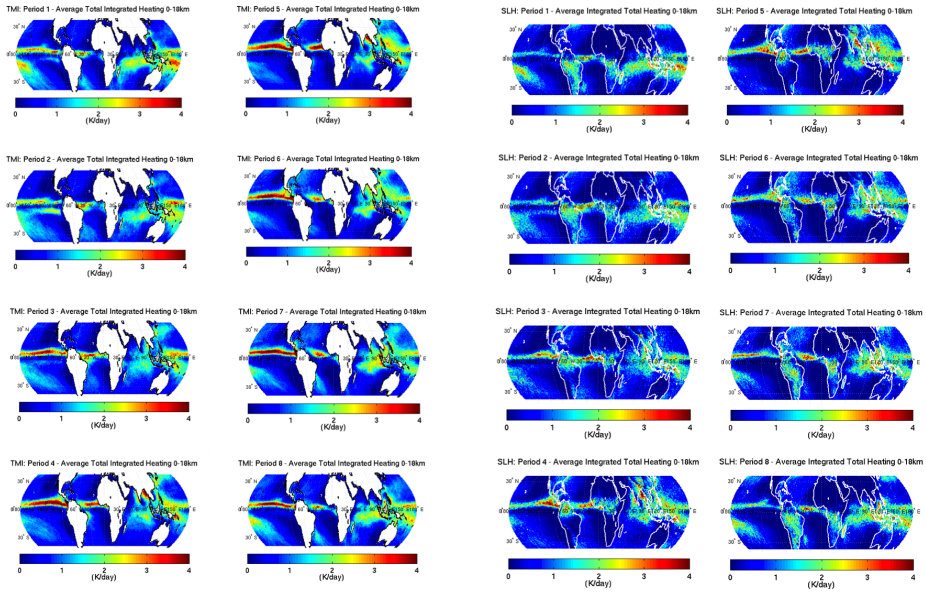

FIGURE 3.8: 13-year composite of average integrated total heating for all hours of the day and for all eight pre-defined periods between 1998 and 2010 from TRAIN algorithm *(left)* and SLH algorithm *(right)*. Units are in Kelvin per day.

time of day. Figure 3.9 shows the global distribution of the diurnal cycle amplitudes for NH winter (Period 1) and for NH summer (Period 5), from both the TRAIN and SLH algorithms. The diurnal amplitudes represent the strength of the diurnal cycle and were calculated based on the method that was described in Section 2.7 where a best-fit sine curve is applied to the time-evolution of the average integrated total latent heating in each 5° x 5° grid box. The amplitudes are presented as percentages to facilitate comparison of regions with different total rainfall accumulations. Grid boxes are masked out in white when the average integrated total latent heating within that box is less than 2% of the maximum global integrated total latent heating value for each particular period. The removes spuriously large diurnal amplitude fractions (i.e. noise) that do not necessarily truly indicate a strong diurnal cycle within that box.

Based on Figure 3.9, there are largely uniform diurnal amplitudes over open ocean areas ranging between 0% and 20% in the TRAIN algorithm and between 10% and 50% in the SLH algorithm. In the TRAIN dataset, there are larger diurnal amplitudes over ocean areas near the Maritime Continent region in Periods 1 and 5 and near Central America in Period 5. The Maritime Continent region contains both land and ocean and "represents a unique geographic region that contains large islands, narrow peninsulas, and complex terrain surrounded by large oceanic and continental areas" (Nesbitt and Zipser, 2003). The

higher amplitudes in the Maritime Continent region occur during all eight periods and therefore during all times of year. In the TRAIN global plots, the larger diurnal amplitude fractions in July, August, and September in the Central America ocean region almost completely vanish in January and February. The stronger diurnal cycles are likely related to the development of summertime convection over landmasses within and nearby to these regions, particularly during summer months when insolation is strong. Over land, maximum rainfall typically occurs in the afternoon and evening due to instability caused by daytime solar heating. This is exactly what is seen in the SLH amplitudes over land – higher amplitudes representing stronger diurnal cycles. A few areas over land actually have diurnal amplitude percentages that approach 100% in the SLH plots.

The global phases for NH summer and winter based on the best fits to the average integrated total latent heating in the 5° x 5° grid boxes are illustrated in Figure 3.10, again for both the TRAIN and SLH algorithms. The phase represents the local hour of maximum daily integrated total latent heating in each grid box. It is apparent that in both winter and summer, the majority of the oceans have phases in the early morning hours between about 4am and 7am based on the TRAIN algorithm. It is worth noting that some ocean regions in the TRAIN phase plots have times of local maximum heating in the afternoon and evening based on the fits. For example, there is a local time of

maximum integrated latent heating around noon off of the east coast of Australia in the southeastern Pacific in both Periods 1 and 5. There is also a peak of heating around 7pm off the southeastern coast of Asia and for the Central American region in the summer. Overall, it seems that the ocean regions from the TRAIN dataset that do have afternoon and evening maxima tend to be in the mid-latitudes. These later peaks may be related to a "secondary peak" of rainfall and latent heating over oceans that has been discussed in some studies. In one study, for instance, a second peak was found to be "especially prominent in the central Pacific and SPCZ" regions. In the same study, they state that the "secondary peak in rainfall from features with ice scattering in the afternoon also corresponds to a peak in the number of features in the early afternoon" (Nesbitt and Zipser, 2003). The later hours of maximum heating may be related to the greater seasonality in the higher latitudes due to larger differences in solar heating between seasons, or perhaps due to the greater land area in the mid-latitudes in both hemispheres (especially in the Northern Hemisphere) as compared to the equatorial region.

In the SLH algorithm, there is a striking difference in the phases between land and ocean. In fact, the land masses unmistakably stand out in the global plots with afternoon and evening peaks of heating. There are fewer ocean regions that have afternoon and evening maxima in the SLH algorithm than in the TRAIN algorithm. Having both morning and afternoon maxima in any given

region violates the assumption that the first harmonic represents the evolution of precipitation in that region. Figure 3.11 shows global maps of the ratio of the semi-diurnal amplitude to the diurnal amplitudes in both SLH and TRAIN, with larger ratios representing larger deviations from the first harmonic. Over some ocean regions where there are afternoon and evening peaks, the amplitude ratios for those regions are also very large, confirming that the first harmonic does not always accurately represent the diurnal cycles of precipitation in certain regions.

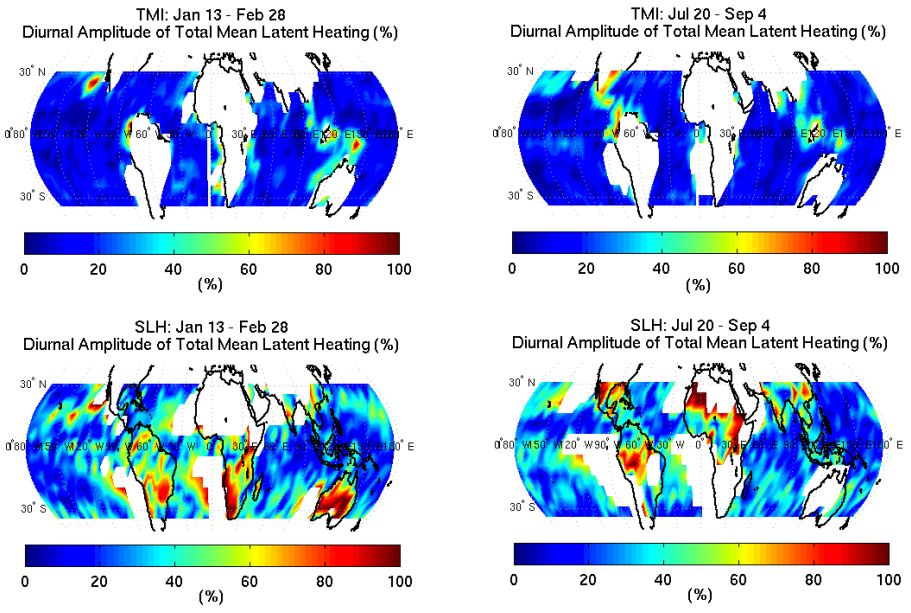

FIGURE 3.9: Global map of characteristic diurnal amplitude fractions for integrated total latent heating over 5° x 5° grid boxes for Period 1 *(left)* and Period 5 *(right)* from the TRAIN algorithm *(top)* and the SLH algorithm *(bottom)*. Masking is included wherever rain rates over 5° x 5° grid boxes were less than 2% of the global maximum value.

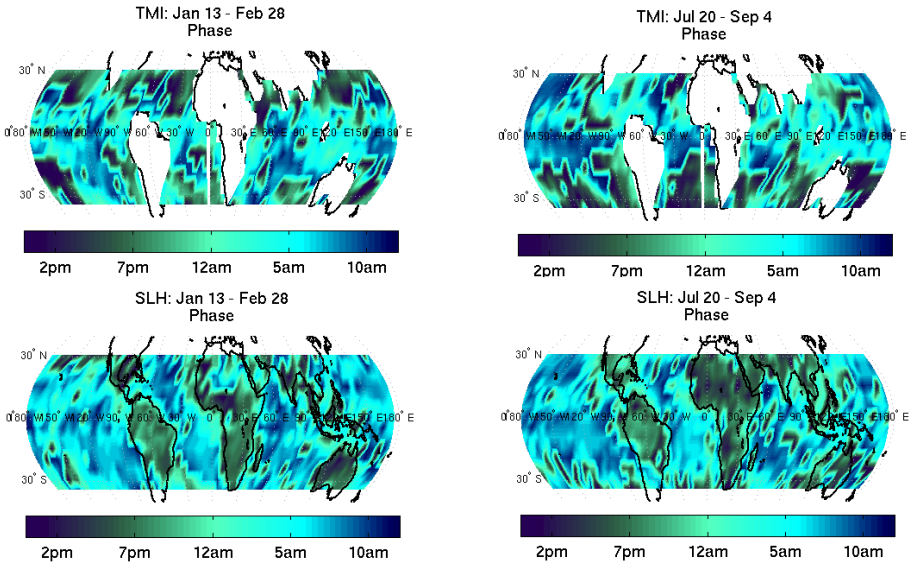

FIGURE 3.10: Global map of characteristic phases for integrated total latent heating over 5° x 5° grid boxes for Period 1 *(left)* and Period 5 *(right)* from the TRAIN algorithm *(top)* and the SLH algorithm *(bottom)*.

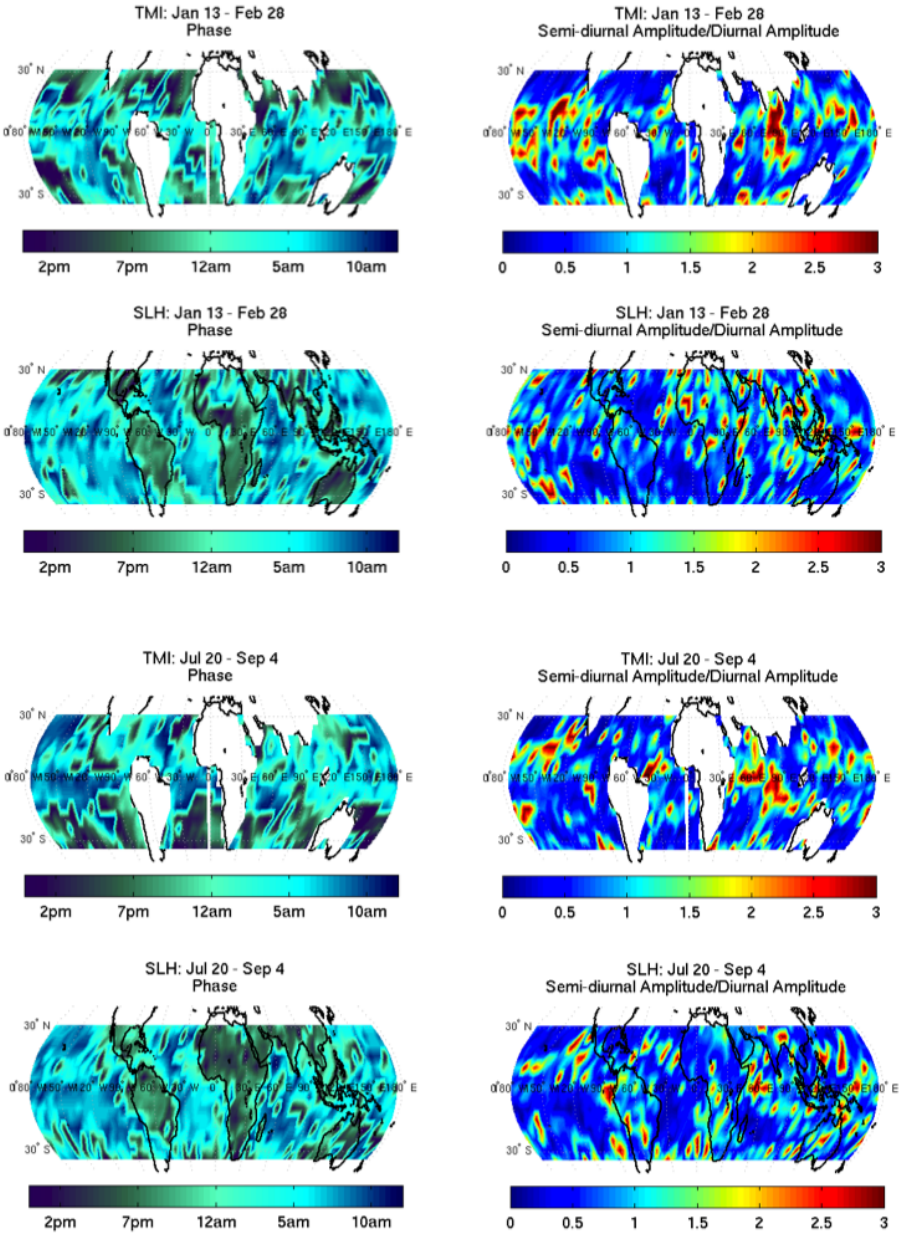

FIGURE 3.11: Global map of characteristic phases *(left)* for integrated total latent heating over 5° x 5° grid boxes and the amplitude ratios (semi-diurnal/diurnal) *(right)* for Period 1 *(top half)* and Period 5 *(bottom half)* from the TRAIN algorithm *(top)* and the SLH algorithm *(bottom)*.

Chapter 4

Regional Latent Heating Characteristics

4.1 Latent Heating Over Ocean

The temporal variation of integrated heating is examined in greater depth for seven ocean regions to get an idea of how latent heating varies in time both seasonally and diurnally in different locations. Stratiform, convective, and total latent heating profiles are all analyzed, but the primary focus is on the integrated total latent heating. Stratiform and convective latent heating are important to study separately because it is recognized that the cloud processes and

vertical structures of stratiform and convective latent heating are characteristically different (Grecu et al., 2009). Furthermore, it is well-known that systems with mostly stratiform latent heating interact differently with the tropical circulation than purely convective systems do (Jakob and Schumacher, 2008). The ocean regions are illustrated in Figure 4.1 and are defined as follows from left to right: Indian, Maritime Continent, Northwest Pacific *(top)*, Tropical West Pacific *(bottom)*, East Pacific, Central America, and Atlantic. The latitude and longitude boundaries of all of the boxed ocean regions are defined in Table 4.1. These seven regions were specifically chosen in order to sample each ocean in the tropics and to highlight a cross-section of distinct large-scale regimes. Some of the regions chosen are partially covered by land, but only the oceanic portion of these boxes are included in the analysis since the TRAIN dataset does not provide estimates over land. In this paper, six of the seven regions are discussed. All figures relevant to each of the seven ocean regions are included in Appendices A-G located at the end of this paper.

The total number of observations from the microwave imager and precipitation radar for the ocean regions will differ slightly since the boxes are not all the same size. Table 4.2 shows that the sampling from the TRAIN algorithm over all ocean regions for any given period are very large, over 2 million for all ocean regions, and therefore considered sufficient for statistically-significant climatological averages. A similar assessment of the number of observations from

the SLH dataset over the same ocean regions reveal a smaller number of observations than what is seen in the TRAIN dataset, but still greater than 600,000 for all regions and for all times of the year. It was necessary to mask out the land values over the ocean regions chosen in the SLH algorithm in order to compare the ocean regions between TRAIN and SLH.

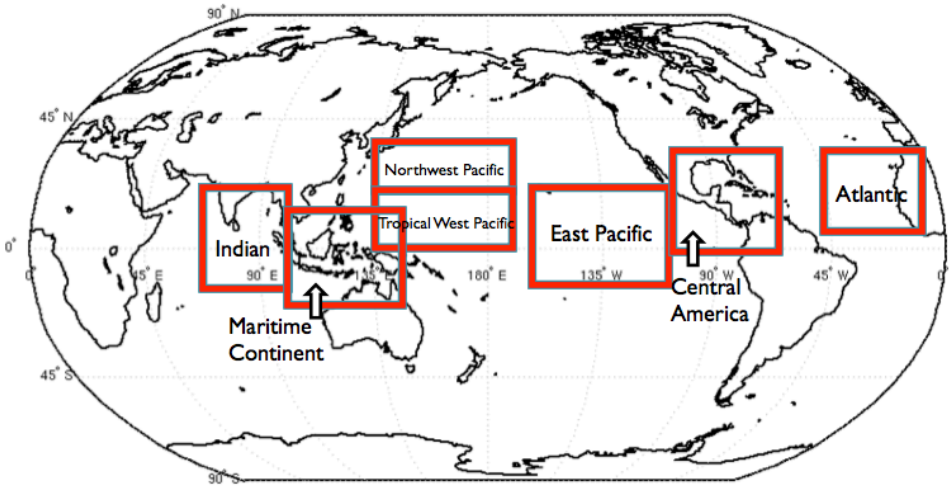

FIGURE 4.1: Seven ocean regions studied: Northwest Pacific, Tropical West Pacific, East Pacific, Atlantic, Indian, Maritime Continent, and Central America.

TABLE 4.1: User-defined latitude and longitude limits for the seven ocean regions. *Note: Northwest Pacific and Tropical West Pacific were defined from 135°E-180°E for SLH algorithm.

Ocean Region	**Latitudes**	**Longitudes**
Northwest Pacific	20°N-35°N	135°E-185°E
Tropical West Pacific	0°-20°N	135°E-185°E
East Pacific	10°S-20°N	200°E-250°E
Atlantic	5°N-30°N	315°E-345°E
Indian	10°S-20°N	70°E-100°E
Maritime	15°S-10°N	100°E-150°E
Central America	0°-30°N	250°E-300°E

TABLE 4.2: Total number of observations in units of millions for the seven ocean regions for the TRAIN algorithm and the seven ocean regions for the SLH algorithm for each of the 8 periods. *Note: The longitude range was to 185°E in the TRAIN algorithm, but was to 180°E in the SLH algorithm for the Northwest Pacific and Tropical West Pacific. Also number of observations within a box will depend on the size of the box, which differs between different regions. Land regions chosen were smaller than all ocean regions.

TRAIN: (x10^6)	Period 1	Period 2	Period 3	Period 4	Period 5	Period 6	Period 7	Period 8
Northwest Pacific	3.9	3.9	3.9	4.0	3.9	3.6	3.9	3.9
Tropical Pacific	3.0	3.0	3.0	3.0	2.9	2.7	2.9	2.9
East Pacific	4.4	4.4	4.4	4.4	4.3	4.0	4.3	4.3
Atlantic	2.5	2.5	2.5	2.5	2.5	2.3	2.5	2.5
Indian	2.2	2.2	2.2	2.2	2.1	2.0	2.1	2.1
Maritime	2.5	2.5	2.5	2.5	2.4	2.3	2.4	2.4
Central America	3.3	3.3	3.3	3.3	3.3	3.1	3.3	3.3
SLH: (x10^6)	**Period 1**	**Period 2**	**Period 3**	**Period 4**	**Period 5**	**Period 6**	**Period 7**	**Period 8**
Northwest Pacific	1.4	1.4	1.4	1.4	1.3	1.2	1.4	1.4
Tropical Pacific	0.95	0.96	0.95	0.93	0.92	0.84	0.95	0.95
East Pacific	1.5	1.5	1.5	1.5	1.5	1.4	1.5	1.5
Atlantic	0.90	0.90	0.90	0.88	0.88	0.79	0.90	0.90
Indian	0.75	0.75	0.75	0.73	0.72	0.66	0.75	0.75
Maritime	0.91	0.91	0.90	0.89	0.88	0.80	0.90	0.90
Central America	1.3	1.3	1.3	1.2	1.2	1.1	1.3	1.3

The seven boxed ocean regions are superimposed with the global average rain rates for January-February (Period 1) and July-September (Period 5) in Figure 4.2. These plots depict how rainfall intensity varies between two seasons by location. The Tropical West Pacific has a noticeable increase in mean rainfall from winter to summer due to the northward migration of the ITCZ. The East Pacific contains the ITCZ throughout all eight periods, but both the areal extent and intensity of rainfall increase in the summer in Period 5. In the Atlantic, there is more rainfall in the box in the summertime since the northern edge of the ITCZ enters the box during that time of year. For the Northwest Pacific region, which is the farthest north of all seven regions, there are no signs of the ITCZ in Northern Hemisphere winter nor summer, but a slight increase

in rainfall is evident due to the monsoonal rains in Southeast Asia in Northern Hemisphere summertime.

The Indian region experiences rainfall during both Periods 1 and 5, but the average rainfall amount within the box increases in the summertime due to the Indian monsoon season, which generally occurs between June and October. The Maritime Continent region appears to have higher average rain rates in the wintertime, likely because the ITCZ moves northward and nearly out of the boxed region in the summertime. Finally, the Central American region seems to have more rainfall in the summer due to a more intense ITCZ. Therefore, every region exhibits changes in rainfall due to either the seasonal migration of the ITCZ or the Indian monsoon season. The structure and variation of latent heating in each of these regions will be considered in detail in this chapter.

Average rain rates within all seven regions averaged over all hours of the day and for each individual 47-day period are shown in Figure 4.3. The ocean regions with the highest amounts of average rainfall throughout the annual cycle include the Indian, Maritime, and Tropical West Pacific regions. The lightest average rainfall is found in the Atlantic, especially between January and June during a period of subsidence. The East Pacific and the Northwest Pacific look very similar to each other in their average rainfall rates, and both have near-constant average rainfall throughout their annual cycles. The mean rain rates in the Central America, Atlantic, and Indian regions behave similarly with a

gradual increase in the summertime months. The cause for the gradual increase in rain in the summer for the three regions likely differs. For example, in the Atlantic and Central American regions, the increase in rainfall in June, July, and August appears to be due to the movement of the ITCZ into those regions. On the other hand, the increase in rainfall in the Indian region is likely related to the stages of the Indian monsoon, which relate to differences in land and ocean temperatures. A recent study by (Clayson and Bogdanoff, 2013) supports these conclusions by stating that in the Indian Ocean, seasonal shifting of the Sun was the second most dominant mode of variability, with the first being related to the monsoonal cycle. For the Pacific and Atlantic basins, Clayson and Weitlich (2007) found based on an analysis of tropical diurnal sea-surface temperature (SST) warming that the most dominant mode of variability was the seasonal shifting of the Sun (Clayson and Bogdanoff, 2013).

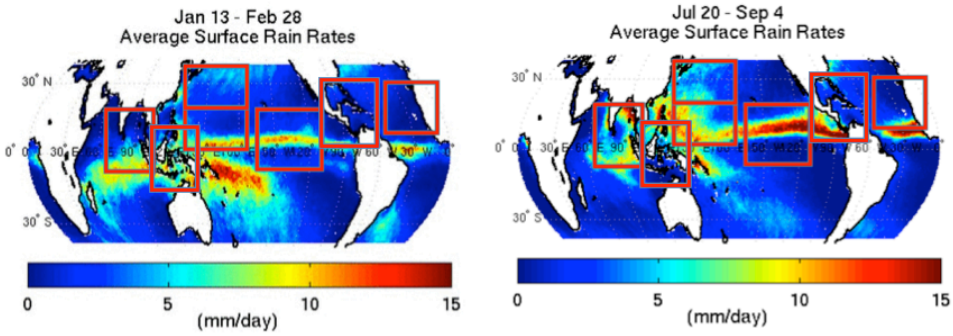

FIGURE 4.2: 13-year composite of the average total rain rates in Period 1 and Period 5 for the seven ocean regions.

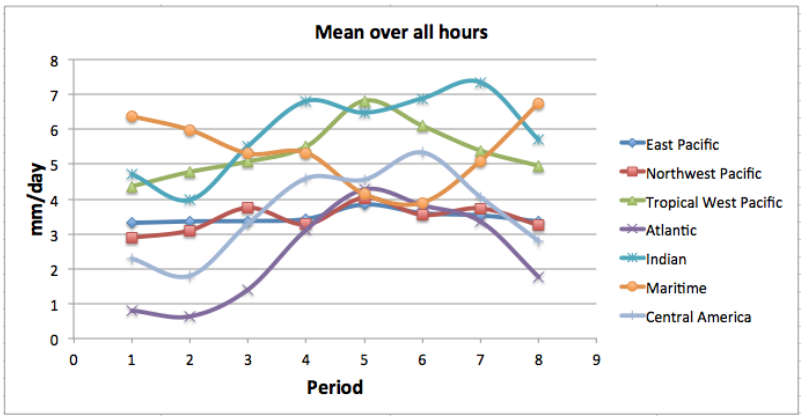

FIGURE 4.3: The annual cycle of average rain rates from TRAIN algorithm in units of millimeters per day averaged over each ocean-boxed region and over all hours of day for each of the eight 47-day periods for 1998-2010.

4.1.1 West Pacific

4.1.1.1 Tropical West Pacific

The Tropical West Pacific latent heating profiles in Figure 4.4 show weaker heating in the Northern Hemisphere winter months. The total heating in January-February is only about 2 Kday^{-1} in both the TRAIN and SLH algorithms. There are differences in the latent heating profiles between the datasets, especially in Period 1. For example, there is a much deeper layer of heating in January and February in the TRAIN algorithm. Additionally, the stratiform latent heating is stronger in Period 1 in the TRAIN algorithm, and the convective latent heating maxima is located higher in the atmosphere in the TRAIN algorithm at around 5 km. The convective latent heating maxima occurs closer to the surface in the SLH algorithm in both Period 1 and 5. The vertical structures of the latent heating and the diurnal evolution of the latent heating agree pretty well between

both algorithms in July-September (Period 5), when the heating is stronger in the Tropical West Pacific box. The only difference between both algorithms in the latent heating profiles in Period 5 is that the SLH convective latent heating is closer to the surface. Nevertheless, it is clear from both algorithms that the Tropical West Pacific tends to have an early morning maximum in total latent heating in July-September. The timing of maximum heating is somewhat less obvious in January-February, but there is a hint of larger values of heating in the early hours of the day in both algorithms.

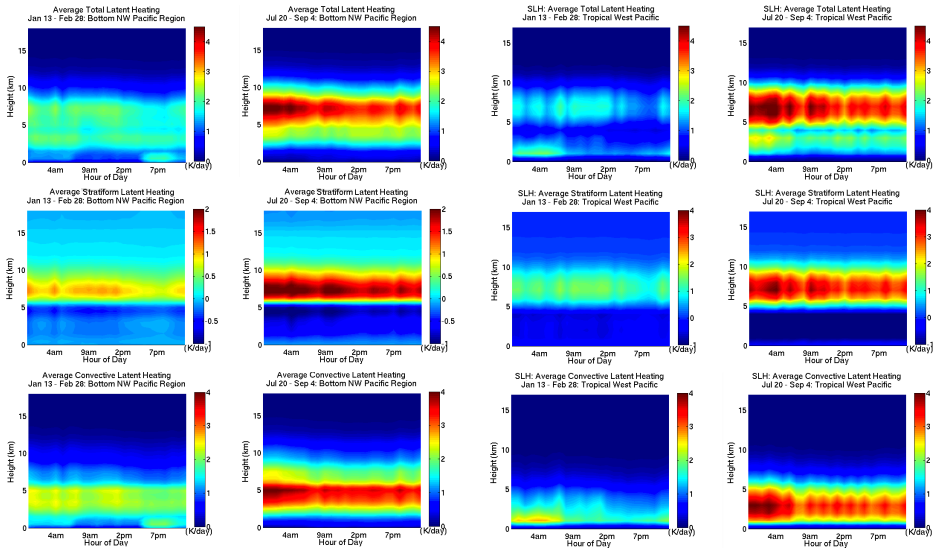

FIGURE 4.4: Tropical West Pacific – 13-year composite of average total *(top)*, stratiform *(middle)*, and convective *(bottom)* vertical latent heating structures in Period 1 and Period 5 for the TRAIN algorithm *(left)* and the SLH algorithm *(right)*. Units are in Kelvin per day.

The results of the FFT analysis summarized in Figure 4.5 show that the diurnal amplitude in the Tropical West Pacific is 4% in Period 1 and 5% in Period 5 based on TRAIN. The diurnal amplitudes based on the SLH algorithm are 19% in Period 1 and 11% in Period 5, suggesting stronger diurnal cycles in the

wintertime, opposite to what the TRAIN algorithm suggested. The SLH algorithm also generally produces much larger diurnal amplitudes than the TRAIN algorithm. These larger amplitudes may be due to higher instantaneous values of latent heating in SLH owing to the higher spatial resolution of the original PR measurements. The local time of maximum integrated total latent heating, represented by the phase, is 9am in Period 1 and 10am in Period 5 based on TRAIN, and 7am in Period 1 and 9am in Period 5 based on SLH. The fits from both algorithms plainly show larger amounts of integrated latent heating in July through September in the Tropical West Pacific. A study conducted by (Ling and Zhang, 2013) found that the western-central Pacific ITCZ is persistently strong throughout the entire year, except during January and February, which agrees with the larger amounts of heating in July-September in the Tropical West Pacific region.

4.1.1.2 Maritime Continent

The Maritime Continent has unique latent heating features compared to the other regions examined since the deeper and stronger latent heating occurs in NH winter, which corresponds to SH summer. The Maritime Continent region is the farthest south of all of the ocean regions, and is centered on the equator. Even though only the oceanic pixels are examined due to the limitations of the TRAIN algorithm, there is a distinct influence of several large islands that affect the resulting structure and evolution of latent heating in this region.

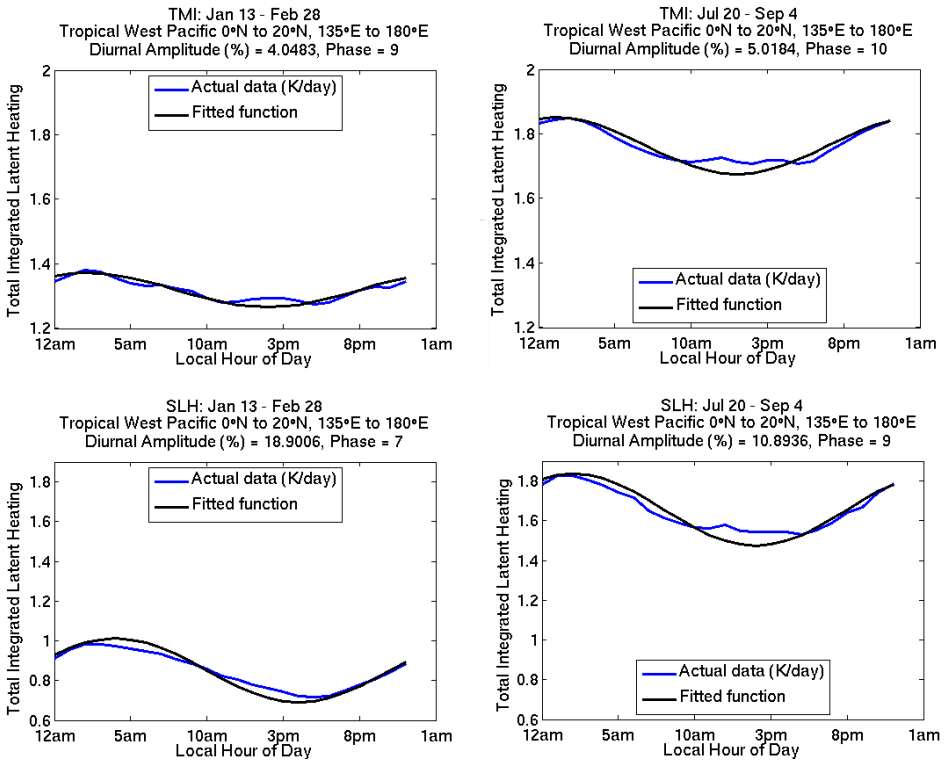

FIGURE 4.5: FFT fit to the diurnal cycle of the TRAIN integrated heating *(top)* and SLH integrated heating *(bottom)* in the Tropical West Pacific boxed region for Period 1 *(left)* and Period 5 *(right)*. Actual data is the blue line and the Fourier fit is the black line. Temporal smoothing was applied to the original data in these plots in order to make the comparisons easier to see. The diurnal amplitude and phase are summarized in the title of each plot.

In both algorithms and in both periods, there is clearly an early morning maximum in latent heating in the Maritime Continent region. There is good agreement between both algorithms in that there is more rainfall and latent heating in the Maritime boxed region in January and February than in July, August, and September. The greatest amount of heating based on the latent heating profiles occurs at an altitude of 7 km between the hours of midnight and 10am in January and February, and at a similar altitude between 3am and 9am

in July, August, and September. A difference between both algorithms in the total latent heating profiles is that there seems to be slightly more heating below 5 km in the SLH profiles than in the TRAIN profiles, likely due to the lower atmospheric convective latent heating in SLH. The maximum convective heating is situated at about 5 km above the surface in the TRAIN heating profiles, while it is situated lower in the atmosphere around 3 km in the SLH heating profiles. The convective heating at or below 5 km is reduced, but not entirely cancelled, by the cooling from the stratiform latent heating profiles leaving a peak heating around 5 km in the total latent heating.

The Fourier fits in Figure 4.7 show higher average integrated total heating in Period 1, which agrees with the latent heating profiles in Figure 4.6. The diurnal cycle in the Maritime region is considerably larger than in the Tropical West Pacific region, with amplitudes of 22% in Period 1 and 16% in Period 5 according to TRAIN and 30% in Period 1 and 24% in Period 5 according to SLH. Both heating algorithms agree very well with the phases in the Maritime Continent, confirming an early morning peak in precipitation intensity. The diurnal cycles peak at 5am in January-February and 6am in July-September based on TRAIN, and 6am for both periods based on SLH. Figure 4.8 shows the diurnal fits to the convective and stratiform portions of the total latent heating separately. The amplitude and phase of the integrated convective latent heating agree very closely with the amplitude and phase of the integrated total latent

heating. The integrated stratiform latent heating characteristic amplitude and phase do not match as well with the total latent heating fits, especially in the TRAIN fits. In the Maritime region according to TRAIN, the strength of the diurnal cycle and the local time of maximum stratiform latent heating are almost identical between January-February and July-September. Both periods have an amplitude of 11% and a local time of maximum stratiform latent heating at 2am. The SLH fits to the integrated stratiform latent heating look similar to the TRAIN and SLH fits of the integrated total latent heating, with a larger diurnal amplitude in Period 1 and phases of 5 am in both Periods 1 and 5.

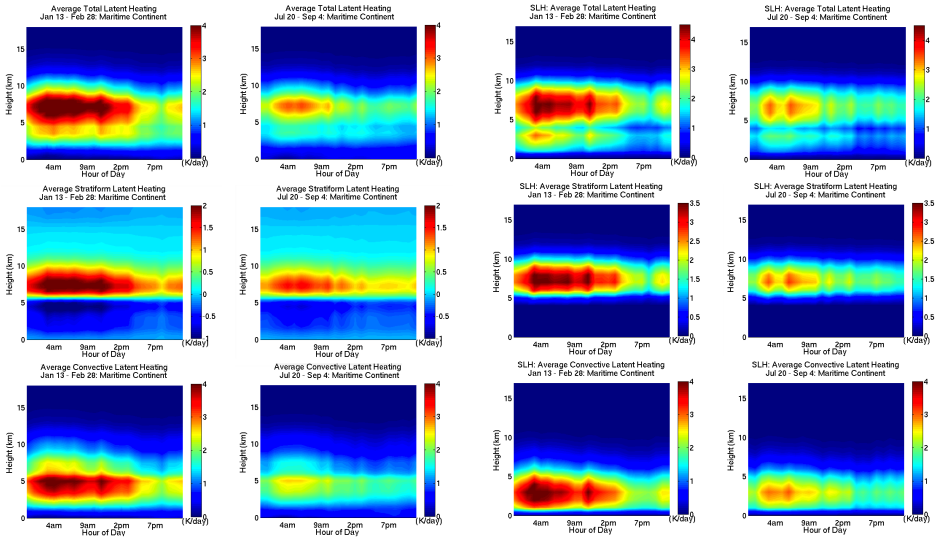

FIGURE 4.6: As in Figure 4.4 but for the Maritime Continent region.

The Tropical West Pacific and Maritime Continent regions are adjacent to each other, and in fact slightly overlap. One can see from Figure 4.2 that the rain that is initially located in the Maritime region in January-February moves

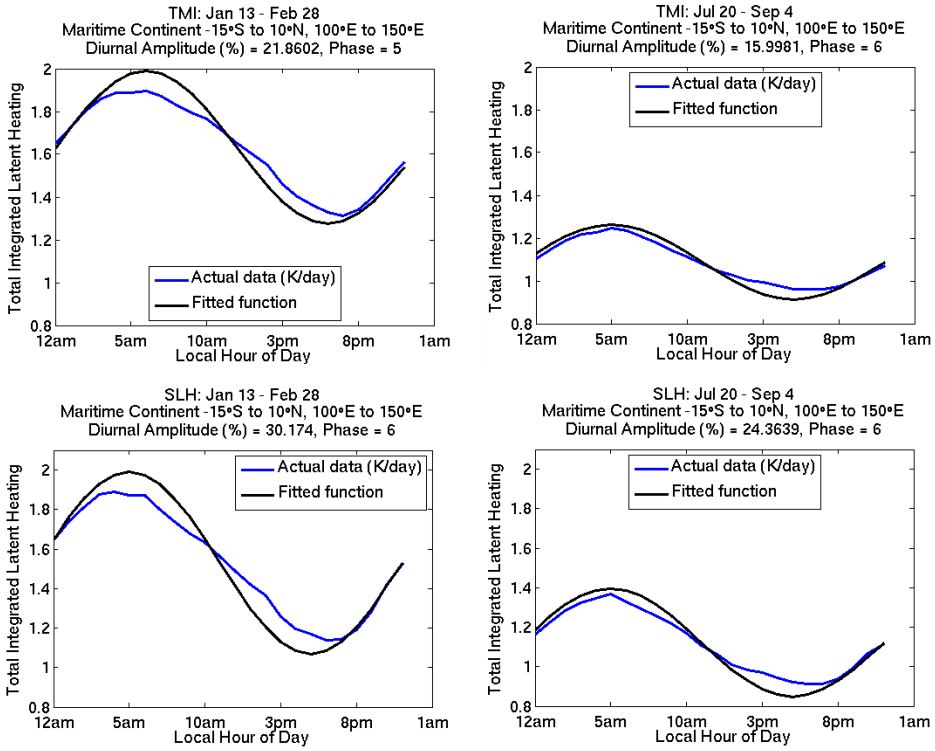

FIGURE 4.7: As in Figure 4.5 but for the Maritime Continent region.

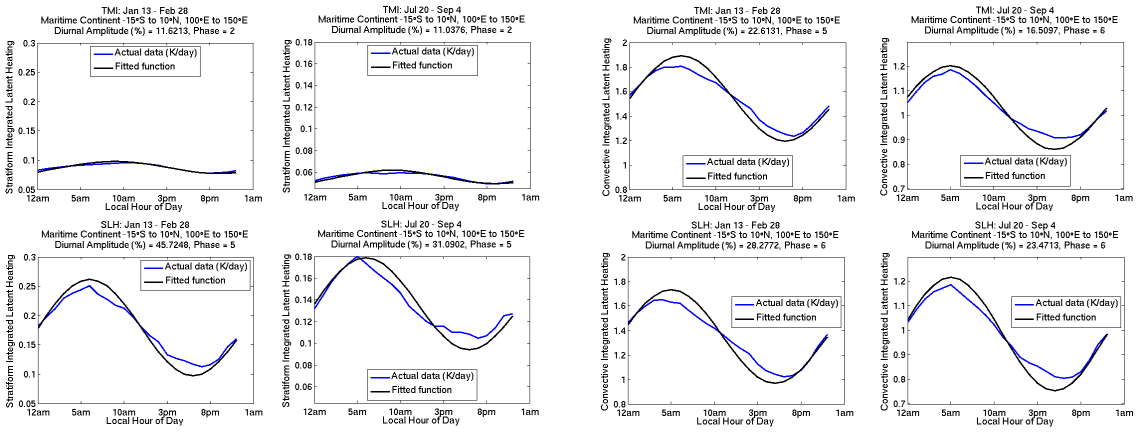

FIGURE 4.8: FFT fit to the diurnal cycle of the TRAIN integrated heating *(top)* and SLH integrated heating *(bottom)* in the Maritime Continent boxed region for Period 1 *(left)* and Period 5 *(right)*. Fits to integrated stratiform latent heating are on the left half, and fits to the integrated convective latent heating are on the right half. Actual data is the blue line and the Fourier fit is the black line. Temporal smoothing was applied to the original data in these plots in order to make the comparisons easier to see. The diurnal amplitude and phase are summarized in the title of each plot.

out of the region northward and into the Tropical West Pacific region in July-September. This likely explains the flip in the annual cycles between the Tropical West Pacific and Maritime Continent regions; that is, when the rain rates and latent heating are larger in one region, they tend to be smaller in the other. Figure 4.9 compares the amplitudes and phases of the diurnal cycles in each of the two regions for all periods. The amplitudes of the diurnal cycle in the Tropical West Pacific are 4-8% in TRAIN, and 10-20% in SLH, with the highest diurnal amplitude occurring in Period 6 in both datasets, which corresponds to September-October. The hour of maximum integrated total latent heating varies between 6am and 10am based on both algorithms and reaches the latest hour of 10am in July-September (Period 5) in TRAIN and June-July (Period 4) in SLH. Thus, the peak heating occurs around 10am local time in the Tropical West Pacific when the region receives more rain. In the Maritime Continent, the diurnal amplitudes vary from 15% to 25% and reach a maximum in January and February and a minimum in June-September based on the TRAIN algorithm. The SLH algorithm shows a similar annual cycle of the diurnal cycle strength in the Maritime region with a range of diurnal amplitudes between 25% and 35% and the weakest diurnal cycle similarly occurring in June-September. The phases for the Maritime Continent agree between both algorithms, with maximum latent heating occurring between 5am and 6am local time and remaining nearly constant throughout the year. The TRAIN algorithm shows a 5am maximum in all Periods except in Periods 4 and 5, which is when the diurnal cycle

weakens according to the fits and the phase becomes 6am local time. The SLH algorithm interestingly shows a constant phase of 6am local time all year long. The Maritime Continent has the most constant phases during the eight 47-day periods compared to all other ocean regions.

4.1.2 East Pacific

The East Pacific exhibits much greater lower-atmospheric heating in the TRAIN heating profiles than the Tropical West Pacific and Maritime Continent. A previous study found that systems over the east Pacific exhibit "a number of significant differences from those over the west Pacific warm pool including shallower clouds with warmer cloud tops, a larger proportion of stratiform rain, less ice for similar amounts of rainwater, and a radar bright-band or melting layer significantly farther below the freezing level" (Berg et al., 2002). In Figure 4.10, total heating peaks at about 3 km between midnight and 8am local time in the winter months based on the TRAIN algorithm. In the TRAIN heating profiles, the lower-atmospheric heating is present during all hours of the day and in both the winter and summer seasons. The larger amounts of total heating below the melting layer in the East Pacific could imply that the convective latent heating contributes more to the total diabatic heating than it does in other regions. It is important to note that the creators of the TRAIN dataset cautioned that the algorithm may have a high bias in the lower-atmosphere

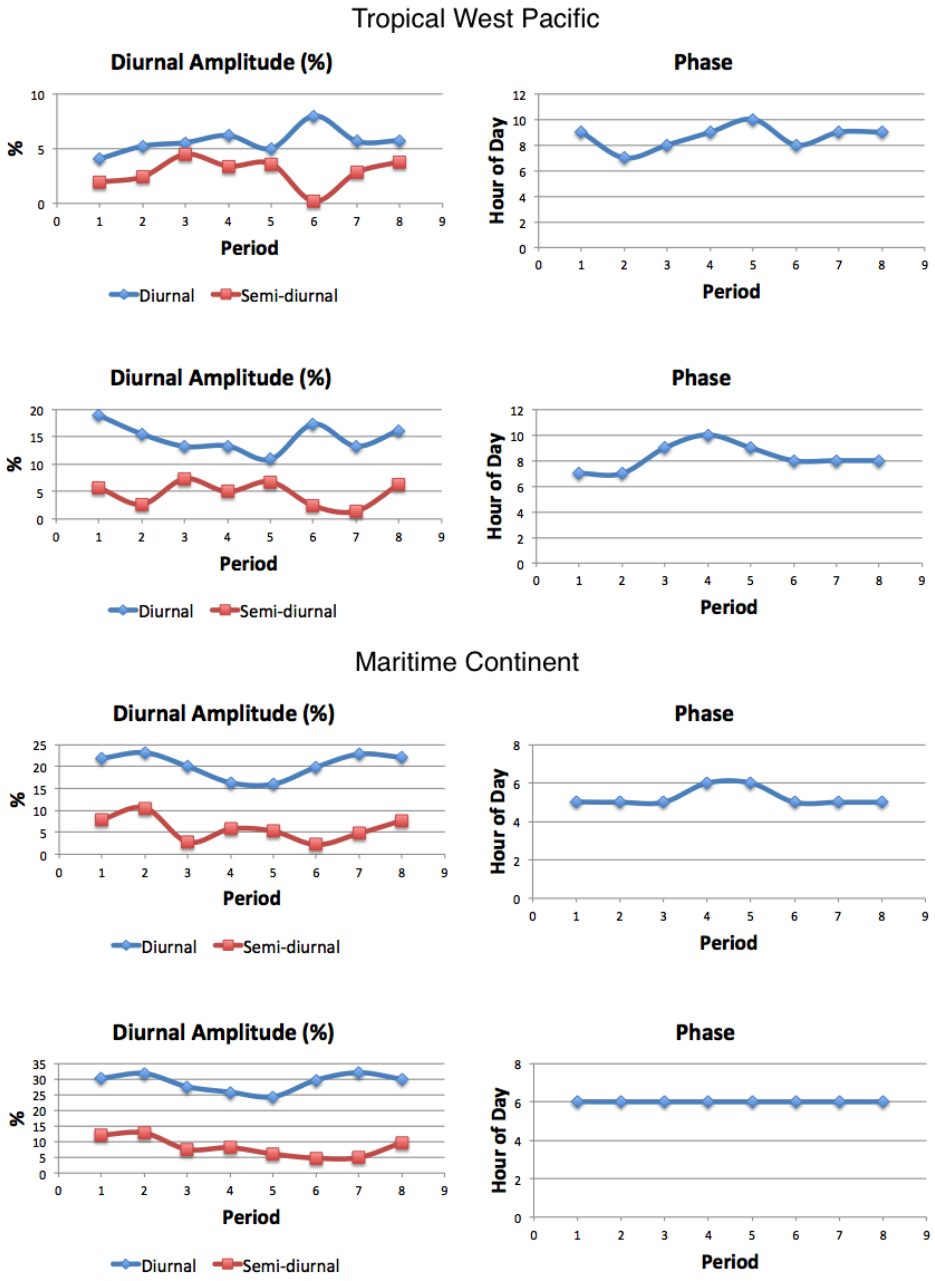

FIGURE 4.9: Tropical West Pacific *(top half)* and Maritime Continent *(bottom half)* – Diurnal amplitude percentages and semi-diurnal amplitude percentages *(left)* and phases *(right)* in military time of TRAIN integrated total latent heating *(top)* and SLH integrated total heating *(bottom)* for each of the eight 47-day periods averaged over 13-year period between 1998 and 2010.

in regions of shallow warm precipitation, such as the East Pacific (*NEWS Q1 dataset). The reason for the possible convective bias is the algorithm's difficulty in separating convective from stratiform heating structures at the coarse resolution of the TMI. One study that supports this lower-atmosphere convective bias found that "shallow convective heating in eastern Pacific may be overestimated by TRAIN algorithm" (Jiang and coauthors, 2009). There are higher amounts of heating in summer than in winter in the East Pacific according to TRAIN, and there is a summertime secondary peak of heating around 7pm local time. In other words, based on the TRAIN latent heating profiles, one might guess that the diurnal cycle is weaker in summer when there are multiple daytime peaks in heating.

The SLH heating profiles show some marked differences from the TRAIN heating profiles in the East Pacific. First, the total and convective heating is concentrated much higher in the atmosphere in the SLH than it is in TRAIN, which may have to do with the possible convective bias in the TRAIN algorithm. The convective latent heating profiles show the largest differences between algorithms, possibly owing to the higher spatial resolution of the TRMM PR or the more direct measure of convective activity provided by active radar reflectivity measurements. The convective heating in TRAIN is much deeper and stronger than it is in SLH. The maximum convective heating in SLH, however, is located closer to the surface than it is in the TRAIN algorithm. Regardless, the

SLH total heating profiles show clear morning maxima in heating between midnight and noon in both Periods 1 and 5. A study by (Nesbitt and Zipser, 2003) helps to confirm this early morning maximum in heating since it was found that the "majority of [ocean] boxes contain maxima from midnight to early morning hours."

According to the TRAIN fits in Figure 4.11, the diurnal cycle is comparable in the East Pacific in July-September when the diurnal amplitude is 4.9% than in January-February when the diurnal amplitude is 4.6%. The phase is the same between the winter and summer at 9am local time. The integrated latent heating appears to be greater in the summer which agrees with Figure 4.1 in that it shows a stronger ITCZ farther north in Period 5. SLH once again implies stronger diurnal cycles than TRAIN, with a stronger cycle in winter than in summer. Based on the SLH algorithm, the diurnal cycle peaks at 7am in Period 1 and 8am in Period 5. So both TRAIN and SLH algorithms agree in the early morning peak in heating in both winter and summer. Figure 4.12 illustrates that the highest diurnal amplitudes reach a maximum of about 7% in TRAIN and 25% in SLH in March and April (Period 2). It should be noted that this is the same time that the secondary ITCZ in the Southern Hemisphere appears within the East Pacific box based on Figure 3.1. The diurnal and semi-diurnal amplitudes are closest in April-June (Period 3) in TRAIN and SLH, suggesting that the diurnal cycle may not explain all of the variation in the East Pacific

during that time of year. The phase generally stays between 6am and 11am all year long in both algorithms. The fits from both algorithms have the latest time of maximum heating occurring between 9am and 11am in Periods 6 and 7, or September through December.

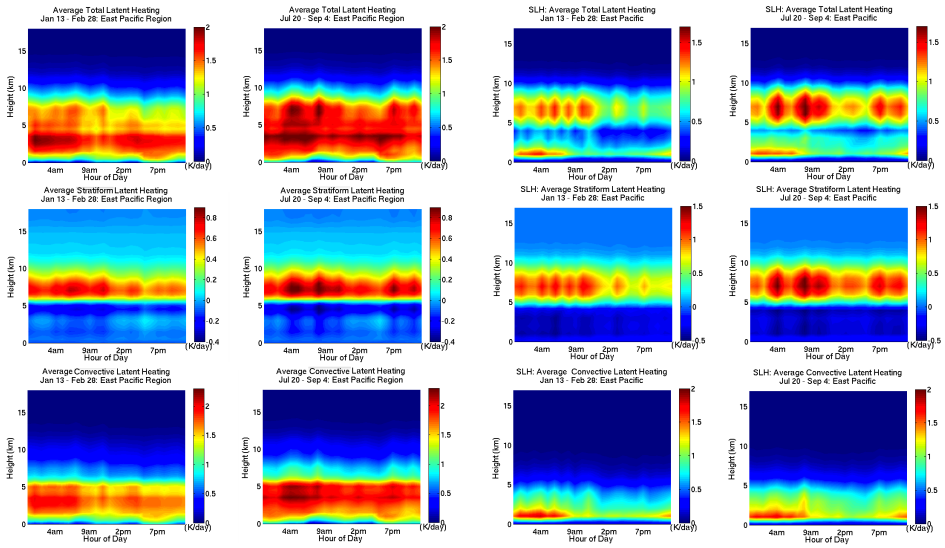

FIGURE 4.10: As in Figure 4.4 but for the East Pacific region.

4.1.3 Atlantic

The latent heating profiles in the Atlantic in Figure 4.13 exhibit some interesting features not present in other regions. The TRAIN profiles show that in January-February, there is very little heating throughout the entire layer with the exception of a thin layer right at the surface. A recent study also found that the Atlantic exhibits heating profiles that are more vertically confined (Ling

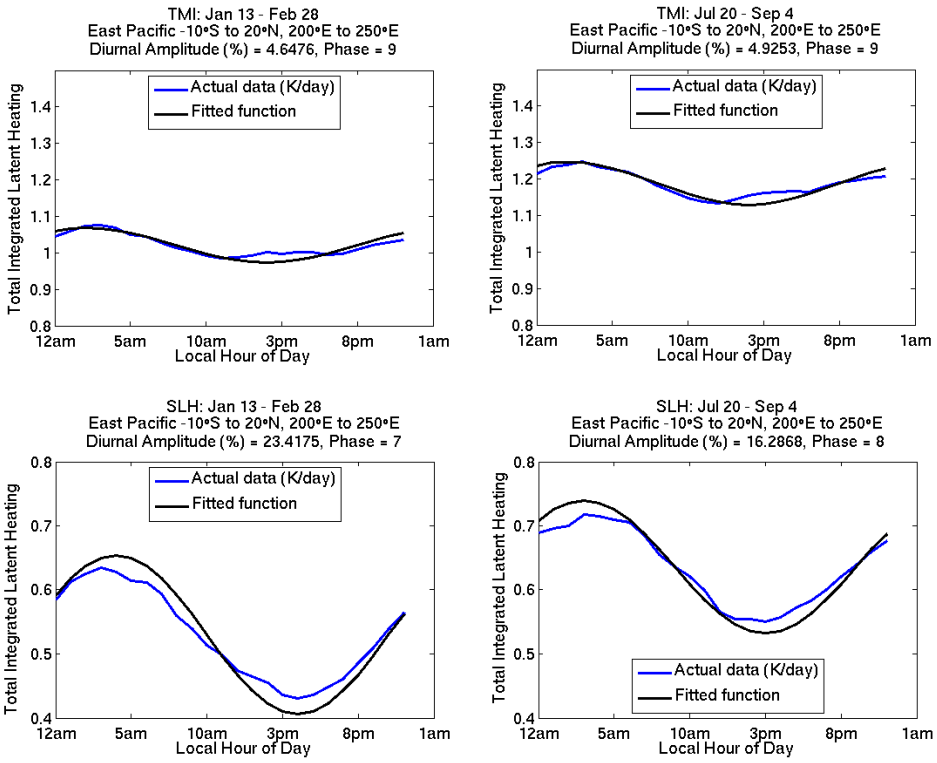

FIGURE 4.11: As in Figure 4.5 but for the East Pacific region.

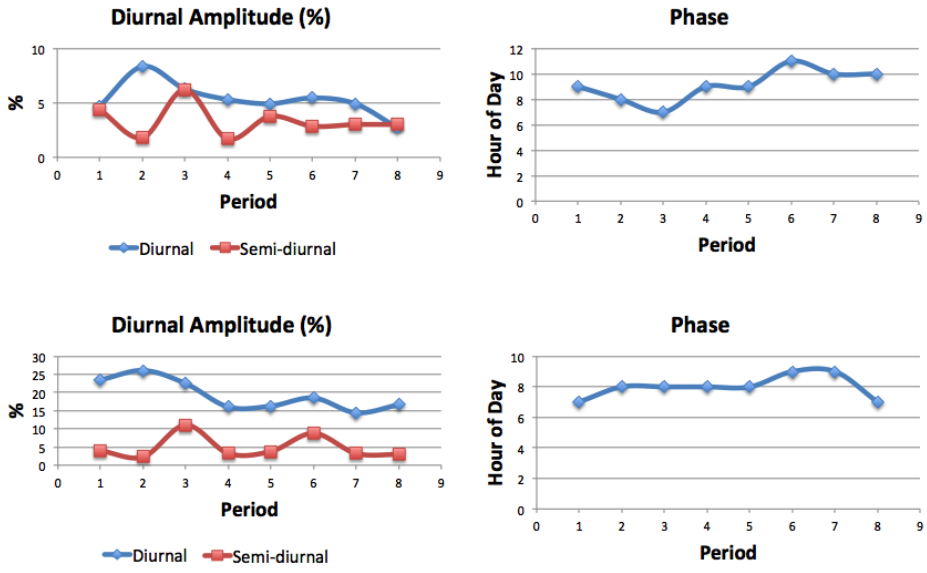

FIGURE 4.12: As in Figure 4.9 but for the East Pacific region.

and Zhang, 2013). There is a noticeable maximum in total latent heating between the surface and 1 km at 6pm in the winter according to TRAIN. In July-September, the maximum values of total latent heating oscillate every 2-3 hours in the morning between 4am and 11am at approximately 7 km. Figure 4.2 shows that there is almost no rain within the Atlantic box in winter, but the northern edge of the ITCZ drifts into the box in summer. The larger heating rates in the Atlantic form a deep layer between about 2 km and 7 km similar to that of the East Pacific, but with heating that is not as low in the atmosphere as what is seen in the East Pacific. The considerable differences in heating between Periods 1 and 5 in the Atlantic, therefore, demonstrate the effects of transitioning from a period of subsidence in winter to a period of convection in summer. It is also important to note that the TRMM satellite lacks sensitivity to light rain, and so it is likely there is some heat missing in the vertical profiles when lighter rain is the dominant form of precipitation. While this is true in all regions examined, it appears to be particularly important in the Atlantic in winter. The only difference in heating profiles between the TRAIN and SLH algorithm is that the convective heating is focused closer to the ground in the SLH algorithm.

There is a substantial difference in the average integrated total latent heating in Figure 4.14 between Periods 1 and 5 in the Atlantic, again agreeing with Figure 4.2. The diurnal amplitude from the TRAIN dataset is about 7% in January and February and about 4% percent in July, August, and September,

suggesting stronger diurnal variation in rainfall in the winter months. This is echoed in the SLH dataset where the diurnal cycle amplitudes are 19% in winter and 13% in summer. By examining the Fourier fits to the average integrated total latent heating in Figure 4.15 for Period 1, it is easy to see that the average integrated heating rates do not change much over the course of a day, only changing by about 0.1 Kday^{-1}. Figure 4.14 shows a maximum diurnal amplitude percentage in December and January (Period 8) in both algorithms in the Atlantic. The phase of the diurnal cycle also changes considerably from 7pm in March-April (Period 2) to 5am in April-June (Period 3), which is also when there is a large drop in the semi-diurnal amplitude based on the TRAIN dataset. The phase then gradually increases in both algorithms throughout the year to later times reaching approximately 9am in Period 8 before dropping again around Periods 2 and 3. The biggest disagreements between the algorithms is in the phases in Periods 1 and 2, when the TRAIN dataset suggests maximum latent heating occurs between 2pm and 7pm, whereas the SLH dataset suggests maximum heating occurs between 6am and 10am.

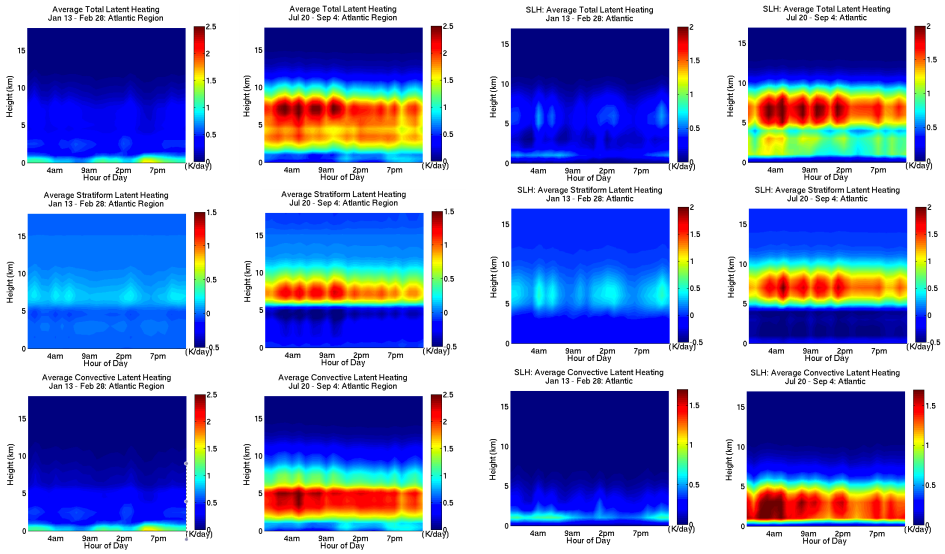

FIGURE 4.13: As in Figure 4.4 but for the Atlantic region.

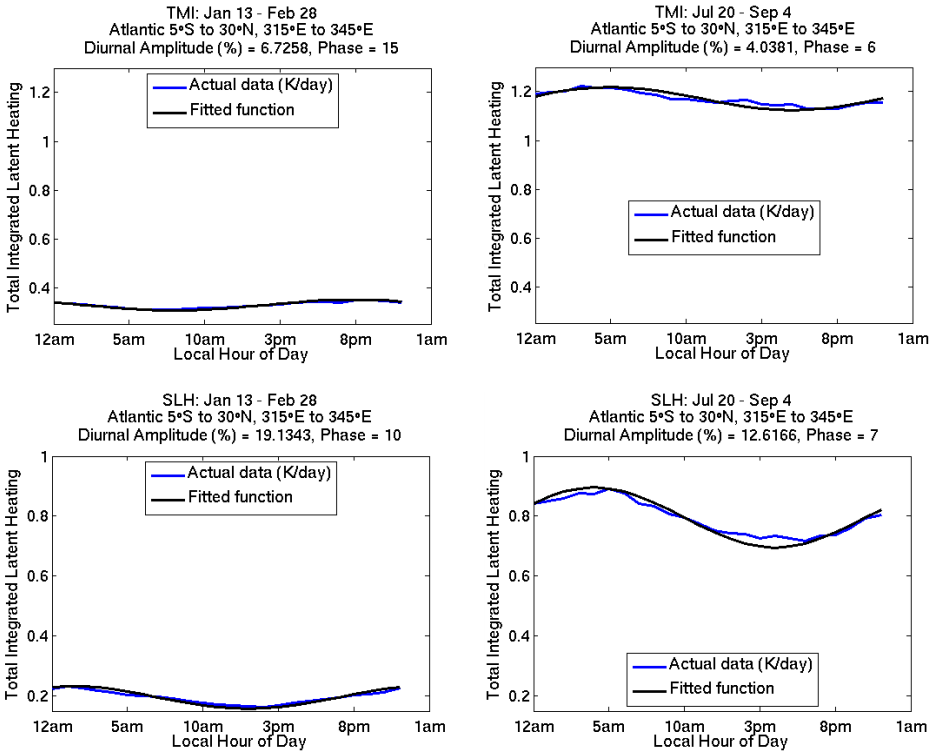

FIGURE 4.14: As in Figure 4.5 but for the Atlantic region.

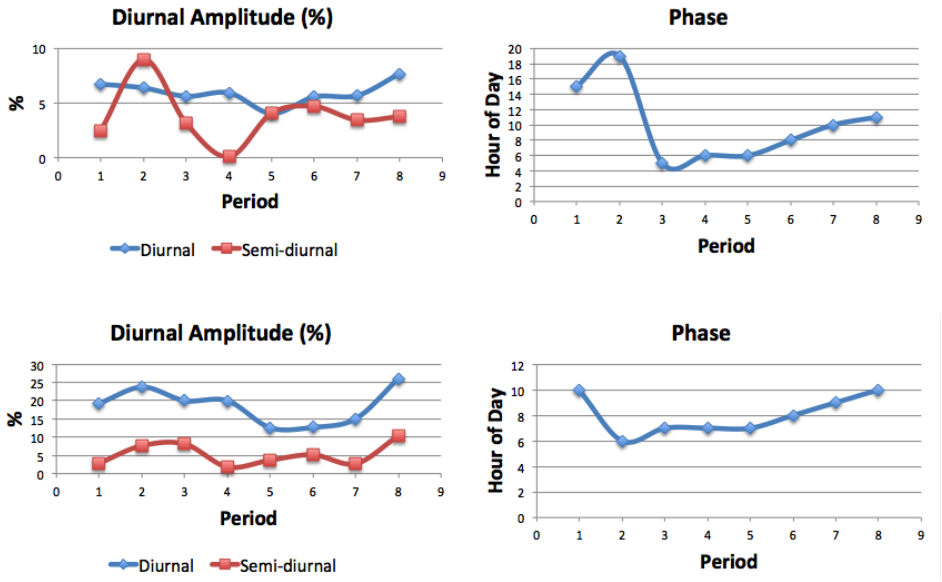

FIGURE 4.15: As in Figure 4.9 but for the Atlantic region.

4.1.4 Northwest Pacific

The mechanisms that drive precipitation variability in the Northwest Pacific are very different than those in the Tropical West Pacific, warranting a separate analysis of this region. In the Northwest Pacific, precipitation is influenced by tropical convection in summer and synoptic storm tracks in winter. In fact, (Ling and Zhang, 2013) found that "diabatic heating in the Northern Hemispheric storm tracks reach its maximum in January over both the Pacific and Atlantic Oceans." Figure 4.16 depicts how the vertical profiles of heating on average evolve during the day in the Northwest Pacific according to the TRAIN and SLH algorithms. Based on the latent heating profiles from TRAIN, the Northwest Pacific in January and February has a low-level peak in total latent heating

in the afternoon around 4-7pm. This afternoon peak may arise from the convective portion of latent heating also shown in Figure 4.16, which similarly peaks around 4-7pm. (Nesbitt and Zipser, 2003) found that the North Pacific north of 35° was the only boxed region that did not contain maxima from midnight to early morning hours, and instead had a peak in the evening. The complete opposite occurs in the TRAIN heating profiles in July, August, and September when there is a maximum in total latent heating at higher altitudes in the troposphere around 7 km stretching between 3am and noon. In the summertime, it appears the stratiform component of the total latent heating may dominate since the greatest latent heating occurs in the upper atmosphere. The stratiform cooling layer may cancel out the convective heating beneath 5 km. Based on the latent heating profiles from SLH, there is a peak in the morning hours in the July-September with heating concentrated higher in the atmosphere than it is in TRAIN. In January-February, however, the total latent heating is not focused quite as close to the surface as in the TRAIN algorithm. In all three SLH latent heating profiles, a clear maximum in latent heating occurs around 5am in winter, which differs from the evening maximum that was seen in the TRAIN algorithm profiles in Period 1. In the summer, the local times of maximum latent heating are similar between both algorithms between midnight and 9am.

Based on the Fourier fits to the diurnal evolution of the average integrated

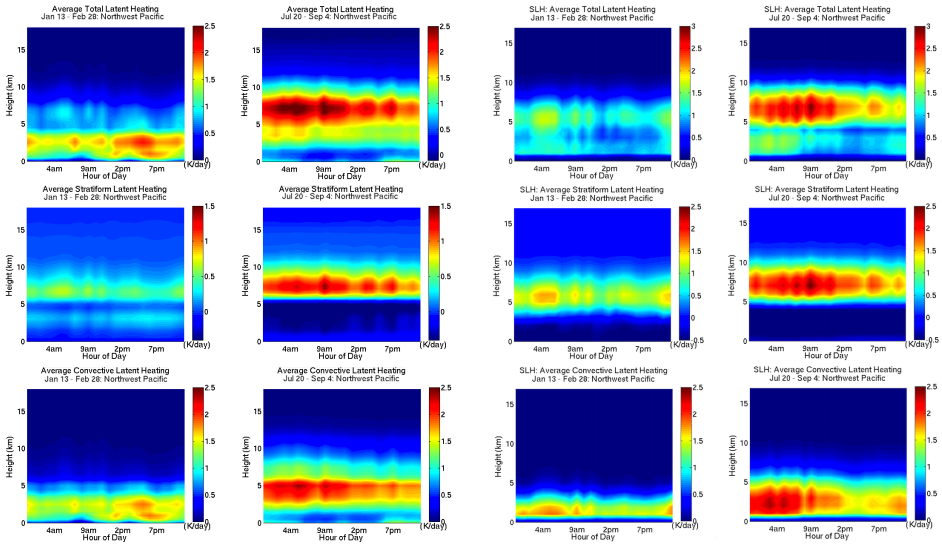

FIGURE 4.16: As in Figure 4.4 but for the Northwest Pacific region.

total latent heating in the Northwest Pacific boxed region in Figure 4.17, the diurnal amplitude percentages in the Northwest Pacific are 9% in the winter and 7% in the summer for the TRAIN dataset and 17% in the winter and 18% in the summer for the SLH dataset. Therefore both datasets show diurnal amplitudes that are close to each other between Period 1 and 5, but the datasets have opposite times of year for the larger amplitudes. The phases from TRAIN are 7pm in the winter and 7am in the summer and the phases from the SLH dataset are 8am in the winter and 7am in the summer. Therefore the algorithms agree more with each other in the phases in NH summertime when both algorithms give a phase of 7am local time. The diurnal amplitudes differ between algorithms likely due to the dependence of the amplitudes on the averages within the boxed regions. Mid-latitude cyclones and precipitation from frontal systems common in the winter in the Northwest Pacific may be captured differently between the TMI

and PR instruments, which may in turn influence the heating estimates.

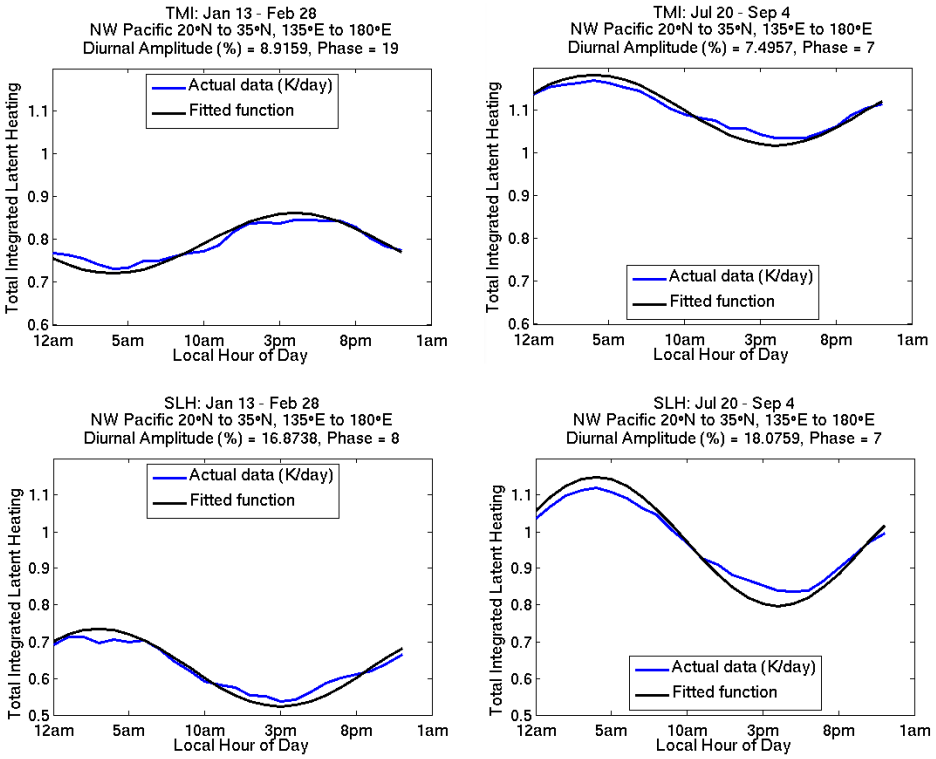

FIGURE 4.17: As in Figure 4.5 but for the Northwest Pacific region.

Based on Figure 4.18, the largest diurnal amplitude percentages along with the smallest semi-diurnal amplitude percentages for the integrated total heating occur in June-July, when the rain rates and heating rates are larger than in January-February. The diurnal amplitudes for the integrated total heating are much bigger in SLH, again likely due to the smaller spatial averaging from the PR compared to the TMI onboard TRMM, which results in the radar resolving larger values that are not averaged out by smaller surrounding values. The phase varies considerably throughout the year according to the TRAIN, but is relatively constant around 7am local time between June and October (Periods 4,

5, and 6) when the diurnal cycle is strongest based on the magnitudes of the diurnal amplitudes. The phases, according to the SLH algorithm, vary much less throughout the year and stay fixed between 6am and 9am local time. Both the TRAIN and SLH algorithms agree very well with the 7am maximum heating in Periods 4, 5, and 6 in the Northwest Pacific.

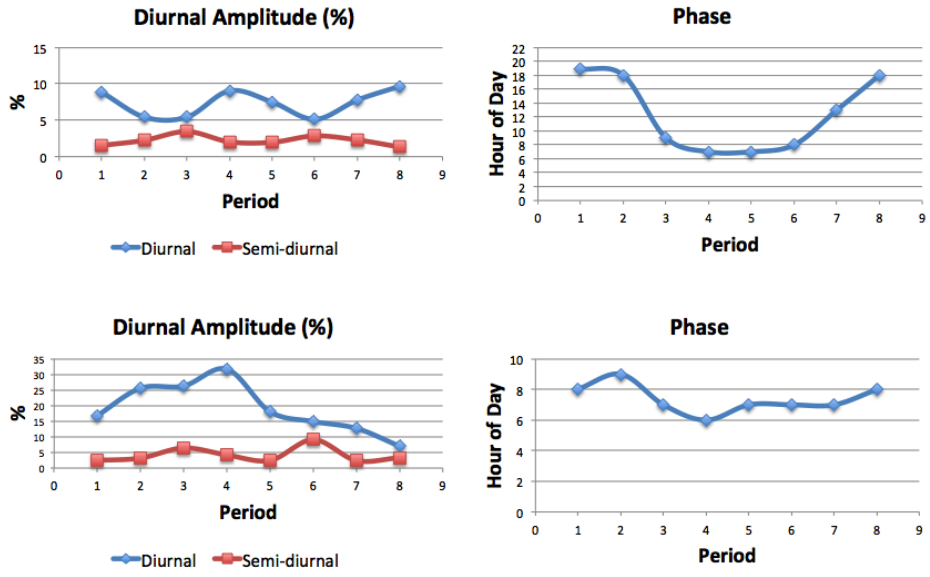

FIGURE 4.18: As in Figure 4.9 but for the Northwest Pacific region.

4.1.5 Central America

Like the Northwest Pacific, there is big difference between the winter and summer latent heating structures in the Central America region based on Figure 4.19. According to both TRAIN and SLH, the level of total maximum heating is higher in the atmosphere in the summer than it is in winter when the heating layer is shallow and concentrated closer to the surface. It is evident

in the TRAIN convective heating structures that in January-February there is a peak of heating very close to the surface in the evening around 7pm. In July-September, the convective heating maximum shifts to a higher altitude of 4-5 km and is strongest between 5am and 10am. The diurnal amplitude is much stronger in the summer (17%) as it is in the winter (3%) based on the TRAIN dataset as presented in Figure 4.20. The SLH fits similarly reveals a higher amplitude in summer (25%) than in winter (15%). The larger amounts of heating in the summer in the Central American region may be explained by the greater amounts of solar heating and convection over land as well as the northern shift and increased intensity of the ITCZ. Finally, based on Figure 4.21, the diurnal cycle is strongest in the Northern Hemisphere summer months (Periods 4 and 5) in the Central American region. The semi-diurnal amplitude is small when the diurnal amplitude is large. There is large seasonality in the strength of the diurnal cycle for Central America, especially in TRAIN. The phase varies between 3am and 8am local time during the course of a year according to both heating algorithms.

4.1.6 Comparing Ocean regions

The diurnal cycle amplitudes for all ocean regions from both TRAIN and SLH are shown in Figure 4.22 in order to compare the strength of their diurnal cycles. The diurnal amplitude fractions from TRAIN are lowest in June, July,

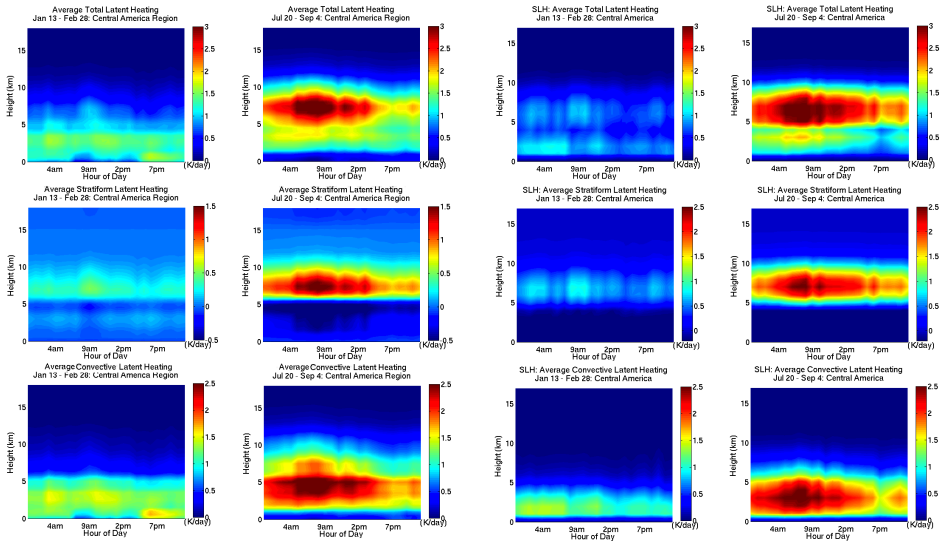

FIGURE 4.19: As in Figure 4.4 but for the Central America region.

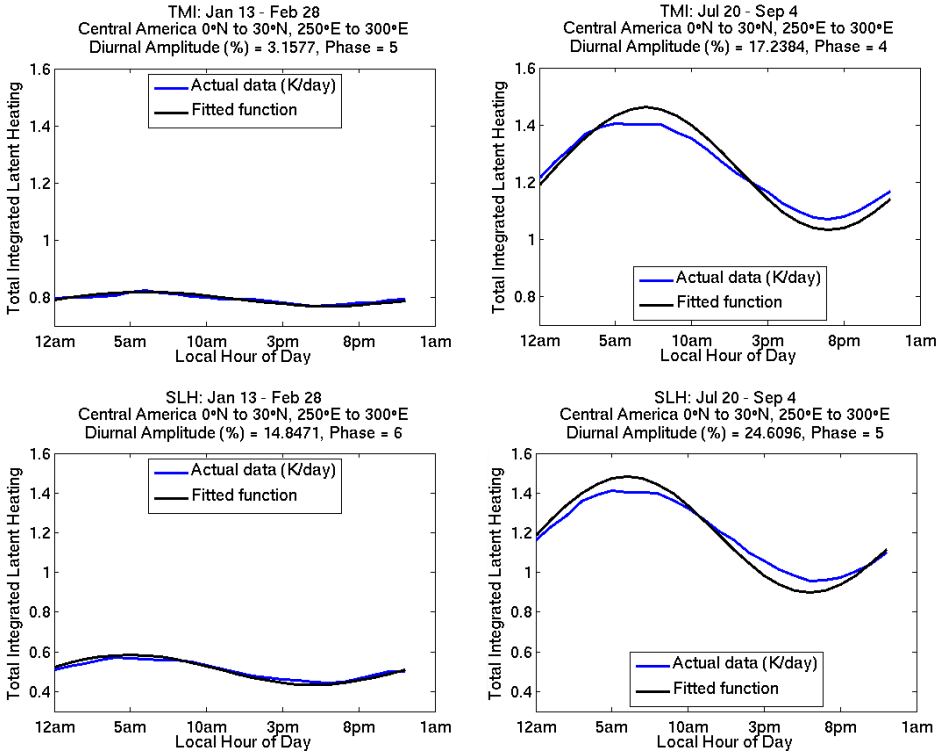

FIGURE 4.20: As in Figure 4.5 but for the Central America region.

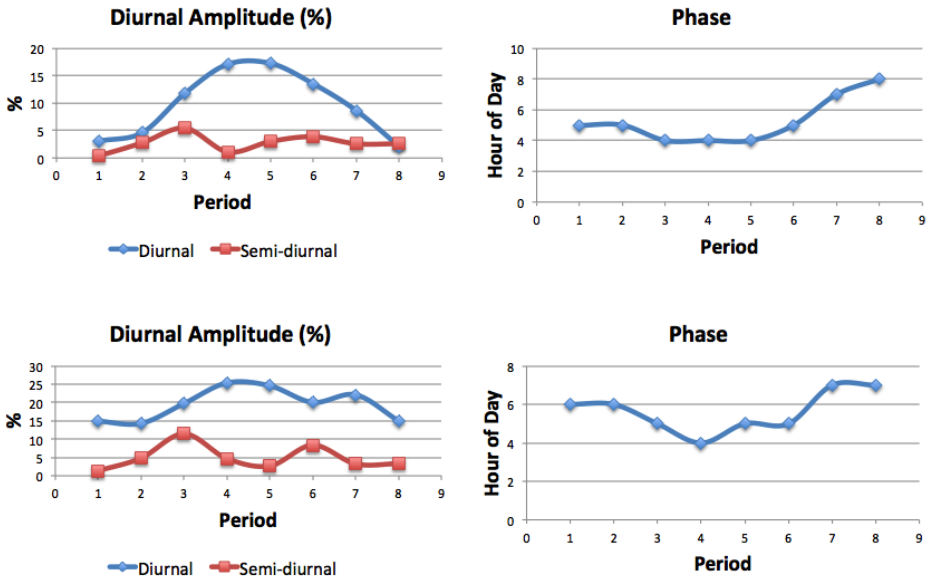

FIGURE 4.21: As in Figure 4.9 but for the Central America region.

and August in the Maritime, Tropical West Pacific, and the Indian regions. In Central America and the Northwest Pacific, the diurnal amplitudes percentages are highest in June, July, August, and September in both datasets. According to TRAIN, the strength of the diurnal cycle does not change much throughout the year in the Tropical West Pacific, Atlantic, and Indian regions. Conversely, SLH indicates larger variations of about 10% throughout the year for the three regions. The annual cycle of the strength of the diurnal cycle is largest in Central America, Northwest Pacific, and the Maritime Continent according to both algorithms. The smallest diurnal amplitudes were found in Central America and the East Pacific in Period 8 based on TRAIN and in the Northwest Pacific in Period 8 based SLH. The largest amplitudes were in the Maritime region throughout the year in both algorithms with the exception of the Northwest Pacific in

June-July (Period 4) from the SLH algorithm. In fact, the Maritime Continent region stands out with large diurnal amplitudes of almost double those of all other regions likely due to land influence. The biggest disagreement between heating algorithms was between the Northwest Pacific and the Atlantic, which were interestingly the highest-latitude boxed ocean regions. A recent study concluded that it is not uncommon for diurnal cycles to differ from the climatological average because of synoptic-scale weather patterns (Foster and Heidinger, 2013). The annual cycle of the strength of the diurnal cycle matched the best between both algorithms for the Tropical West Pacific, East Pacific, Maritime, and Central American regions – all regions close to the equator. The diurnal amplitude did not vary by a large percentage (greater than 20%) over the annual cycle for any of the ocean regions. This finding agrees with a study conducted by (Nesbitt and Zipser, 2003) where they found that "for features with and without ice scattering over the ocean, the amplitude of the diurnal cycle is remarkably similar for all regions and the amplitude never varies by more than about 20% for any region."

The phases from both heating algorithms for the seven ocean regions and for all eight of the 47-day periods are also shown in Figure 4.22. Interestingly, the phases for the ocean regions all lie between 4am and 10am in April-October (Periods 3-6) in both algorithms. In fact, the phases for all ocean regions are remarkably consistent according to the SLH dataset throughout the year. The

early morning peak in latent heating is consistent with previous efforts to document the diurnal rainfall over oceans. For example, a study using rain gauge measurements has shown substantial oceanic nocturnal maximum of precipitation (Nesbitt and Zipser, 2003). The same study also found afternoon minima in oceanic precipitation "through the absorption of shortwave radiation by upper portions of the convective anvils, which increases the static stability in cloudy regions, weakening vertical motions" (Nesbitt and Zipser, 2003). The nighttime increase in rainfall has been attributed to a decrease in stability due to longwave cooling at night, which leads to cloud development and enhanced convection (Eastman and Warren, 2014, Nesbitt and Zipser, 2003). More recently, (Taylor, 2012) found that the diurnal cycle of longwave cloud forcing maximizes near 6am local time, further supporting the idea of decreased stability due to longwave cooling at night. Nesbitt et al (2003) concluded that it is not that it is raining harder at night, but rather that there is a larger area covered by rain caused by an increase in a number of systems. Only the Northwest Pacific in October-April (Periods 1, 2, 7, and 8) and the Atlantic in January-February (Periods 1 and 2) in the TRAIN dataset digress from this early morning maximum rainfall and integrated heating. Another study discovered that "near-continent variations in the diurnal cycle have been linked to coastline effects and gravity wave forcing by the nearby continental diurnal cycle", which may help to explain some of the distinct diurnal cycles of ocean regions that include land such as the Atlantic (Nesbitt and Zipser, 2003).

Figure 4.23 presents these results in a slightly different way illustrating how the TRAIN rainfall in each ocean region varies both diurnally and seasonally. It is apparent that for almost all ocean regions, the largest rain rates tend to occur in the morning and also during July-October (Periods 5 and 6), which correspond to July through October. The only region that does not have a rainfall maximum in July-October according to the plots is the Maritime Continent region, which has a rainfall maximum in December-April. Again, this deviation of the Maritime Continent region from all other ocean regions may be because the other regions reside almost entirely in the Northern Hemisphere whereas the Maritime region partly resides in the Southern Hemisphere. All of the ocean regions, though, clearly have maximum in precipitation in the morning during most times of year. In the Atlantic region, substantial rain quickly appears in Periods 4-7 and then disappears in Periods 8,1,2 and 3, again illustrating a transition from convection to subsidence. There also appears to be strong heating throughout most hours of the day between June and October, but there is noticeably more intense rainfall in the early morning hours centered around 5am. Figure 4.24 shows similar color plots for all ocean regions, but for the integrated total latent heating instead of the rain rates from both TRAIN and SLH. There is qualitatively good agreement between all ocean regions, with the exception of perhaps the Northwest Pacific.

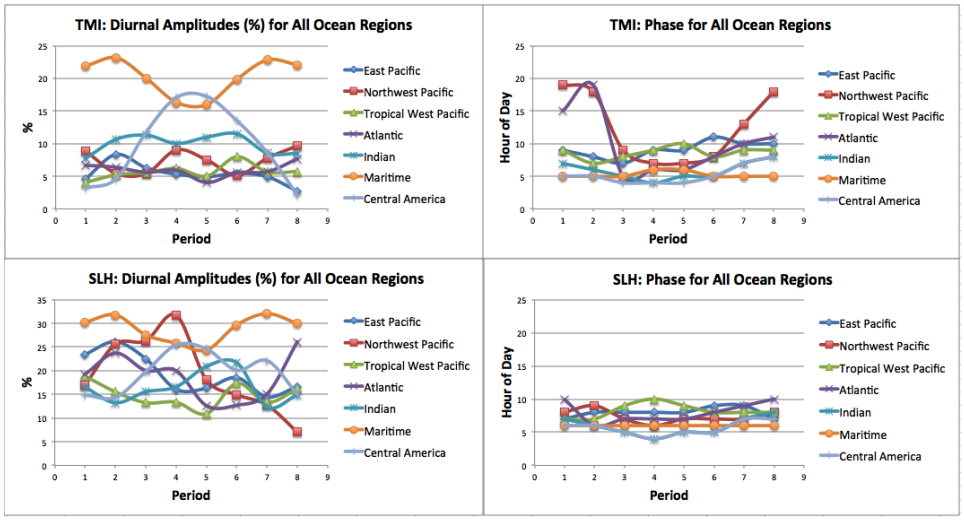

FIGURE 4.22: The annual cycle of diurnal amplitudes *(left)* and phases *(right)* from the TRAIN algorithm *(top)* and the SLH algorithm *(bottom)* for each of the seven ocean-boxed regions and for each of the eight 47-day periods for 1998-2010.

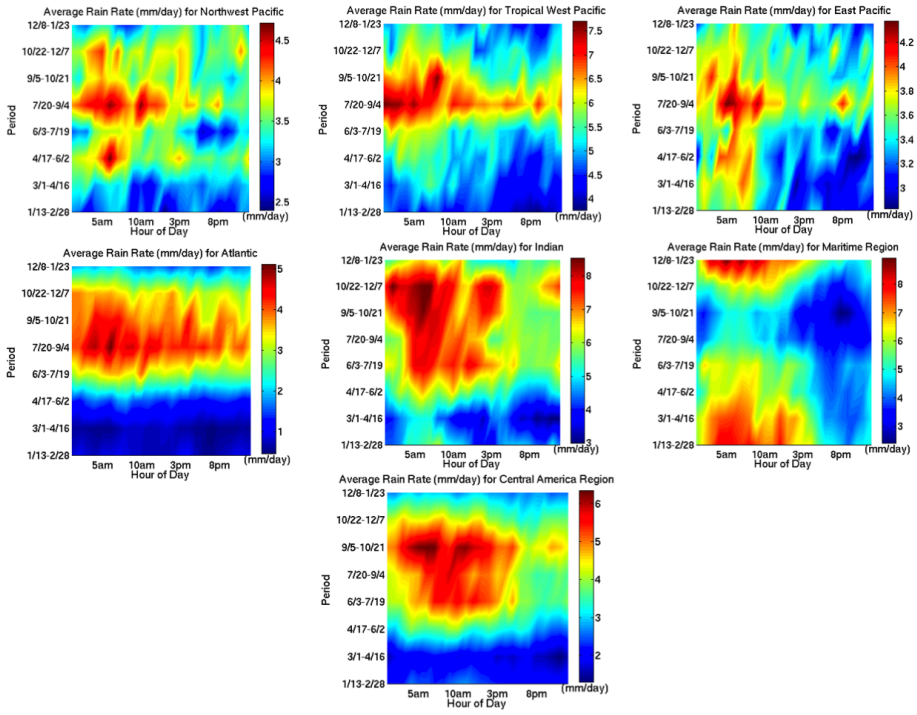

FIGURE 4.23: Plots of diurnal cycle and seasonal cycle of rain rates for all of the seven ocean regions from the TRAIN algorithm with hour of day on the x-axis and seasonal cycle of eight 47-day periods on y-axis. Note: Color scales differ between regions. Regions include Northwest Pacific, Tropical West Pacific, East Pacific, Atlantic, Indian, Maritime, and Central America.

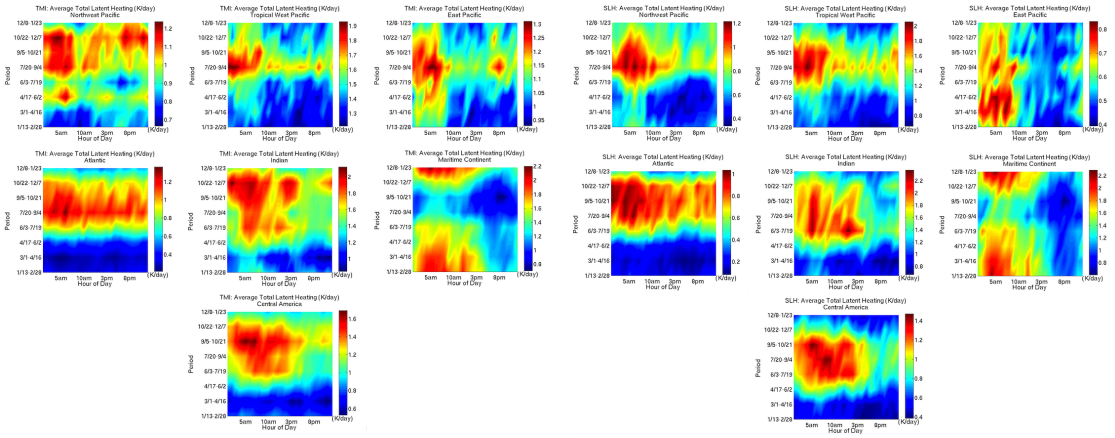

FIGURE 4.24: Plots of diurnal cycle and seasonal cycle of integrated total latent heating for all of the seven ocean regions from TRAIN algorithm *(left)* and SLH algorithm *(right)* with hour of day on the x-axis and seasonal cycle of eight 47-day periods on y-axis. Note: Color scales differ between regions. Regions include Northwest Pacific, Tropical West Pacific, East Pacific, Atlantic, Indian, Maritime, and Central America.

4.2 Latent Heating Over Land

Land regions are of particular interest to study since research has shown that there is "significant seasonality over land regions and weak seasonality over oceans" (Taylor, 2012). Not only do the seasonal cycles differ between land and ocean, but there are also "much smaller diurnal cycles over isolated ocean areas than over land areas" (Nesbitt and Zipser, 2003). The land regions chosen in this study include the Amazon, Congo, and India as seen in Figure 4.25. The Indian region was specifically chosen in order to analyze the monsoon cycle. The Amazon and Congo regions were chosen since both regions are close to the equator and see copious amounts of rainfall during different times of year based on the integrated heating maps in Figure 3.8. It is worth noting that

a previous study done by (Nesbitt and Zipser, 2003) found that "tropical and subtropical Africa, and tropical South America have the strongest amplitudes, with the African regions having the strongest amplitudes in the category with ice scattering." The Amazon and Congo are ideal regions to contrast since the Amazon region features rainforests while the Congo region features more dry and arid conditions. Both the Amazon and Congo are located in the Southern Hemisphere, and so January-February corresponds to the summertime in those regions while July-September corresponds to the wintertime. All figures relevant to each of the three land regions are included in Appendices H-J located at the end of this paper. Table 4.3 contains the specific latitude and longitude coordinates of the land regions and Table 4.4 shows the sampling in each land region in units of millions. Even though there are fewer observations due to the smaller swath width of the PR and also due to smaller user-defined land boxes, there remains hundreds of thousands of observations in each region providing an adequate sample to analyze.

Past studies suggest that rainfall and convection should reach a maximum in the afternoon and evening hours due to daytime solar heating over land. For example, (Nesbitt and Zipser, 2003) found that "land areas have a much larger rainfall cycle than over the ocean, with marked minimum in the midmorning hours and a maximum in the afternoon." Afternoon and evening maxima over land differs from oceans where there is early morning maxima in rainfall and

latent heating. Land surfaces have varying surface emissivities and varying elevations which can lead to more noisy and spatially-variable rainfall measurements. Additionally, land surfaces have smaller heat capacities than ocean surfaces, and so land heats up and cools off much quicker in the same amount of time than an ocean surface would.

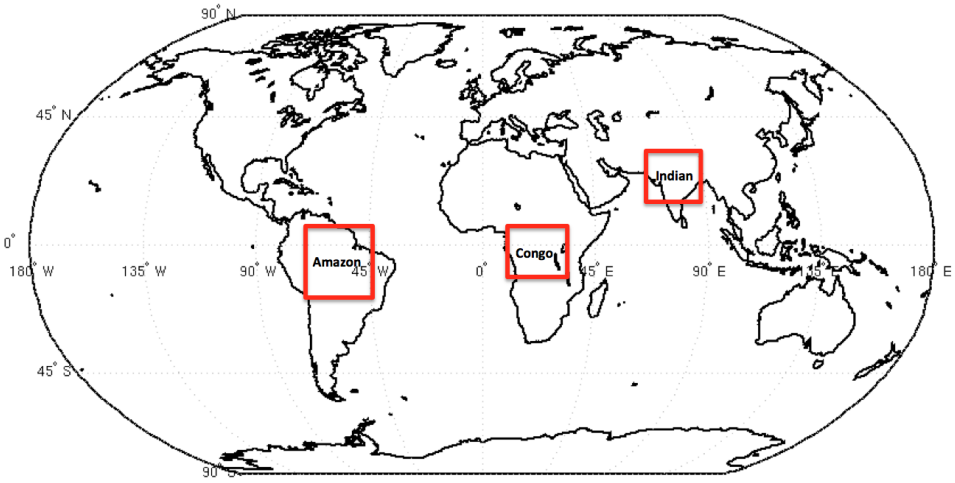

FIGURE 4.25: Land regions chosen to analyze latent heating profiles estimated from the SLH algorithm. Regions chosen are Amazon (15°S-5°N, 70°W-45°W), Congo (10°S-5°N, 10°E-30°E), and Indian (15°N-30°N, 67°E-85°E).

TABLE 4.3: User-defined latitude and longitude limits for the three land regions.

Land Region	**Latitudes**	**Longitudes**
Amazon	15°S-5°N	70°W-45°W
Congo	10°S-5°N	10°E-30°E
Indian	15°N-30°N	67°E-85°E

TABLE 4.4: Total number of observations in units of millions for the three land regions for the SLH algorithm for each of the eight 47-day periods. Number of observations within a box will depend on the size of the box, which differs between different regions. Land regions chosen were smaller than all ocean regions.

SLH: (x10^6)	Period 1	Period 2	Period 3	Period 4	Period 5	Period 6	Period 7	Period 8
Amazon (land)	0.53	0.54	0.53	0.52	0.52	0.47	0.53	0.53
Congo (land)	0.32	0.32	0.32	0.31	0.31	0.28	0.32	0.32
Indian (land)	0.39	0.39	0.39	0.38	0.38	0.34	0.39	0.39

4.2.1 Amazon and Congo

The latent heating profiles presented in Figure 4.26 for the Amazon region show significant differences in the maximum latent heating between January-February and July-September, with more intense latent heating in January-February. The total latent heating during SH summer is higher in the atmosphere at around 7 km until 2pm when there is a sudden increase in convective heating around 3 km. In fact, if one examines only the convective latent heating in the Amazon in Period 1, it is obvious that there is a peak around 2pm and that there is virtually no convective heating during all other hours of day. This afternoon peak in convective latent heating likely derives from "pop-up" convection that is brought about by daytime solar heating. The solar heating in the Amazon region would be stronger in January-February than in July-September since January-February corresponds to summer in the Southern Hemisphere. In winter (July-September) in the Amazon, the total latent heating is much weaker but is also more isolated to the afternoon hours than it was in the summertime,

when total latent heating was strong during most hours of the day in the upper-atmosphere. Interestingly, there is almost no stratiform latent heating throughout the day in July-September in the Amazon, a fact that agrees with the lack of upper-atmospheric heating in the total heating profiles. This absence of stratiform latent heating in Period 5 is very different from the stratiform heating profiles in Period 1, where there is strong stratiform latent heating during most of the day. There is an afternoon peak of total latent heating between about 1 km and 7 km at around 2pm local time in the Amazon during both Periods 1 and 5.

The vertical structures of total, stratiform, and convective heating in Congo (Figure 4.26) are similar to what is in the Amazon. Convective latent heating is once again concentrated between 2 km and 6 km and maximizes around 3pm local time, an hour later than the local time of maximum in the Amazon. There are also smaller amounts of convective and total latent heating in the morning in the Congo region compared to the Amazon. The stratiform latent heating once again appears during all times of day as it does in the Amazon, but in the Congo region there is a more obvious maximum in the morning between midnight and 4am. This maximum stratiform latent heating in the morning is what contributes to the weak amounts of total latent heating in the morning in the Congo region. Despite the weak total latent heating in the morning, there still appears to be a noticeable maximum of approximately 6 Kday^{-1} at about

3pm in both Periods 1 and 5 in the Congo region. One distinction between the Amazon and Congo regions is that the latent heating in the Congo region is not as smooth and is spottier than it is in the Amazon region. The afternoon peak of total latent heating in SH summer is also deeper in the Amazon than it is in Congo. There is evidence that both the Amazon and Congo exhibit stronger diurnal cycles with an afternoon maximum in Period 5.

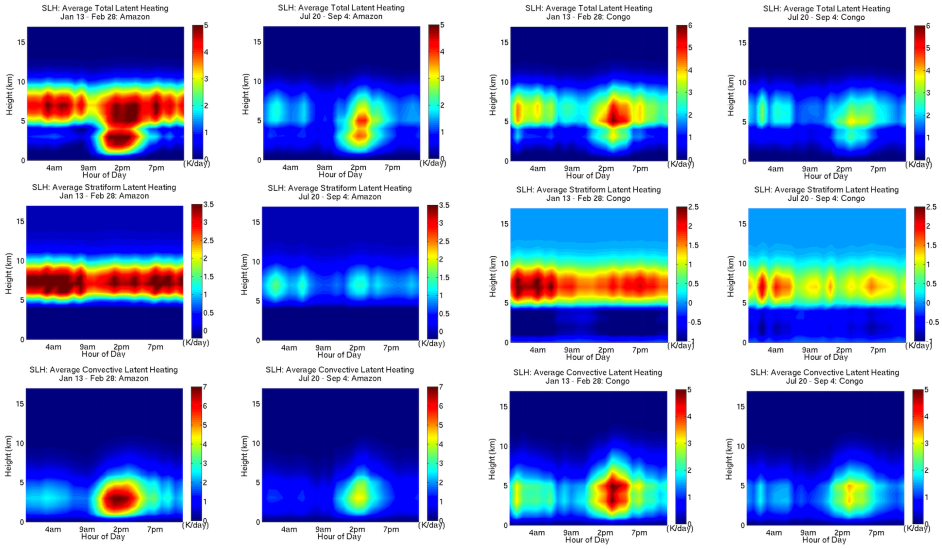

FIGURE 4.26: Amazon and Congo – 13-year composite of average total *(top)*, stratiform *(middle)*, and convective *(bottom)* vertical latent heating structures in Period 1 and Period 5 for the SLH algorithm for the Amazon region *(left)* and the Congo region *(right)*.

In stark contrast to the oceanic regions presented earlier, the FFT fits to the diurnal cycles of integrated total heating in Figure 4.27 evidently show an afternoon maximum in integrated total latent heating around 3pm-5pm local time for both land regions. According to the amplitudes and phases, the Amazon region has a more pronounced diurnal cycle in July-September with a diurnal amplitude of about 51% than in January-February when the diurnal amplitude

is about 43%. The phases for the Amazon region according to the fits are at 9pm local time for both winter and summer. The fits for the Congo region also show a stronger diurnal cycle in July-September based on diurnal amplitude percentages. In both winter and summer, the diurnal cycle in the Congo region is weaker than in the Amazon. There is also considerably less annual variation in the amplitude of the diurnal cycle in Congo with only a 3% difference between Periods 1 and 5. The phase of the diurnal cycle in the Congo region is very similar to that in the Amazon, peaking at 8pm local time.

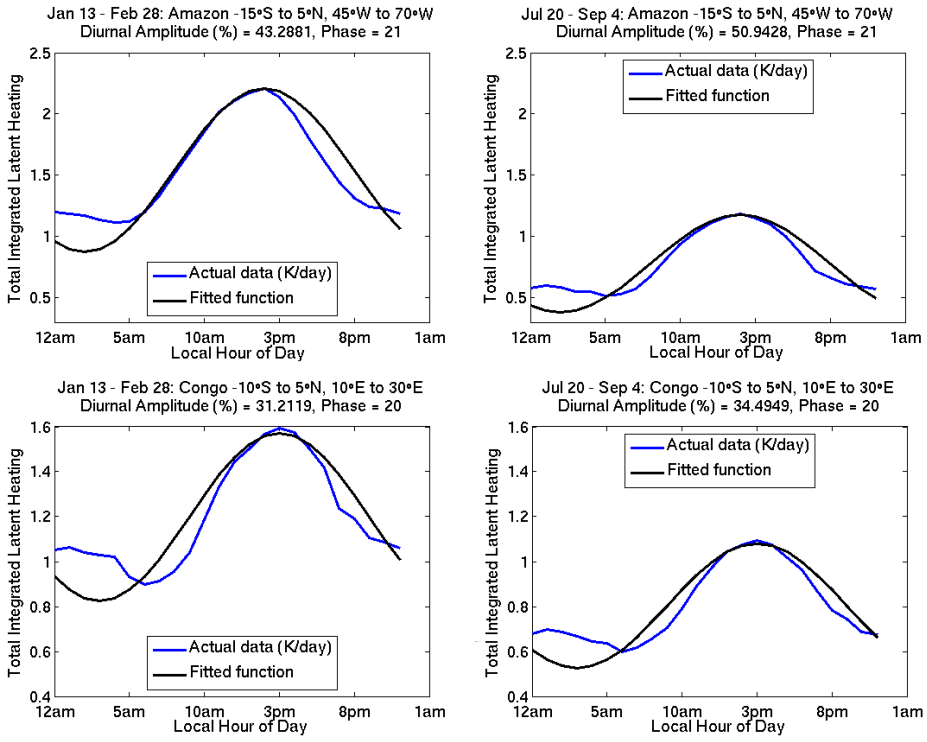

FIGURE 4.27: FFT fit to the diurnal cycle of the SLH integrated heating in the Amazon *(top)* and Congo *(bottom)* boxed region for Period 1 *(left)* and Period 5 *(right)*. Actual data is the blue line and the Fourier fit is the black line. Actual data is the blue line and the Fourier fit is the black line. Temporal smoothing was applied to the original data in these plots in order to make the comparisons easier to see. The diurnal amplitude and phase are summarized in the title of each plot.

An examination of the annual cycle of diurnal amplitudes based on Fourier fits in Figure 4.28 reveals similar magnitudes between the diurnal amplitudes and the semi-diurnal amplitudes for both the Amazon and Congo regions. This suggests that the diurnal cycle is not the sole factor modulating precipitation and latent heat release in these regions. In April through September (Periods 3, 4, and 5) especially, both Congo and the Amazon exhibit semi-diurnal amplitudes that equal or almost equal the diurnal amplitudes. The diurnal cycle tends to dominate during all other periods from September to April, which is the summer in both regions.

The evolution of the daytime peaks throughout the year differs between the Amazon and Congo. In the Amazon, the 9pm peak persists in Periods 1-7 before shifting an hour later to 10pm during Period 8. The phases in Congo start at 8pm in Period 1 but shift an hour earlier to 7pm in Period 2, and then to 6 pm in Periods 3-4. In July through January, or Periods 5-8, the phase returns again to 8pm. Thus, the diurnal cycle peaks earlier during the annual cycle and exhibits more variation throughout the year in Congo than it does in the Amazon.

4.2.2 Indian monsoon

India is an interesting region to study since the rainfall and latent heating variability is tightly coupled to the monsoon. The Indian monsoon is a

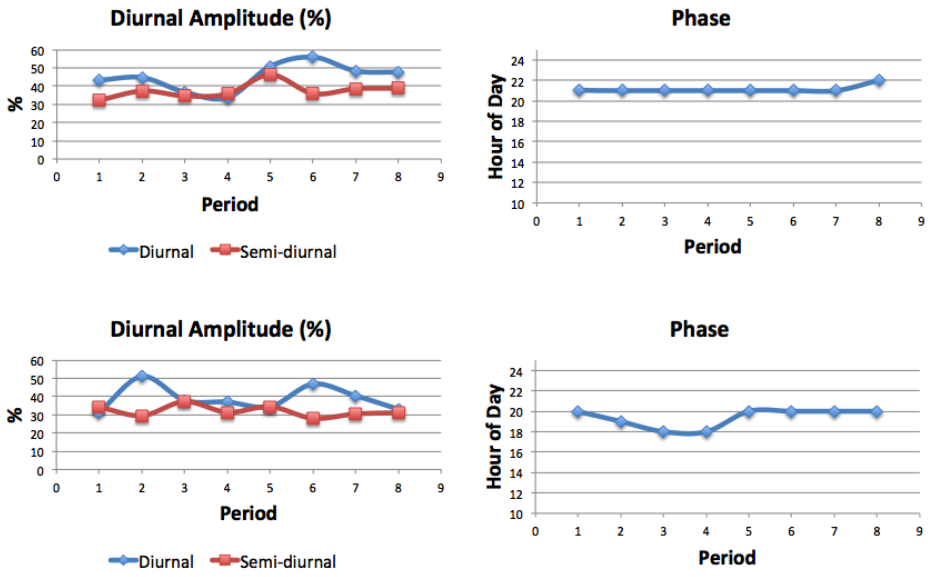

FIGURE 4.28: Amazon and Congo – Diurnal amplitude percentages and semi-diurnal amplitude percentages *(left)* and phases *(right)* in military time of the SLH integrated total latent heating for each of the eight 47-day periods averaged over 13-year period between 1998 and 2010 for the Amazon *(top)* and Congo *(bottom)*.

large-scale circulation pattern that brings India the vast majority of its annual rainfall between June and September. The timing, strength, and duration of the monsoon are intimately connected to elevated latent heating over the Indian subcontinent. The latent heating profiles shown in Figure 4.29 highlight the enormous difference in atmospheric heating between consecutive pre- and post-monsoon periods. The value of the maximum heating increases between these two periods from values of approximately 2.7 Kday^{-1} in April-June (Period 3) to as high as 4 Kday^{-1} in June-July (Period 4). Not only do the values of maximum heating change, but also the duration of larger amounts of heating throughout the day. In Period 4, there is stronger latent heating during most

hours of the day with peak heating occurring between midnight and 4am and again between 2pm and 7pm. In Period 3, there is very little heating, with the exception of little amounts of stratiform latent heating, until about 2pm local time. In Period 4, both the convective and total latent heating increase at 2pm, but an additional maximum in heating, though not as strong, appears in the overnight hours between midnight and 4am. The stratiform latent heating in Period 4 is large for all hours of the day, and there is an evening peak similar to that in Period 3 in addition to a morning peak between midnight and 4am. The stratiform latent heating appears to contribute more to the total latent heating in Period 4 than it does in Period 3.

The plots of the diurnal fits and the actual averaged integrated heating in Figure 4.30 confirm the overall increase in heating from April-June to June-July. Integrated total latent heating averages to about 0.5 Kday^{-1} in Period 3 and about 1.3 Kday^{-1} in Period 4. The diurnal amplitude of the integrated total heating goes from a very strong 80% in Period 3 down to about 16%, a value more consistent with oceanic regions, in Period 4. The much stronger diurnal cycle in April-June compared to June-July agrees with the plots of latent heating evolution since there are multiple peaks in Period 4 that do not show up in Period 3. Larger amplitudes imply that a large percent of the total variation matches the first harmonic, which is a diurnal cycle with one peak during the 24 hours of the day.

Surprisingly, despite the large differences in the amplitude of the diurnal cycle, the phase differences between April-June and June-July in the Indian land region are very small, peaking at 7pm in Period 3 and at 8pm in Period 4. Figure 4.31 displays the diurnal amplitudes and phases for each of the eight 47-day periods averaged over the 13 years of data. The maximum diurnal amplitude is an impressive 96% in March and April, or Period 2. Not surprisingly, in Periods 4 and 5 the diurnal amplitudes are smallest and also closely match the semi-diurnal amplitudes, indicating that multiple daytime peaks in heating may contribute to the total heating variation. The phase in the Indian region varies between 2pm and 8pm during the annual cycle. The 2pm maximum in latent heating occurs in January through February, while the later 8pm maximum in heating occurs in Periods 3, 4, and 5 which correspond to April to September.

One interesting aspect of the Indian monsoon is the "elevated heating maximum" that occurs during the transition of the monsoon seasons. For example, (Choudhury and Krishnan, 2011) found that the level of maximum heating was progressively elevated as the percentage of stratiform fraction was increased. Figure 4.32 shows the difference between Period 3 and Period 4 in the height of maximum latent heating during all hours of the day and also shows the difference between the value of maximum latent heating through the depth of the atmosphere for each hour of the day. The height of maximum total and stratiform

latent heating rises from April-June to June-July when the overall rain rates and latent heating increases. The stratiform latent heating rises from roughly 7 km in Period 3 to 8 km in Period 4, and the total latent heating rises from roughly 6 km to 7 km. The height of maximum convective latent heating does not change much between Periods 3 and 4. The only difference in the height of maximum convective latent heating between the two periods is that there is a rise from 3 km to 5 km during the 6-7pm peak in Period 3 that is not present in Period 4. The hourly values of maximum latent heating throughout depth increase for stratiform, convective, and total latent heating from Period 3 to Period 4. It is evident based on the plots that there is an obvious maximum in latent heating between 2pm and 7pm in April-June, but a maximum in latent heating is more difficult to distinguish in June-July. This again agrees with the multiple peaks in Period 4 in the Indian region.

4.2.3 Comparing Land Regions

Consistent with prior studies, land regions tend to have a maximum in latent heating and rainfall in the afternoon and evening. Past research has found that over land, the "number of systems, conditional rainfall rates, and convective intensities of features without and with ice scattering respond strongly to afternoon heating" (Nesbitt and Zipser, 2003). Additionally, (Taylor, 2012) found that evening maxima of convective precipitation and deep convective

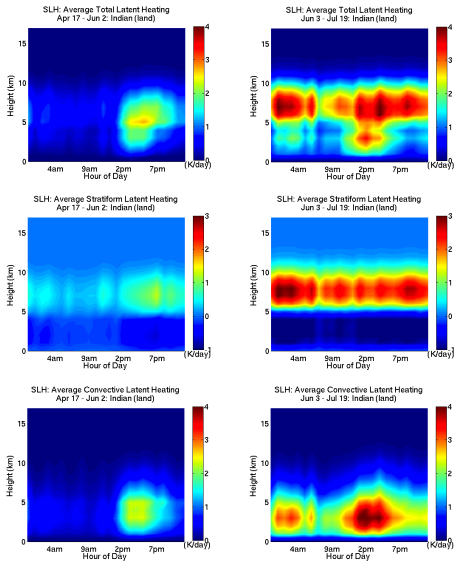

FIGURE 4.29: As in Figure 4.26 but for the Indian (land) region and for Period 3 *(left)* and Period 4 *(right)*.

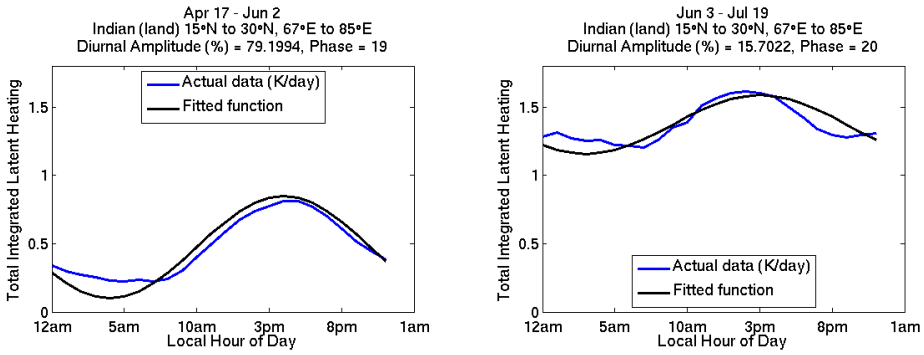

FIGURE 4.30: As in Figure 4.27 but for the Indian (land) region and for Period 3 *(left)* and Period 4 *(right)*.

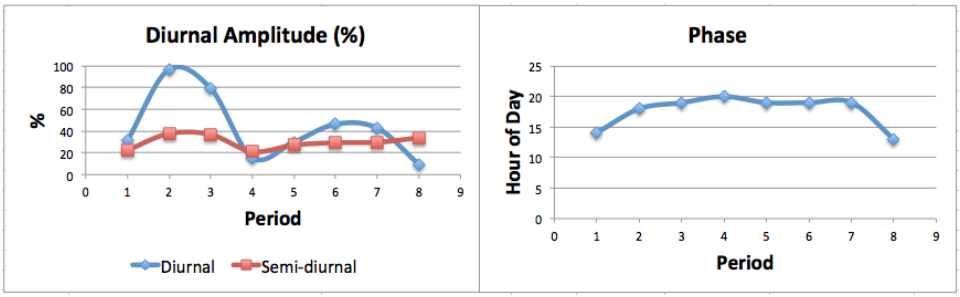

FIGURE 4.31: As in Figure 4.28 but for the Indian (land) region.

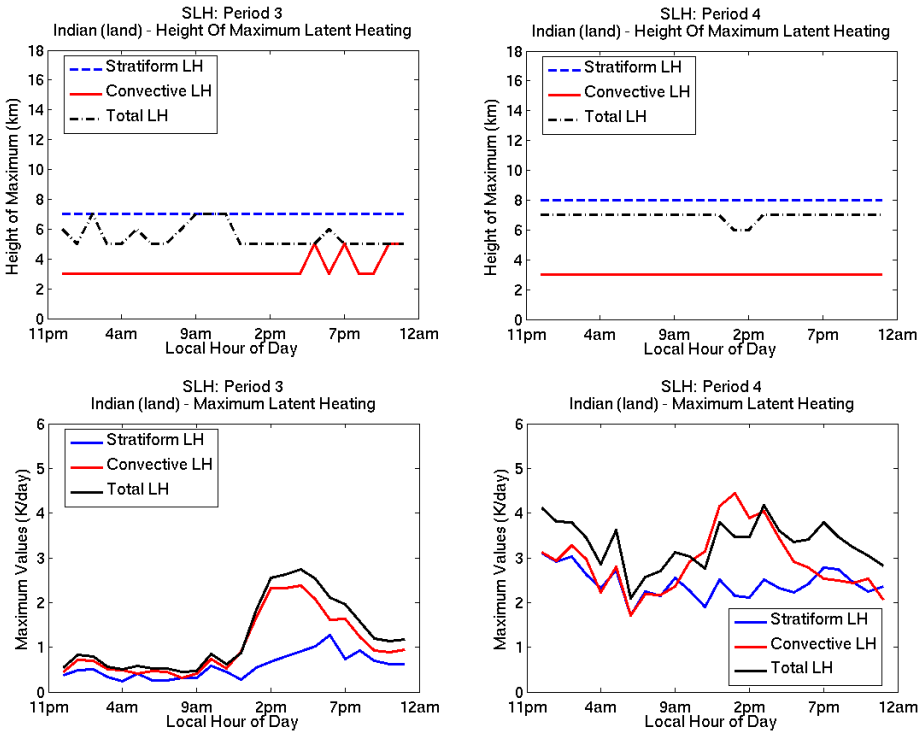

FIGURE 4.32: Indian monsoon – Diurnal cycle of height of maximum latent heating (stratiform, convective, and total) *(top)* and maximum values of latent heating (stratiform, convective, and total) through the depth of the atmosphere *(bottom)* for Period 3 *(left)* and Period 4 *(right)* averaged over 13-year period between 1998 and 2010.

clouds tend to occur in the evening over tropical land regions. This analysis reveals generally larger diurnal amplitudes over land than over ocean, implying stronger and more pronounced diurnal cycles over land. Based on Figure 4.33, the mean integrated total latent heating averaged over all hours of the day for each period for the Amazon and Congo regions largely follow a similar pattern of the strongest heating from October to April. The Indian region displays an annual pattern that is opposite to the Amazon and Congo regions, with the greatest heating occurring from June to September and the fewest amounts of heating occurring from October to April.

India contains a large range of mean latent heating between December-February (Periods 1 and 8) and June-September (Periods 4 and 5), much larger than the annual ranges in the Amazon and Congo regions. The values of integrated total heating in India are almost zero in Periods 1 and 8 before they rise dramatically to 1.4 $Kday^{-1}$ in Period 4. The dramatic increase in mean integrated total latent heating supports the onset of the monsoon. Figure 4.33 also demonstrates the annual cycle of the diurnal amplitudes for each of the three land regions in order to compare the diurnal cycle strength between regions. Again, the Indian region has a much larger difference in diurnal amplitudes throughout the year compared to the Amazon and Congo regions. India starts off in Period 1 with similar magnitude diurnal amplitudes that the Amazon and Congo have, but then in Periods 2 and 3 the strength of the diurnal cycles over India are almost double those in the Amazon and Congo. The Amazon and Congo have a similar pattern in the changes of diurnal amplitudes throughout the year, with very small changes in the strength of the diurnal cycle during the eight periods.

The differences in the ranges of the diurnal amplitudes between the three land regions is clearly related to the fact that the Indian region is forced by monsoon variability while the Amazon and Congo are forced by more gradual responses to seasonal solar heating variations. The phases in all three land regions are all very close to each other between 2pm and 9pm. The Amazon

and Congo have phases that are very close to each other during all periods, and India has similar phases to the two regions in all periods except for Periods 1 and 8. This deviation of the phases may be a result of the small integrated total latent heating values in December-February in the Indian region. These results are reinforced in Figure 4.34 where the seasonal cycle versus the diurnal cycle for the three land regions is depicted, highlighting afternoon and evening maxima in latent heating. Regrettably, it is not possible to verify the consistency of these results to equivalent estimates from the TRAIN algorithm due to the lack of sensitivity of passive microwave observations to precipitation over land.

4.3 Contrasting Ocean and Land

Because of the different ways that land and ocean respond to solar heating, there are inherent differences in the diurnal cycles of rainfall and latent heating between land and ocean regions. Figure 4.35 shows the annual cycles of the average integrated total latent heating for all ten regions based on the SLH dataset. The Indian Ocean region has the highest integrated heating value of all regions and all periods in June and July (Period 4) of about 1.8 Kday^{-1}. The lowest amounts of heating are found in the Atlantic during the subsidence period and in the Indian land region outside of the monsoon.

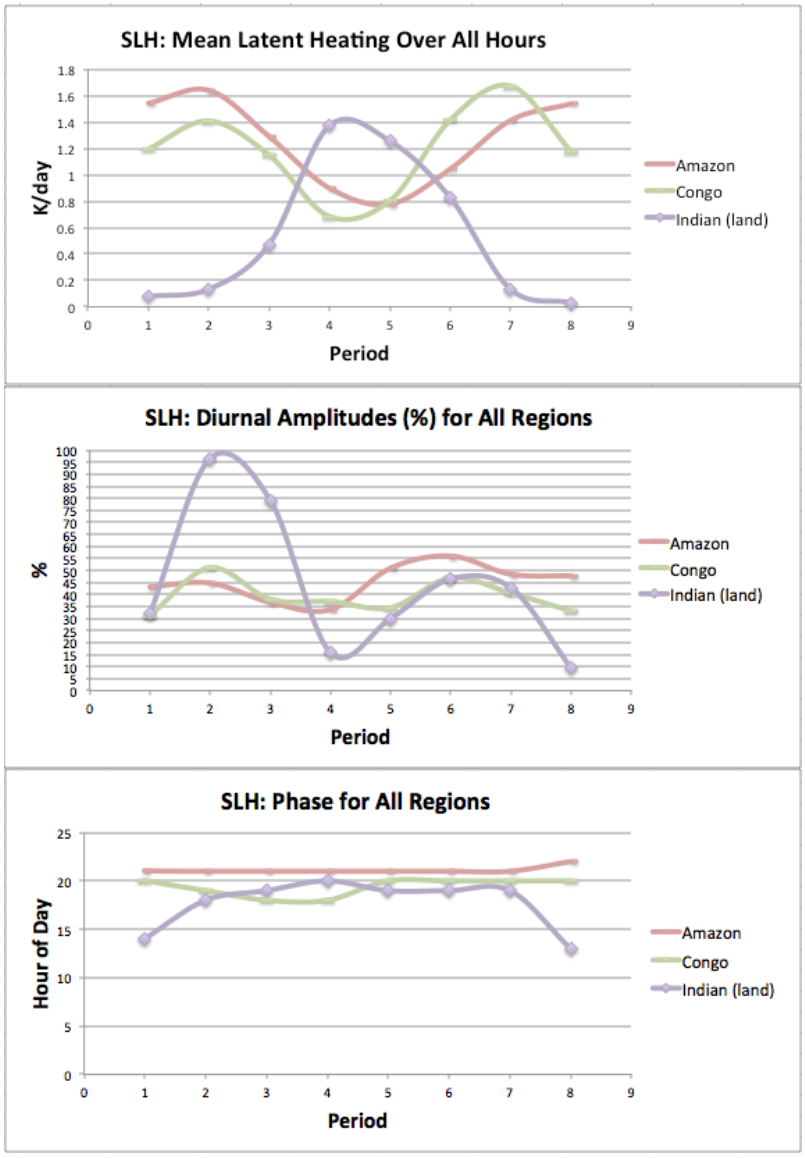

FIGURE 4.33: The annual cycle of average integrated total heating *(top)*, diurnal amplitude percentages *(middle)*, and phases *(bottom)* from SLH algorithm averaged over each land-boxed region and over all hours of day for each of the eight 47-day periods for 1998-2010.

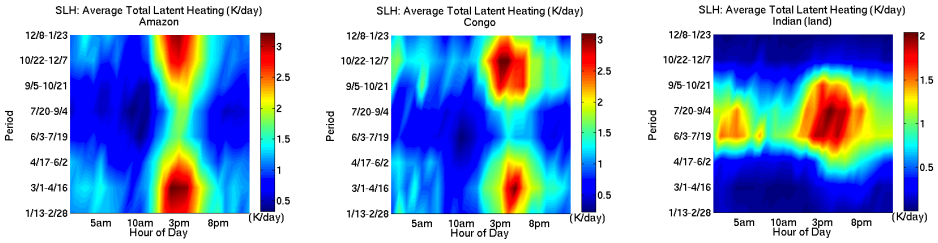

FIGURE 4.34: Plots of diurnal cycle and seasonal cycle of integrated total latent heating for all of the three land regions from the SLH algorithm with hour of day on the x-axis and seasonal cycle of eight 47-day periods on y-axis. Note: Color scales differ between regions. Regions include the Amazon, Congo, and Indian (land).

Figure 4.36 shows the calculated diurnal amplitudes and phases for all ten regions. Diurnal cycles range between 10% and 30% for all seven ocean regions throughout all times of year. The diurnal amplitudes for the Amazon and Congo regions range between 30% and 60% all year long and the diurnal amplitudes for the Indian land region range between 15% and 100%. Based on the figure, there is a clear distinction between the land and ocean areas in the magnitudes of the diurnal amplitudes, with larger diurnal amplitudes over land than over ocean. Results from a previous study confirm these differences between land and ocean since it was found that the "amplitudes of diurnal cycle of rainfall over continents is larger than that over open oceans" (Nesbitt and Zipser, 2003). There is an even more striking contrast between land and ocean regions in the plot of the annual cycle of the phases, with all ocean region phases falling between 5am and 10am local time during the eight periods. The diurnal cycles in the Amazon and Congo regions, however, exhibit peaks around 8pm local time. The peak of the diurnal cycle in the Indian region is around the same

time (8pm) in Periods 2-6, but deviates strongly in Periods 1 and 8 to an earlier phase of about 2pm.

The global map of diurnal amplitudes in Figure 4.37 for 5° x 5° grid boxes demonstrates that these higher amplitude percentages over land regions is a general feature and not particular to the regions examined here. The majority of the oceans have diurnal amplitude percentages between 0% and 50%, with a few isolated regions with higher amplitudes. Over northern South America and southern Africa and Australia, the diurnal variations are especially strong. There is weaker average integrated total heating over parts of South America, Africa and Australia based on the fact that those regions are masked out in Period 5 (explanation for masking can be found at the end of Section 2.7). Even though there is more masking over the Southern Hemisphere continents in Period 5, there are still higher amplitudes present over land compared to the oceans. Looking at the phases within the same figure, it is apparent that there is a difference in the time of local maximum integrated total latent heating between land and ocean grid boxes. In both January-February and July-September, the hours of local maxima over land are generally between noon and 7pm. Most of the ocean regions have times of local maximum integrated total heating in early morning hours between midnight and 10am. These global plots agree with the previous plots in Figure 4.33 of amplitudes and phases calculated from the SLH fits for all ten regions that are analyzed.

The differences in both seasonal and diurnal variations in integrated total latent heating between land and ocean from the SLH dataset are summarized in Figure 4.38. All of the ocean regions have the greatest integrated total heating in local summer when solar heating and available moisture are maximum. Past studies have found similar results of maximum rainfall and heating during the warm season. For example, one study found that the largest amplitudes in Northern Hemisphere generally occur during June, July, and August, while the largest amplitudes in the Southern Hemisphere generally occur during December, January, and February (Foster and Heidinger, 2013). The Maritime, Amazon, and Congo regions all have the largest integrated heating in SH summer, and all three regions reside either partly or entirely in the Southern Hemisphere. All ocean regions, even the Maritime Continent region, have maximum integrated heating in the early morning hours between midnight and 10am. Only the Indian Ocean has a clear secondary peak around 1pm local time in June and July (Period 4). Both the Amazon and Congo regions show a heating peak around 3-5pm from September to April. The Indian region has a heating peak around 3-7pm from June to September. There is also a weaker secondary peak in the morning hours around 4am from June to September in the Indian land region. The highest amounts of heating occur over the land regions with roughly 3 Kday^{-1} of average maximum heating. For the ocean regions, the largest heating rates occur in the Indian, Maritime, and Tropical West Pacific regions with an average maximum heating rate of about 2 Kday^{-1}. The smallest amounts of

heating are found in the East Pacific and in the Atlantic.

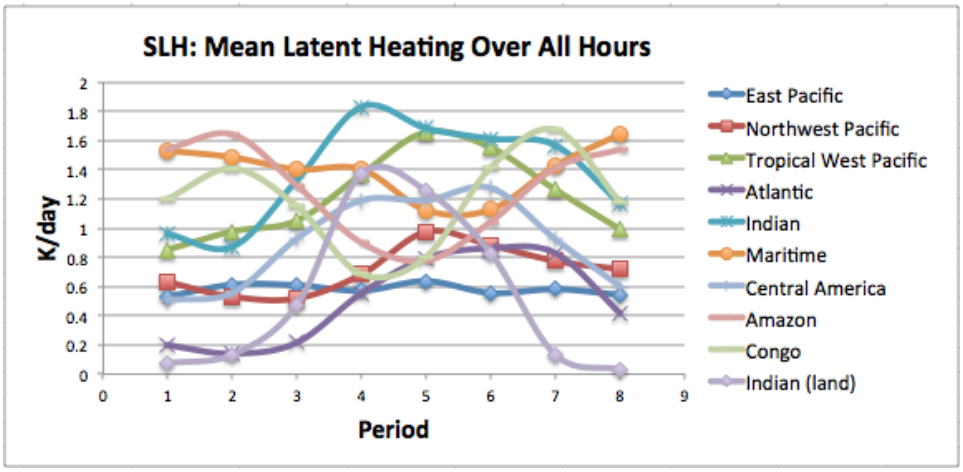

FIGURE 4.35: Global map of diurnal amplitude percentages and phases based on fits to 5° x 5° diurnal cycles of SLH integrated total latent heating for Period 1 *(left)* and Period 5 *(right)*. Includes masking of any grid boxes where average within the box is less than 2% of the maximum global amount of integrated total latent heating.

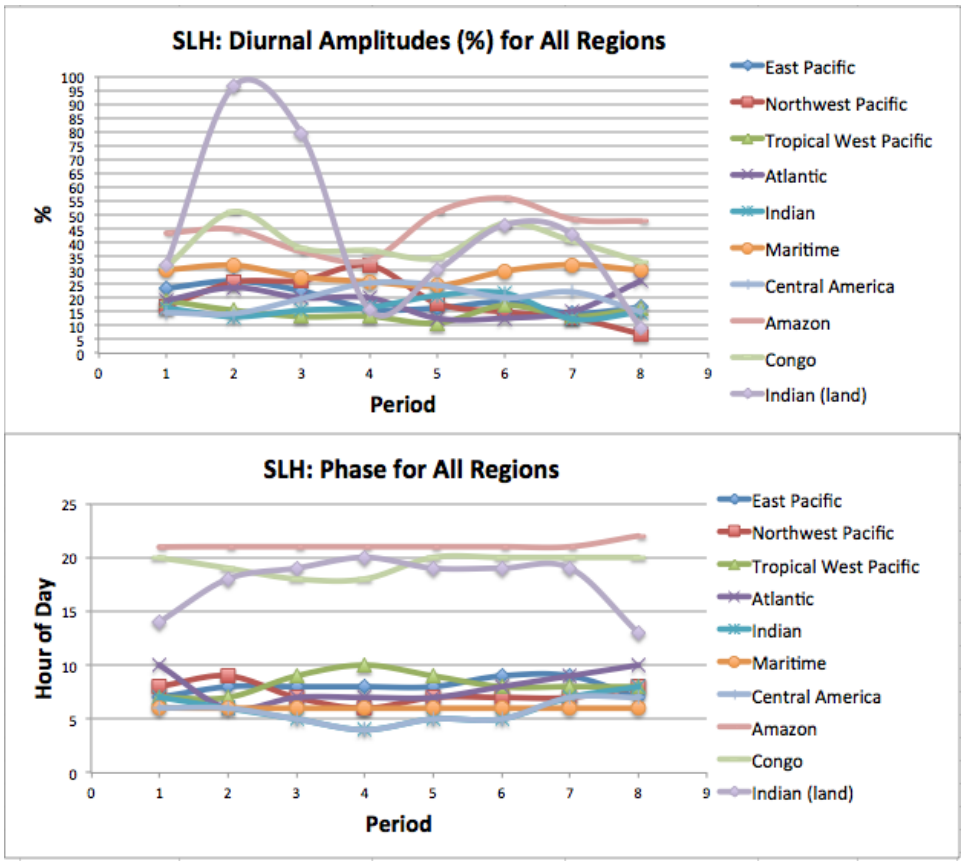

FIGURE 4.36: The diurnal amplitude percentages *(top)* and phases *(bottom)* for the integrated total heating for the seven ocean regions and three land regions calculated from the SLH algorithm.

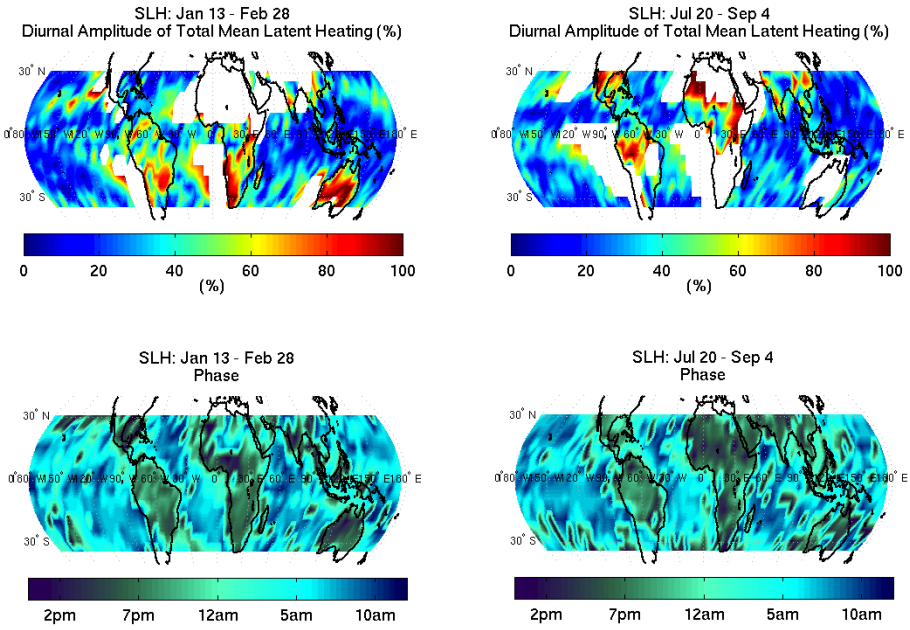

FIGURE 4.37: Global map of diurnal amplitude percentages *(top)* and phases *(bottom)* based on fits to 5° x 5° diurnal cycles of SLH integrated total latent heating for Period 1 *(left)* and Period 5 *(right)*. Includes masking of any grid boxes where average within the box is less than 2% of the maximum global amount of integrated total latent heating.

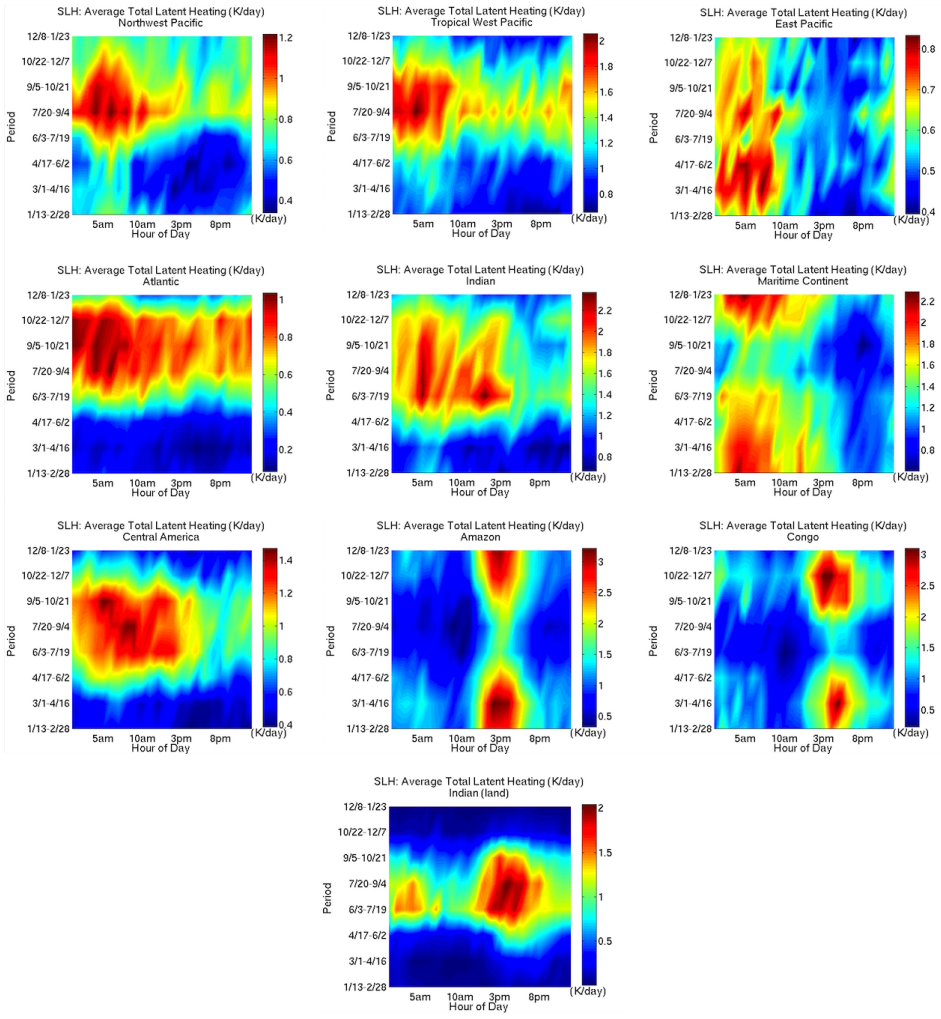

FIGURE 4.38: Plots of diurnal cycle and seasonal cycle of the integrated total latent heating for the seven ocean regions and three land regions from the SLH algorithm with hour of day on the x-axis and seasonal cycle of eight 47-day periods on y-axis. Note: Color scales differ between regions. *From left to right: (First row)* Northwest Pacific, Tropical West Pacific, East Pacific, *(Second row)* Atlantic, Indian, Maritime Continent, *(Third row)* Central America, Amazon, Congo, and *(Fourth row)* Indian (land).

Chapter 5

Summary and Conclusions

5.1 Interpretation of Results

Based on the regional results, there is clearly a diurnal cycle of rainfall and latent heating evident over both ocean and land regions based on TRMM observations. The diurnal cycles of latent heating differ between ocean regions, but each of the ocean regions has, on average, a maximum of integrated total latent heating in the early morning hours. The early morning peak seems especially prevalent over ocean regions close to the equator. The heating maximizes in July, August, and September in all the Northern Hemisphere ocean regions. The only region that departs from this trend is the Maritime Continent, the only region that resides mostly in the Southern Hemisphere, where

the heating maximizes in December to April. The highest rain rates and latent heating are found in the Maritime Continent, Tropical West Pacific, and Indian regions. The diurnal amplitudes of latent heating for ocean regions generally fall between 10% and 30%, and the phases over oceans generally fall between 5-10am according to both the TRAIN and SLH algorithms. There are signs of secondary peaks present over ocean regions based on our global phase maps, and these secondary peaks tend to occur when the diurnal and semi-diurnal amplitudes are similar in magnitude. In some cases the semi-diurnal amplitude actually exceeds the diurnal amplitudes – an instance of this occurs in the Atlantic in Period 2, the Indian Ocean region in Period 2, and in India in Periods 4 and 8.

Latent heating over land exhibits very different diurnal cycles than over the ocean. In general, land regions tend to have rainfall and latent heating maxima later in the day than in ocean regions based on the global phase maps. The heating maxima also generally tend to be in the warm season. The diurnal cycles are more pronounced over land regions based on higher diurnal amplitudes. Diurnal amplitudes range between 35% and 100% over land regions and the phases lie between 2pm and 10pm. The seasonal cycle of the strength of the diurnal cycle in India is quite different from the Amazon and Congo regions, with a very large variation throughout the year. In India, there is a different dominant mode of variability than there is in the Amazon and Congo, owing

to the strong influence of the monsoon. India also differs from the Amazon and Congo regions by having a secondary peak in the morning hours during the peak of the monsoon season, which causes the region to have a weaker diurnal cycle during that time of year. In Periods 1 and 8, India also contains earlier peaks in heating around 2pm.

While many of these findings apply to both the TRAIN and SLH algorithms, there are some interesting differences between the two datasets. First, the SLH algorithm tends to have a lower peak convective heating in the atmosphere than the TRAIN algorithm. The SLH algorithm often places peak convective heating between 2 km and 4 km, while the TRAIN algorithm has the peak of convective heating between 3 km and 5 km. The differences in the level of maximum convective heating between algorithms may stem from the use of shallow convection in SLH and not in TRAIN. There are also differences in the values of maximum convective and stratiform heating in both algorithms. In the TRAIN algorithm, there is a clear separation between convective and stratiform heating, with convective heating usually larger in magnitude than the stratiform heating. In the SLH algorithm, the maximum values of convective and stratiform heating are more comparable. For some hours of the day, the maximum values of stratiform latent heating actually exceed the maximum values of convective latent heating according to the SLH algorithm.

Differences also exist in the global distribution of integrated total heating

between the two algorithms. There are larger values of integrated heating in some locations, for example in the central and eastern Pacific, in the TRAIN algorithm compared to the SLH algorithm. Additionally, the TRAIN algorithm displays deeper total latent heating in the global cross-sections than the SLH algorithm does for both the Hadley and Walker Circulations. There are also differences in the Fourier fits, amplitudes, phases, and annual cycles of the amplitudes and phases between TRAIN and SLH. The diurnal amplitudes tend to be much larger in the SLH algorithm than the TRAIN algorithm for the same ocean regions. On the other hand, the phases generally agree well between the two heating algorithms. The largest differences in the annual patterns of the diurnal amplitudes and phases seem to be in the Northwest Pacific, Atlantic, and Indian Ocean regions. The differences between algorithms for these particular regions may be related to an increase in random synoptic systems affecting the diurnal cycles in higher-latitude regions such as the Northwest Pacific and Atlantic. This may especially be true in the winter season for these regions, which is when the phases deviate from the typical 5-10am peaks in the TRAIN algorithm for the Northwest Pacific and Atlantic. Nevertheless, there is sufficient agreement in the spatial distribution of heating and in the annual patterns of the diurnal cycle strength and local times of maxima to provide some confidence in the conclusions about heating variation in the regions examined.

5.2 Future research

While there is some disagreement between the two heating algorithms, there is also some agreement between them such as the phases and the spatial distributions of integrated heating. However, it is important to remember that the phases and amplitudes that are calculated are based on best fits to the actual data. Real data, however, is sporadic and random, and sometimes the fits may not actually represent the real data too well. When the fits to the data are not truly representative of the actual data, the conclusions drawn from the characteristic amplitudes and phases may be misguided. More research is needed to assess the accuracy of these results using additional heating algorithms. It seems based on this research that most ocean regions share similar times of peak integrated total latent heating, but the strength of the diurnal cycle varies between different ocean regions and during different seasons.

Some additional analysis that could be done includes adding the radiative heating to the examination of diabatic heating profiles in the tropics. The radiative heating portion of diabatic heating is important since "a clear relationship emerges between the vertical structure of atmospheric radiative heating and large-scale vertical motion through its impact on the regional distribution of clouds and water vapor" (L'Ecuyer and McGarragh, 2010). Furthermore, a "key to the interaction of convection with large-scale circulation is the diabatic

heating associated with condensation, evaporation, and radiative transport processes and its vertical and horizontal distribution throughout the tropics" (Jakob and Schumacher, 2008). Future work could also include assessing the relationships between heating, clouds, and other environmental factors such as vertical motion since horizontal wind divergence and vertical motion are directly related to diabatic heating (Tao and coauthors, 2006). Studying the relationship between heating and cloud cover could be done through calculations of cloud fractions using data from the TRAIN dataset since number of high, low, and raining clouds are available to analyze. Additional environmental factors that could also influence atmospheric heating profiles include SST, SST gradients, wind divergence and convergence at the surface, and dry or moist air columns (Su et al., 2008). Furthermore, it would be beneficial to compare these results against reanalyses and climate models to test the accuracies of the numerical model simulations of tropical rainfall and heating.

Further investigation could also be focused on the physical processes behind the diurnal cycle variations since, for instance, the causes for the observed diurnal cycles of precipitation over ocean regions remain uncertain (Nesbitt and Zipser, 2003). Differences between land and ocean regions in the diurnal cycles of latent heating and rainfall may be explained by local effects such as mountainous terrain, coasts, surface fluxes, land/sea differences, surface emissivities, and SST changes. However, both local and large-scale forcings may influence

the diurnal cycles in certain regions, and no one mechanism is necessarily exclusive in acting to control the diurnal cycle (Nesbitt and Zipser, 2003). It may also be interesting to further analyze the diurnal cycles within regions of annual heavy rainfall versus the diurnal cycles within predominantly shallow stratocumulus regions. Examining the diurnal and seasonal cycles within smaller boxed regions than the boxed regions chosen for this study may be useful in providing further insight into the environmental factors that govern changes in precipitation.

Perhaps the best way to improve model representation of rainfall and heating is to combine what is known and understood on regional scales. Examining heating and precipitation on regional scales may help to provide insight on the atmospheric parameters that influence the diurnal and seasonal variations. It may be beneficial for scientists to continue studying satellite products and heating algorithms and to experiment with the capability of modeling future rainfall based on representation of microphysical processes. With the future demise of the TRMM satellite, a new era of satellite data is already beginning with the Global Precipitation Mission (GPM) satellite that was launched on February 28, 2014. The GPM satellite offers a global view of precipitation and is more sensitive to lighter precipitation (<0.5 mm/hour), which TRMM has difficulties detecting. The GPM satellite will also be able to measure snowfall, which

should provide a more complete look at Earth's water cycle. Continued advancements in space-borne and ground instruments and in the algorithms that require the observations to estimate rainfall and diabatic heating will help with future forecasting capabilities on global and regional scales.

Appendix A

Tropical West Pacific

The following plots are all for the Tropical West Pacific boxed region and include 1) Winter and summer diurnal cycle of integrated total latent heating, 2) Winter and summer fourier fits to the diurnal cycle of total integrated latent heating, 3) Seasonal variation of diurnal amplitudes and phases, 4) Winter and summer diurnal cycle of height of maximum latent heating, 5) Winter and summer diurnal cycle of maximum value of latent heating in atmospheric column, and 6) Diurnal and seasonal cycle of integrated total latent heating.

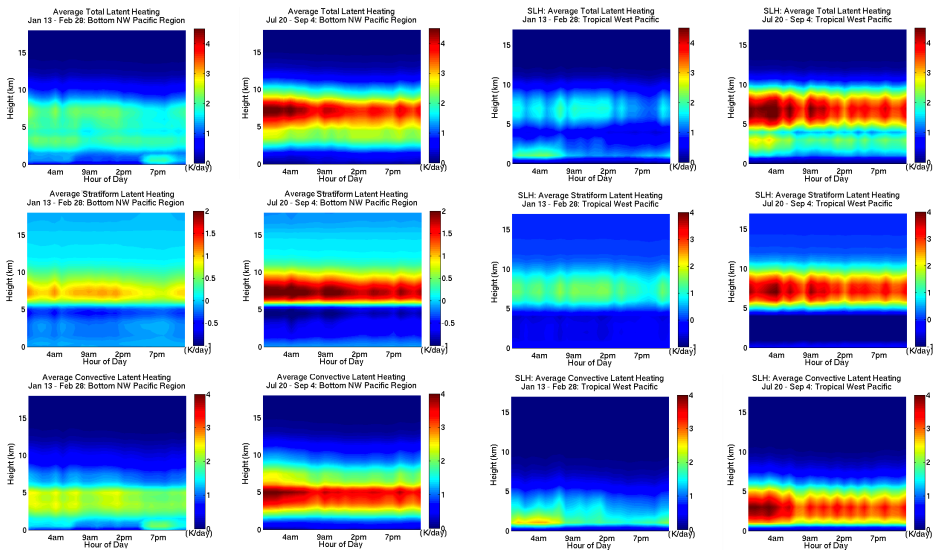

FIGURE A.1: Tropical West Pacific – 13-year composite of average total *(top)*, stratiform *(middle)*, and convective *(bottom)* vertical latent heating structures in Period 1 and Period 5 for the TRAIN algorithm *(left)* and the SLH algorithm *(right)*. Units are in Kelvin per day.

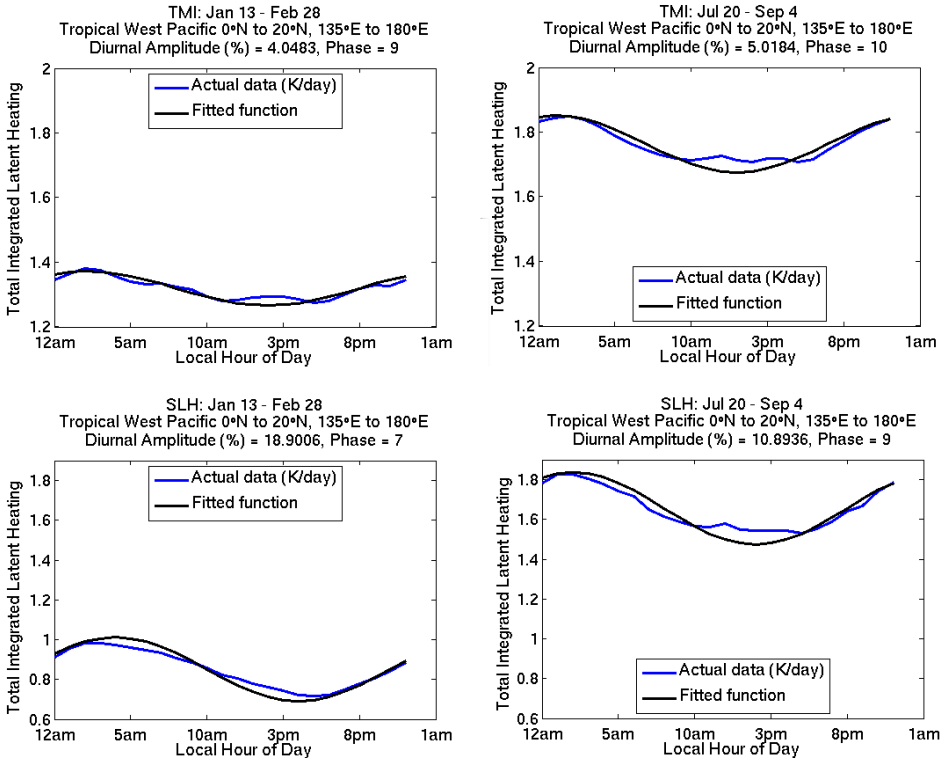

FIGURE A.2: Fourier fit to the diurnal cycle of the TRAIN integrated heating *(top)* and SLH integrated heating *(bottom)* in the Tropical West Pacific boxed region for Period 1 *(left)* and Period 5 *(right)*. Actual data is the blue line and the Fourier fit is the black line. Actual data was smoothed in these plots in order to compare to the fit. Included in the title are the latitude and longitude coordinates, the diurnal amplitude percentage, and the phase.

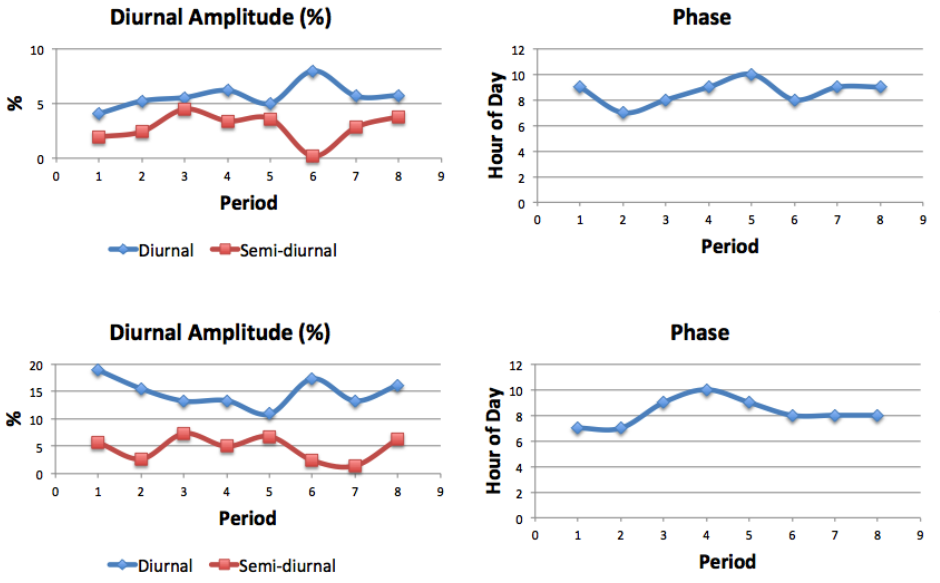

FIGURE A.3: Tropical West Pacific – Diurnal amplitude percentages and semi-diurnal amplitude percentages *(left)* and phases *(right)* in military time of TRAIN integrated total latent heating *(top)* and SLH integrated total heating *(bottom)* for each of the eight 47-day periods averaged over 13-year period between 1998 and 2010.

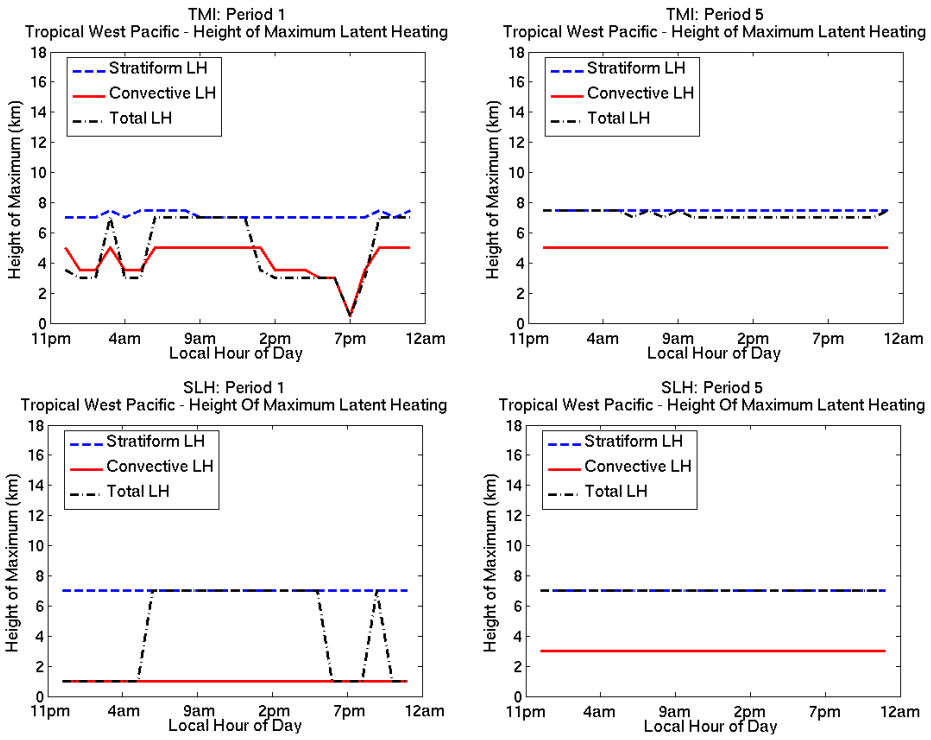

FIGURE A.4: Tropical West Pacific – Diurnal cycle of height of maximum latent heating (stratiform, convective, and total) for Period 1 *(left)* and Period 5 *(right)* from the TRAIN algorithm *(top)* and the SLH algorithm *(bottom)* averaged over 13-year period between 1998 and 2010.

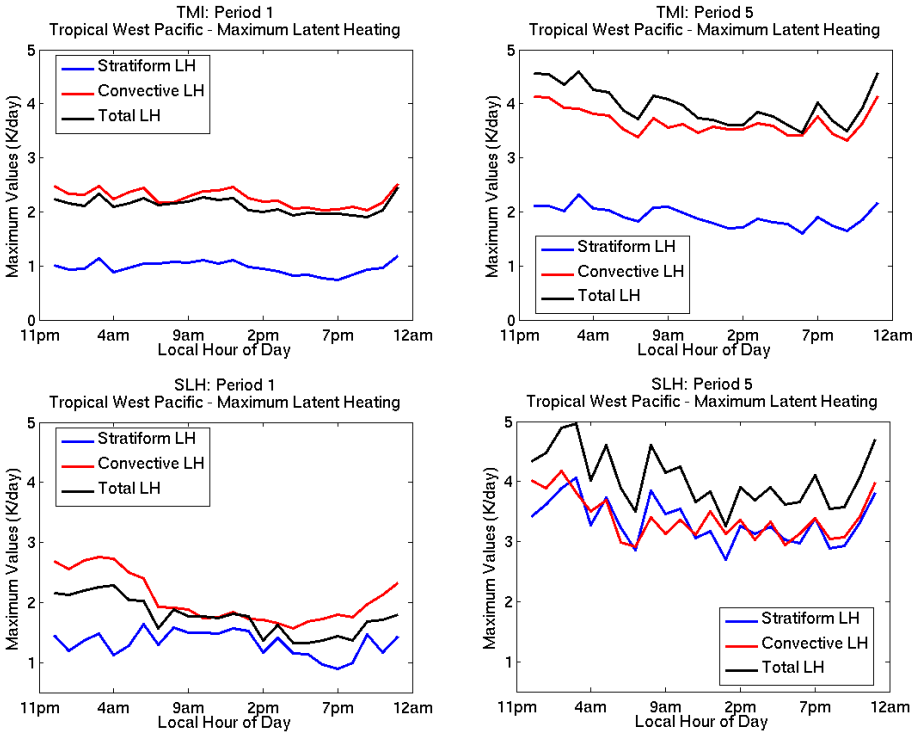

FIGURE A.5: Tropical West Pacific – Diurnal cycle of maximum values of latent heating (stratiform, convective, and total) through the depth of the atmosphere for Period 1 *(left)* and Period 5 *(right)* from the TRAIN algorithm *(top)* and the SLH algorithm *(bottom)* averaged over 13-year period between 1998 and 2010.

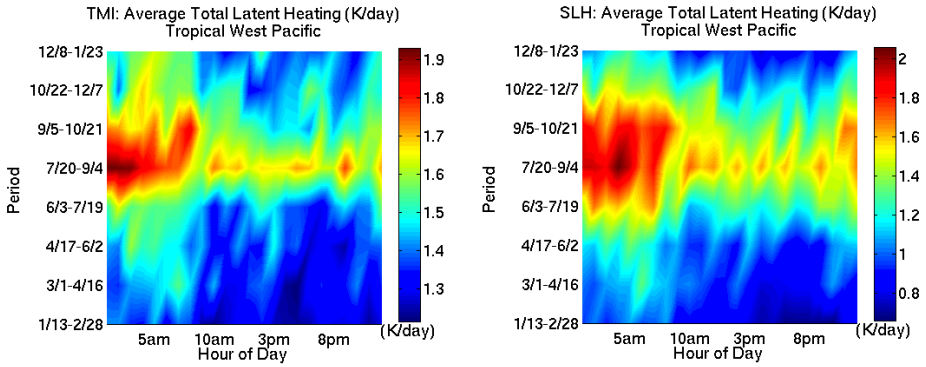

FIGURE A.6: Plots of diurnal cycle and seasonal cycle of integrated total latent heating for the Tropical West Pacific region from the TRAIN algorithm *left* and the SLH algorithm *right* with hour of day on the x-axis and seasonal cycle of eight 47-day periods on y-axis.

Appendix B

Maritime Continent

The following plots are all for the Maritime Continent boxed region and include 1) Winter and summer diurnal cycle of integrated total latent heating, 2) Winter and summer fourier fits to the diurnal cycle of total integrated latent heating, 3) Seasonal variation of diurnal amplitudes and phases, 4) Winter and summer diurnal cycle of height of maximum latent heating, 5) Winter and summer diurnal cycle of maximum value of latent heating in atmospheric column, and 6) Diurnal and seasonal cycle of integrated total latent heating.

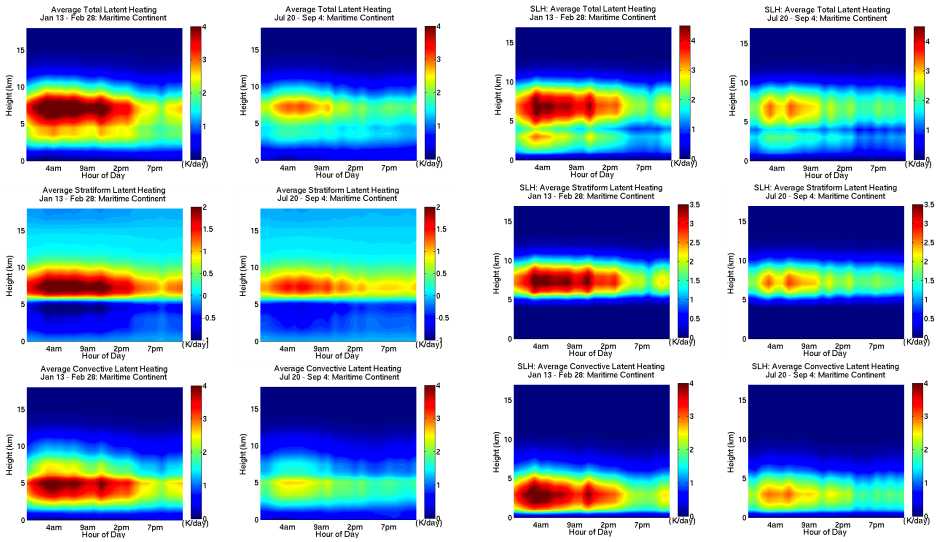

FIGURE B.1: As in Figure A.1 but for the Maritime Continent region.

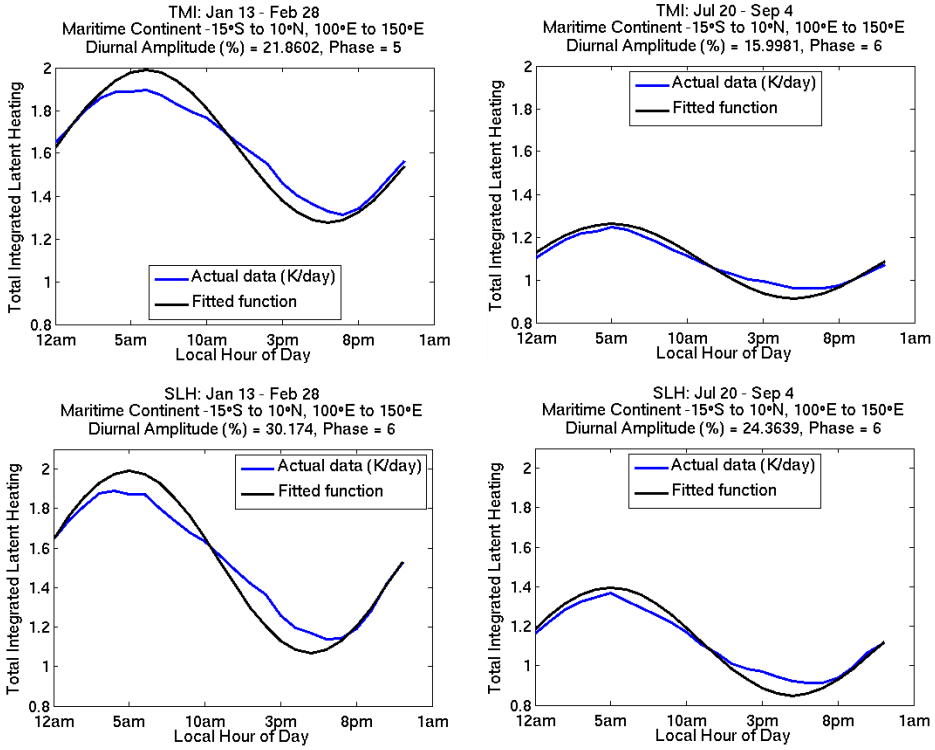

FIGURE B.2: As in Figure A.2 but for the Maritime Continent region.

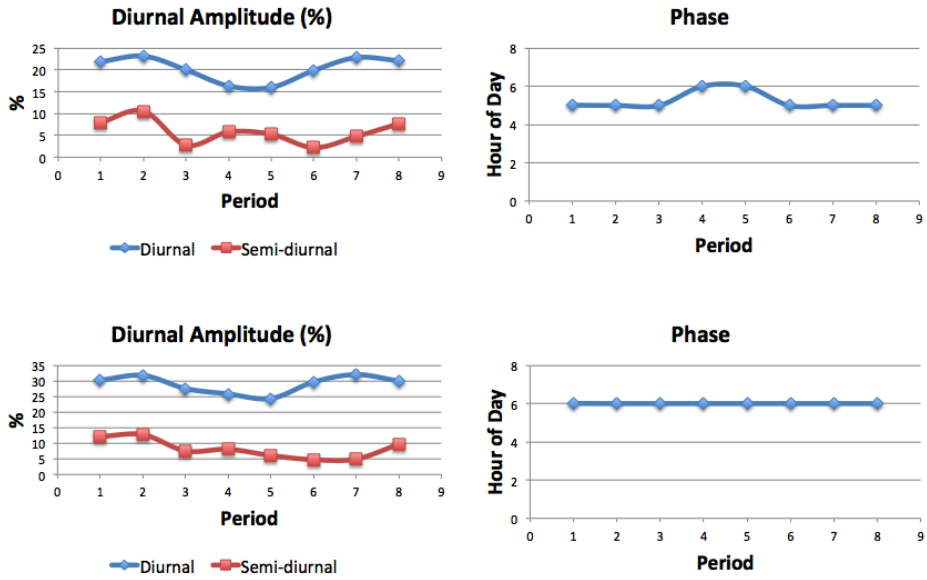

FIGURE B.3: As in Figure A.3 but for the Maritime Continent region.

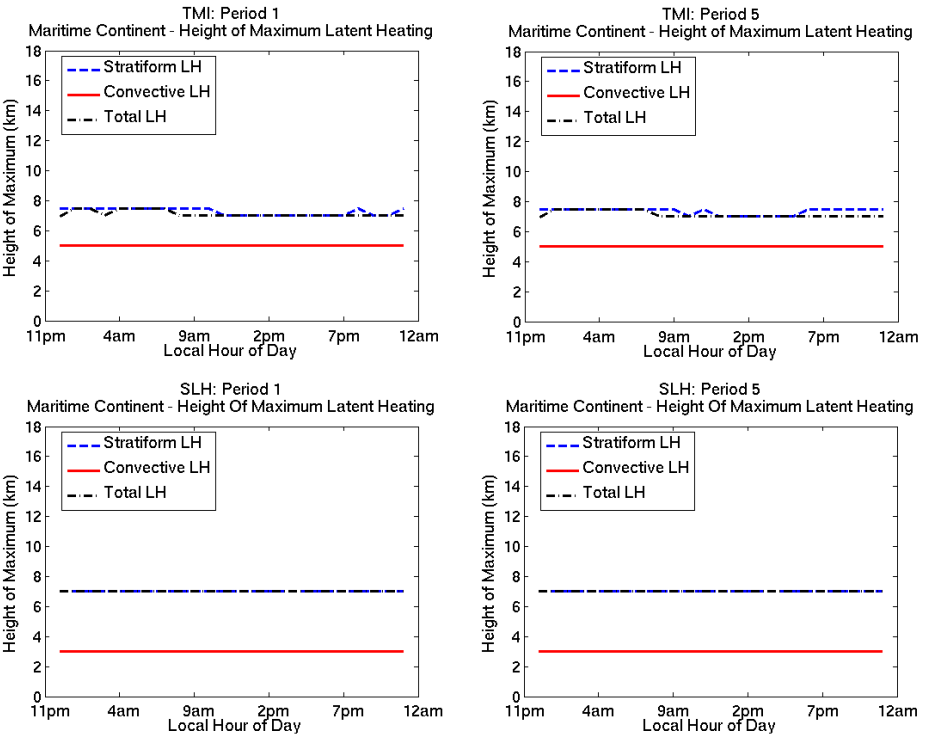

FIGURE B.4: As in Figure A.4 but for the Maritime Continent region.

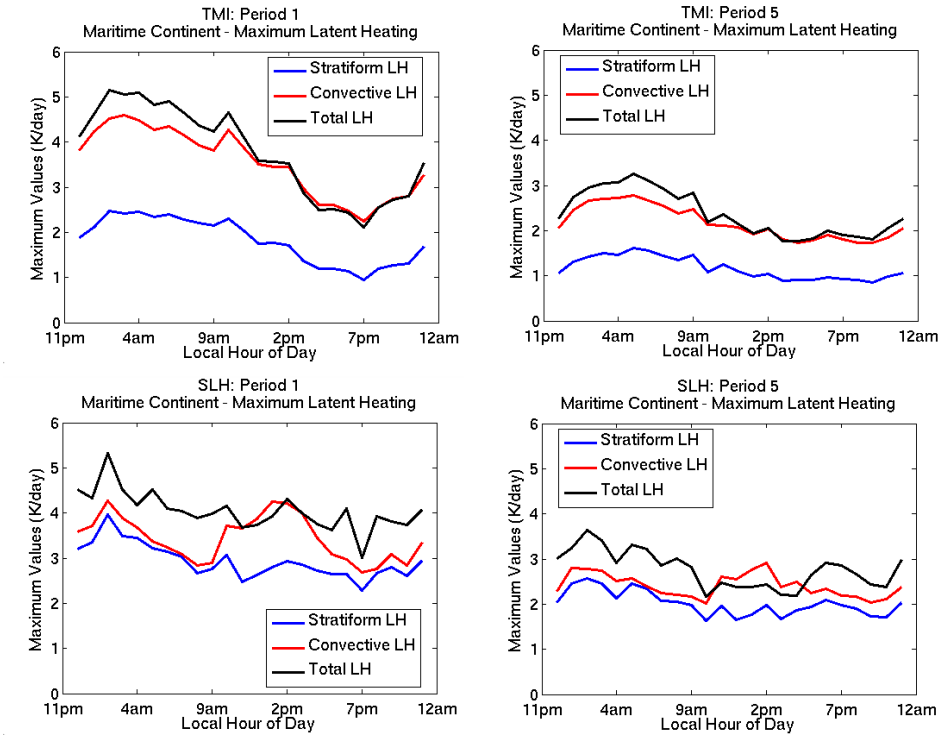

FIGURE B.5: As in Figure A.5 but for the Maritime Continent region.

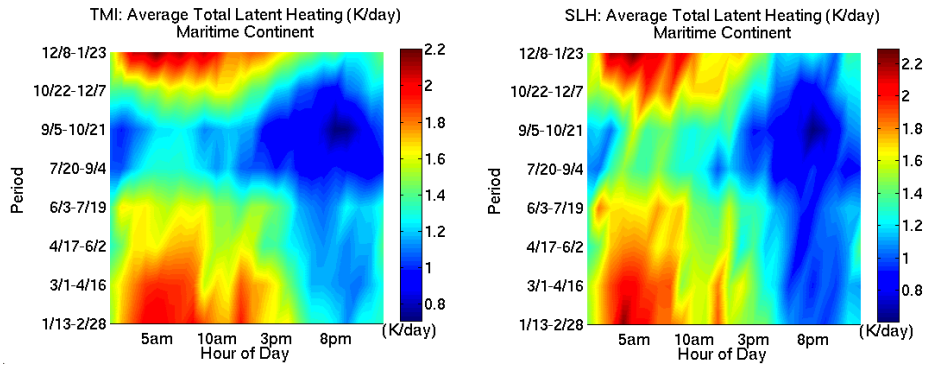

FIGURE B.6: As in Figure A.6 but for the Maritime Continent region.

Appendix C

East Pacific

The following plots are all for the East Pacific boxed region and include 1) Winter and summer diurnal cycle of integrated total latent heating, 2) Winter and summer fourier fits to the diurnal cycle of total integrated latent heating, 3) Seasonal variation of diurnal amplitudes and phases, 4) Winter and summer diurnal cycle of height of maximum latent heating, 5) Winter and summer diurnal cycle of maximum value of latent heating in atmospheric column, and 6) Diurnal and seasonal cycle of integrated total latent heating.

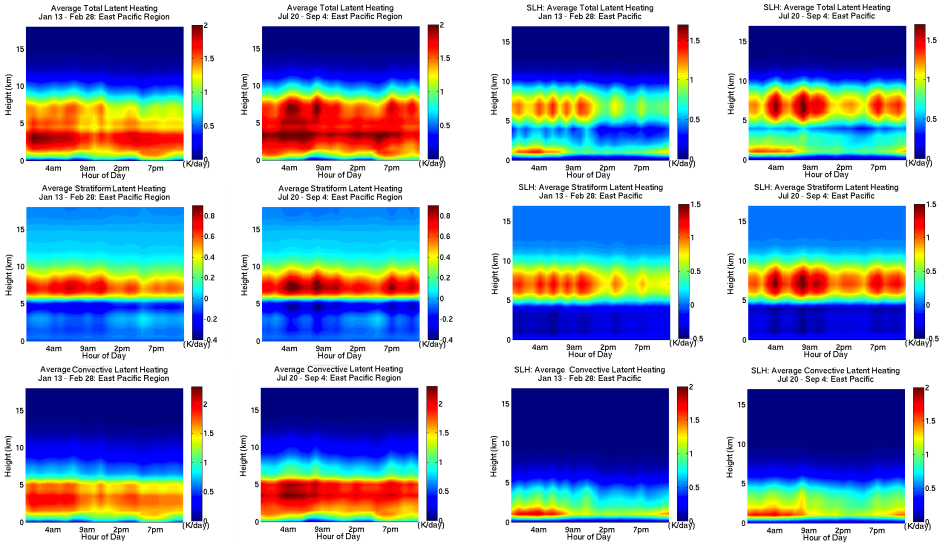

FIGURE C.1: As in Figure A.1 but for the East Pacific region.

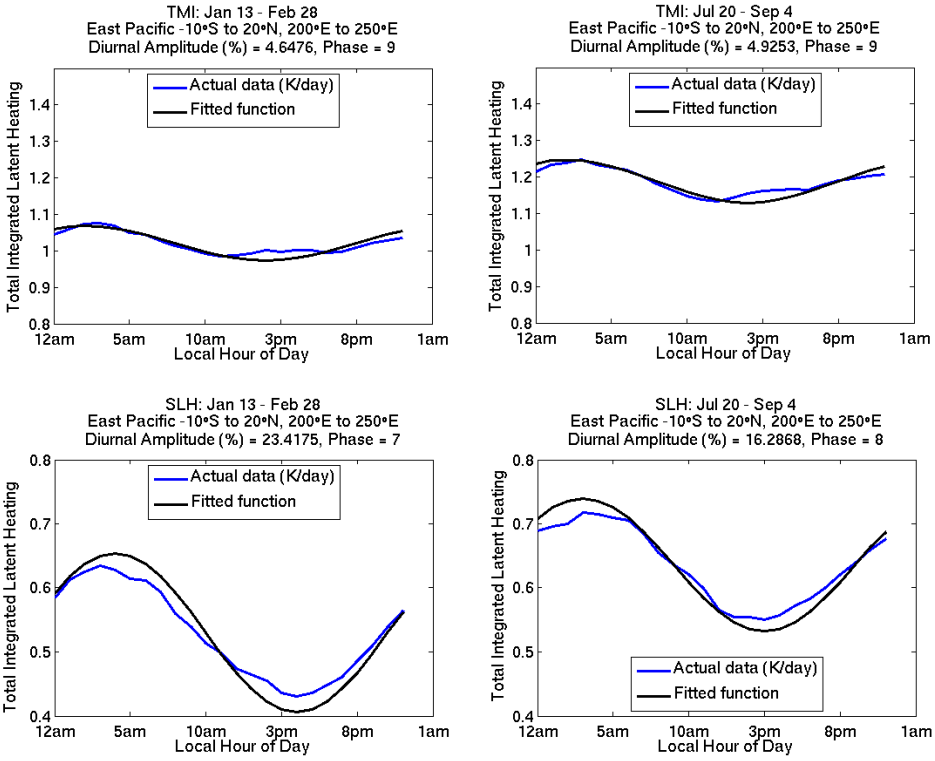

FIGURE C.2: As in Figure A.2 but for the East Pacific region.

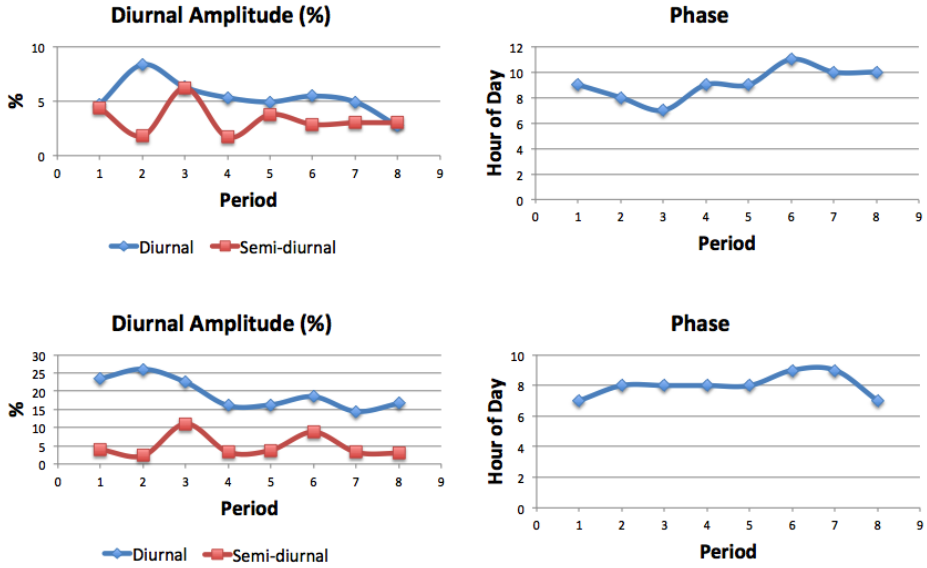

FIGURE C.3: As in Figure A.3 but for the East Pacific region.

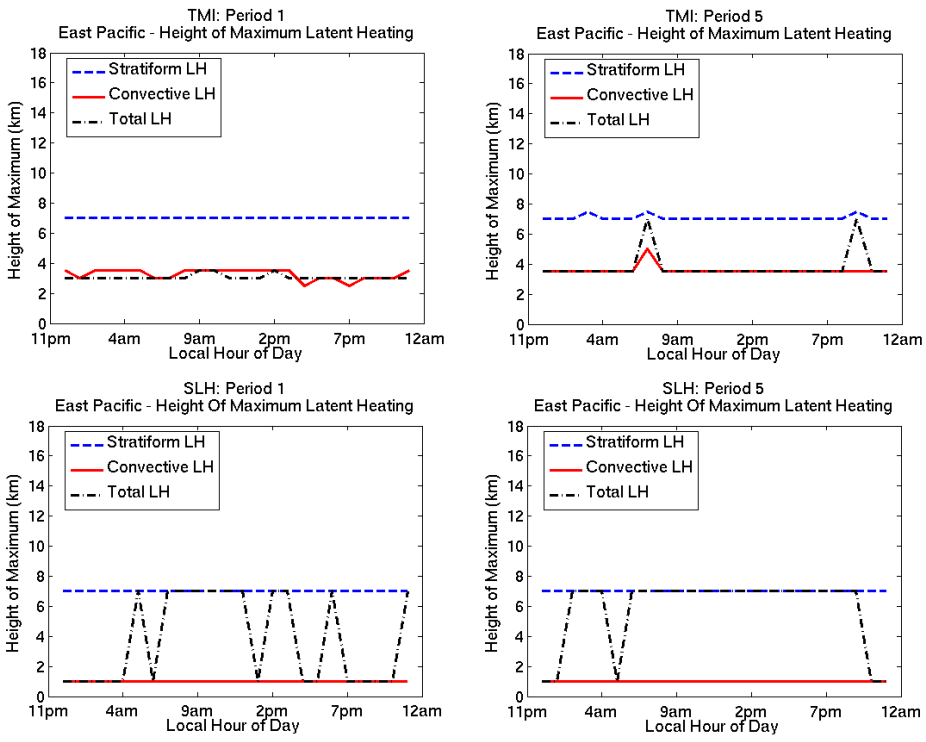

FIGURE C.4: As in Figure A.4 but for the East Pacific region.

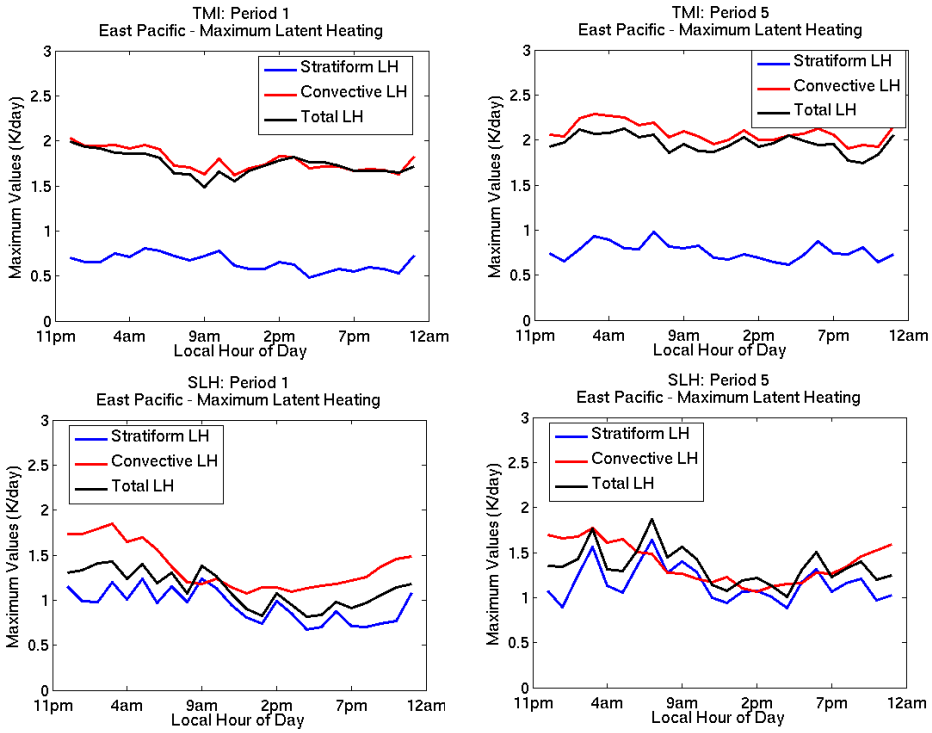

FIGURE C.5: As in Figure A.5 but for the East Pacific region.

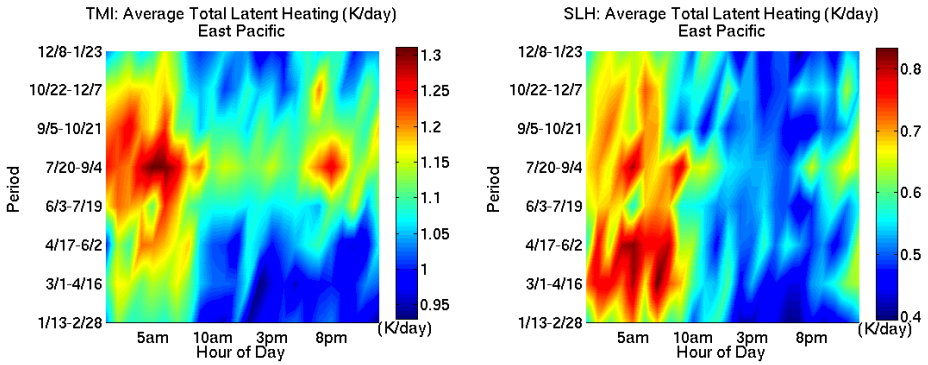

FIGURE C.6: As in Figure A.6 but for the East Pacific region.

Appendix D

Atlantic

The following plots are all for the Atlantic boxed region and include 1) Winter and summer diurnal cycle of integrated total latent heating, 2) Winter and summer fourier fits to the diurnal cycle of total integrated latent heating, 3) Seasonal variation of diurnal amplitudes and phases, 4) Winter and summer diurnal cycle of height of maximum latent heating, 5) Winter and summer diurnal cycle of maximum value of latent heating in atmospheric column, and 6) Diurnal and seasonal cycle of integrated total latent heating.

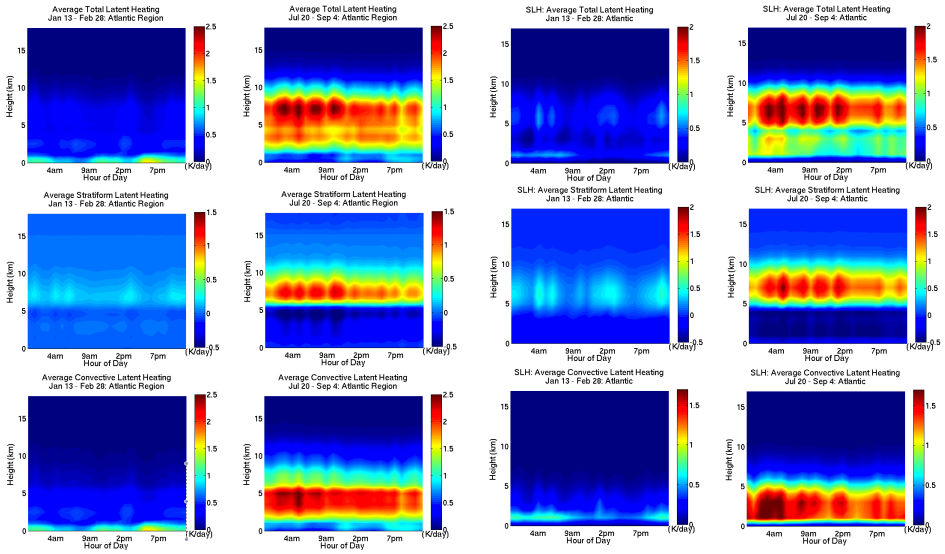

FIGURE D.1: As in Figure A.1 but for the Atlantic region.

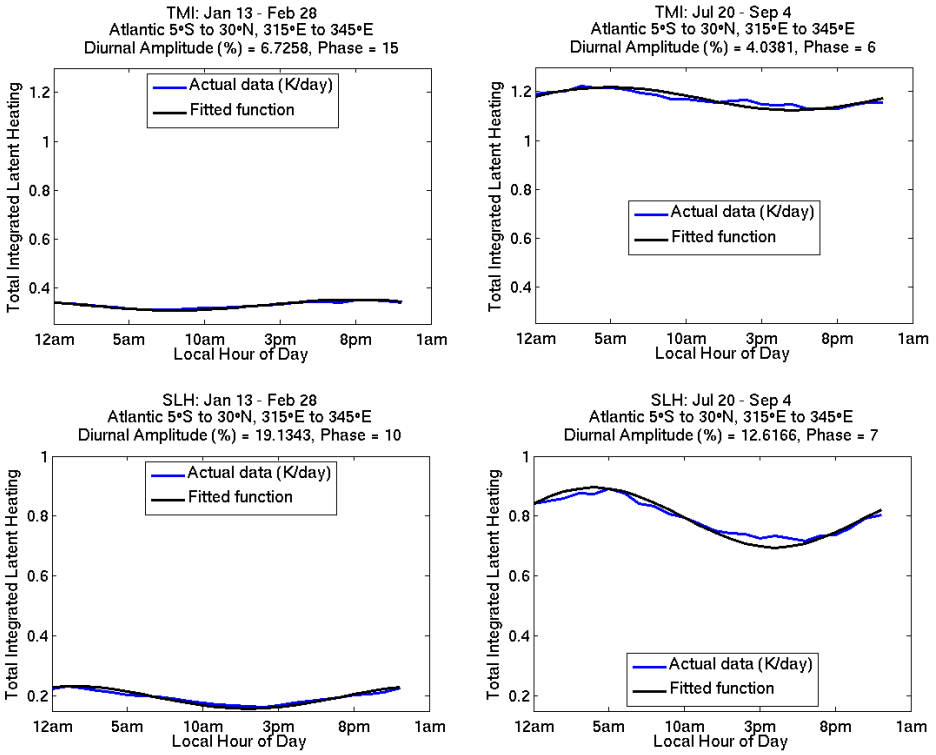

FIGURE D.2: As in Figure A.2 but for the Atlantic region.

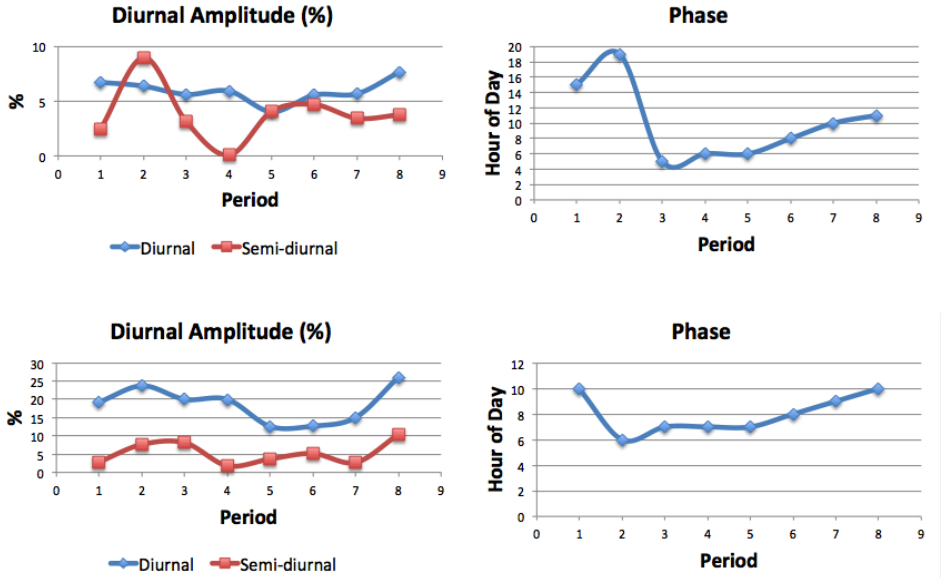

FIGURE D.3: As in Figure A.3 but for the Atlantic region.

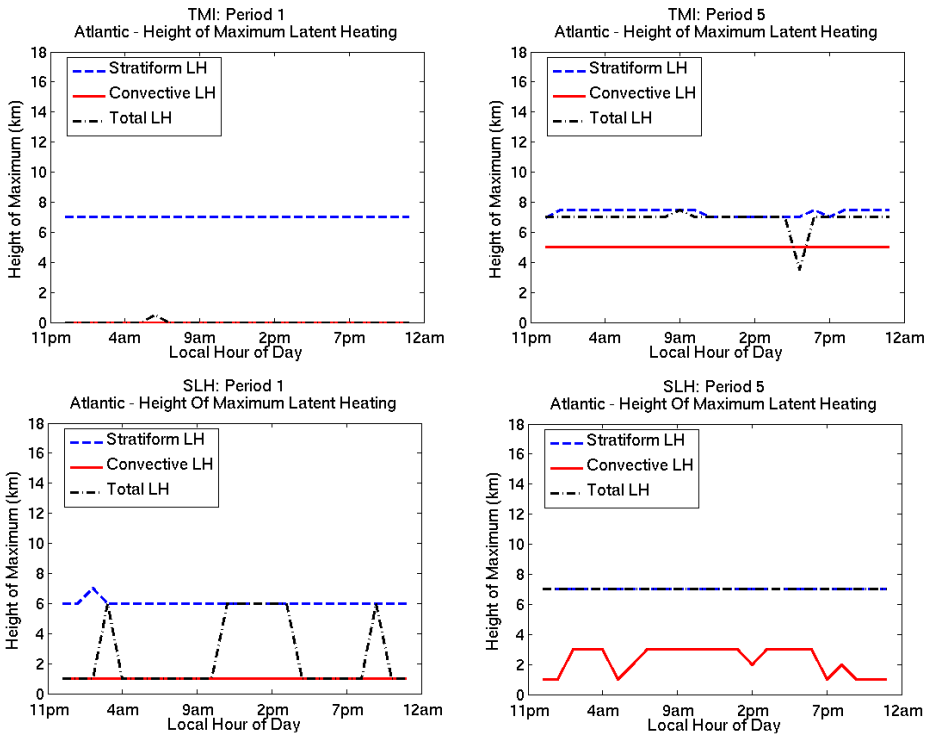

FIGURE D.4: As in Figure A.4 but for the Atlantic region.

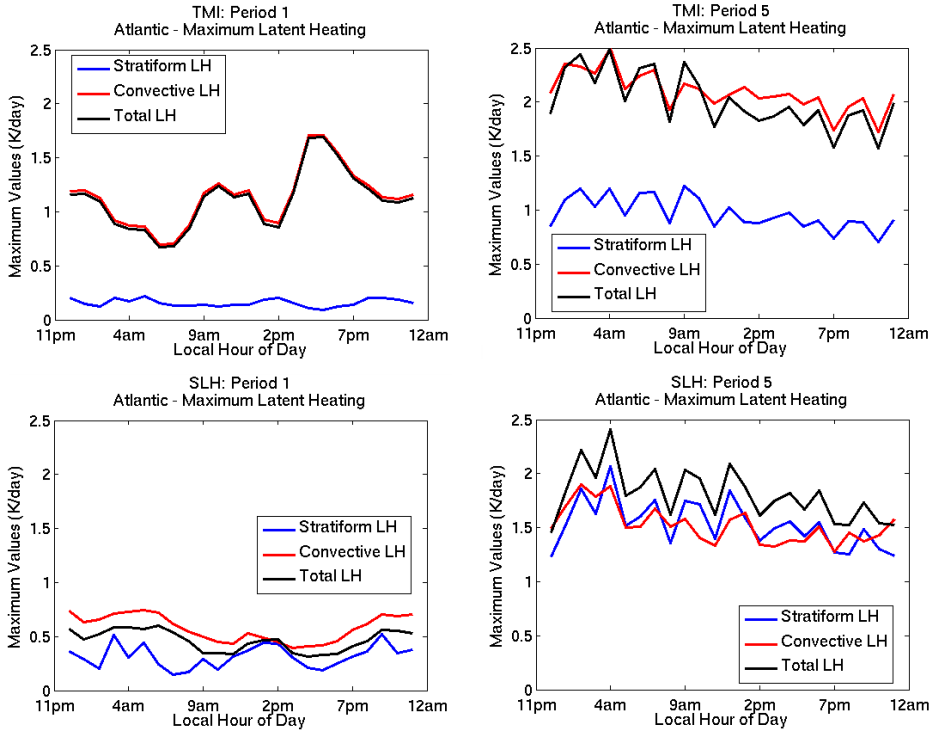

FIGURE D.5: As in Figure A.5 but for the Atlantic region.

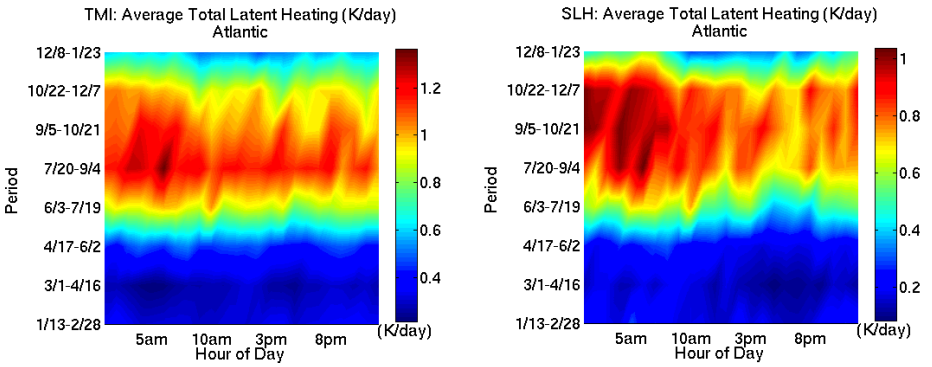

FIGURE D.6: As in Figure A.6 but for the Atlantic region.

Appendix E

Northwest Pacific

The following plots are all for the Northwest Pacific boxed region and include 1) Winter and summer diurnal cycle of integrated total latent heating, 2) Winter and summer fourier fits to the diurnal cycle of total integrated latent heating, 3) Seasonal variation of diurnal amplitudes and phases, 4) Winter and summer diurnal cycle of height of maximum latent heating, 5) Winter and summer diurnal cycle of maximum value of latent heating in atmospheric column, and 6) Diurnal and seasonal cycle of integrated total latent heating.

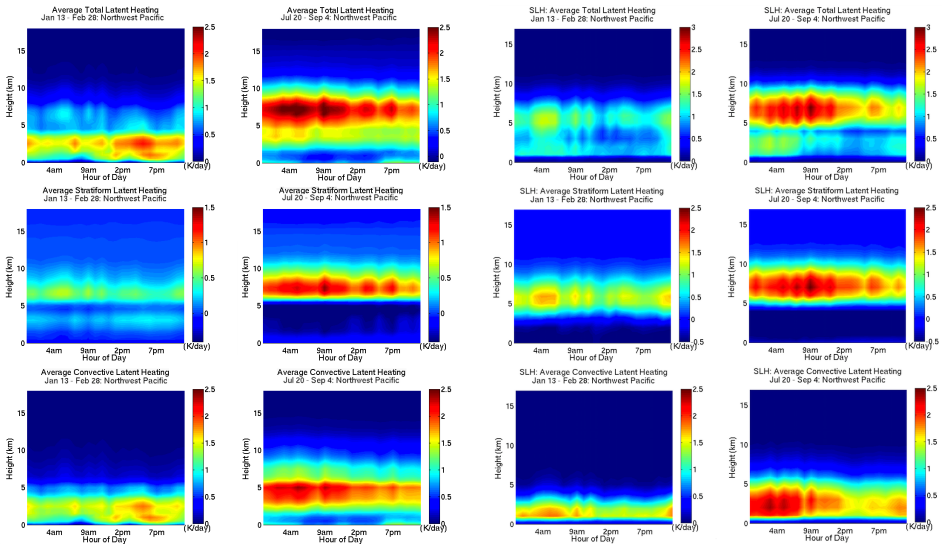

FIGURE E.1: As in Figure A.1 but for the Northwest Pacific region.

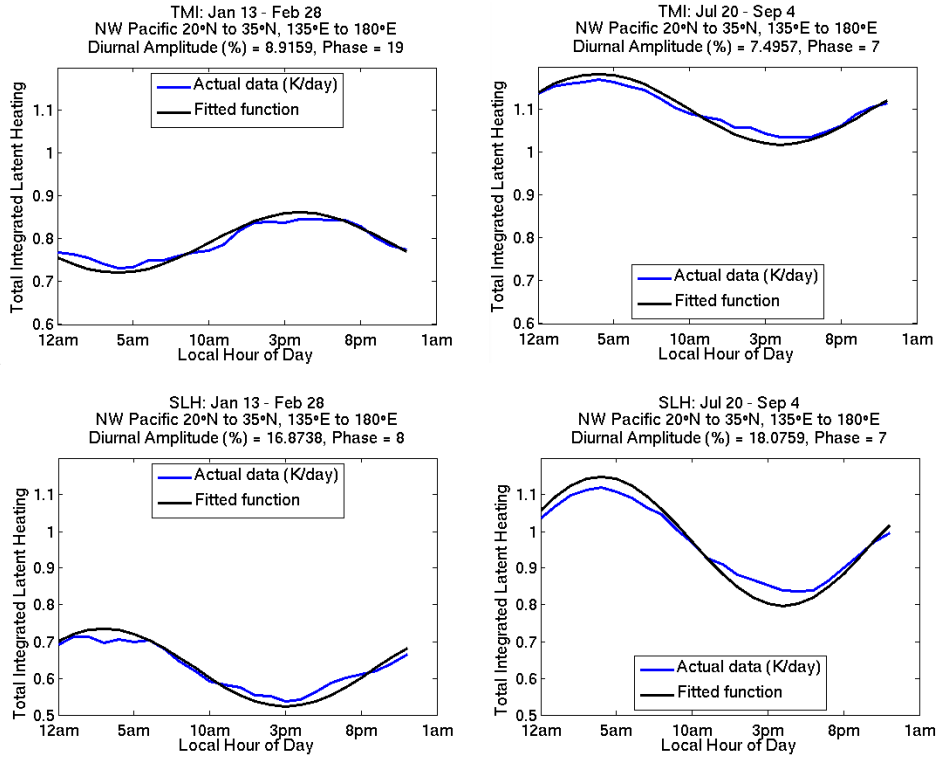

FIGURE E.2: As in Figure A.2 but for the Northwest Pacific region.

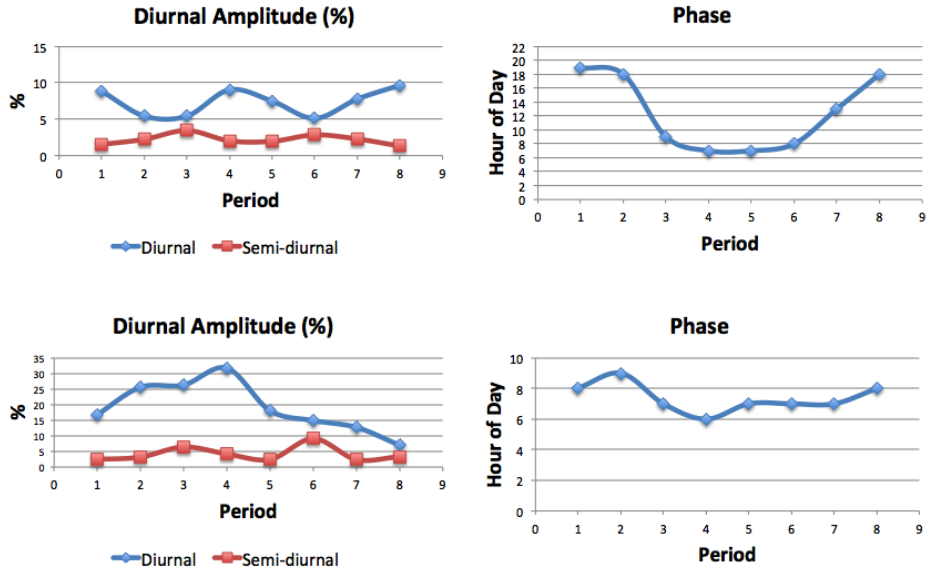

FIGURE E.3: As in Figure A.3 but for the Northwest Pacific region.

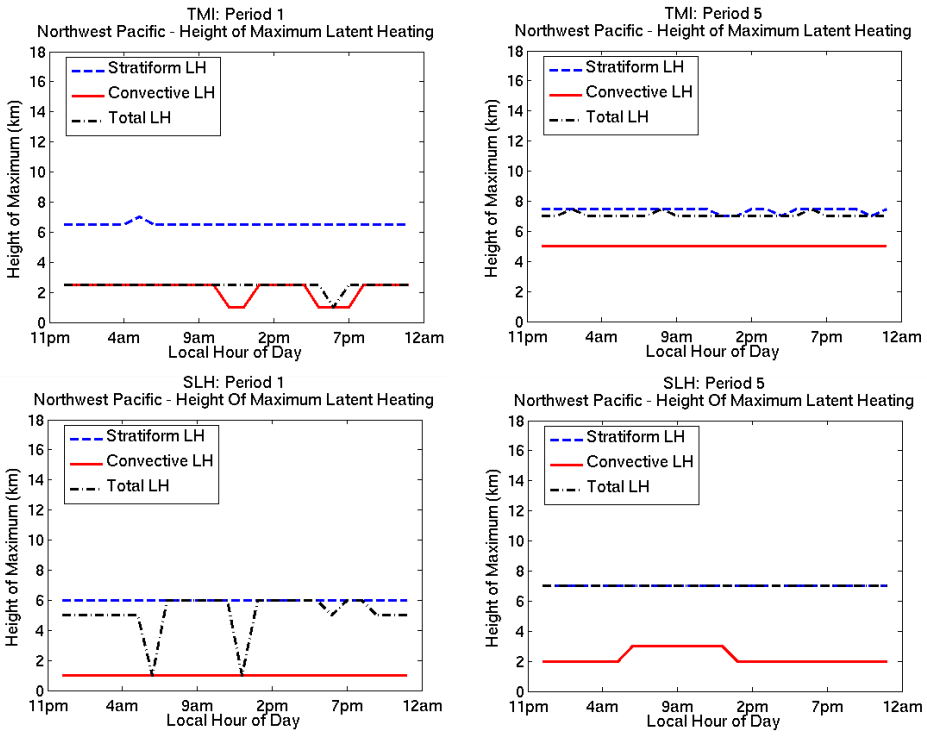

FIGURE E.4: As in Figure A.4 but for the Northwest Pacific region.

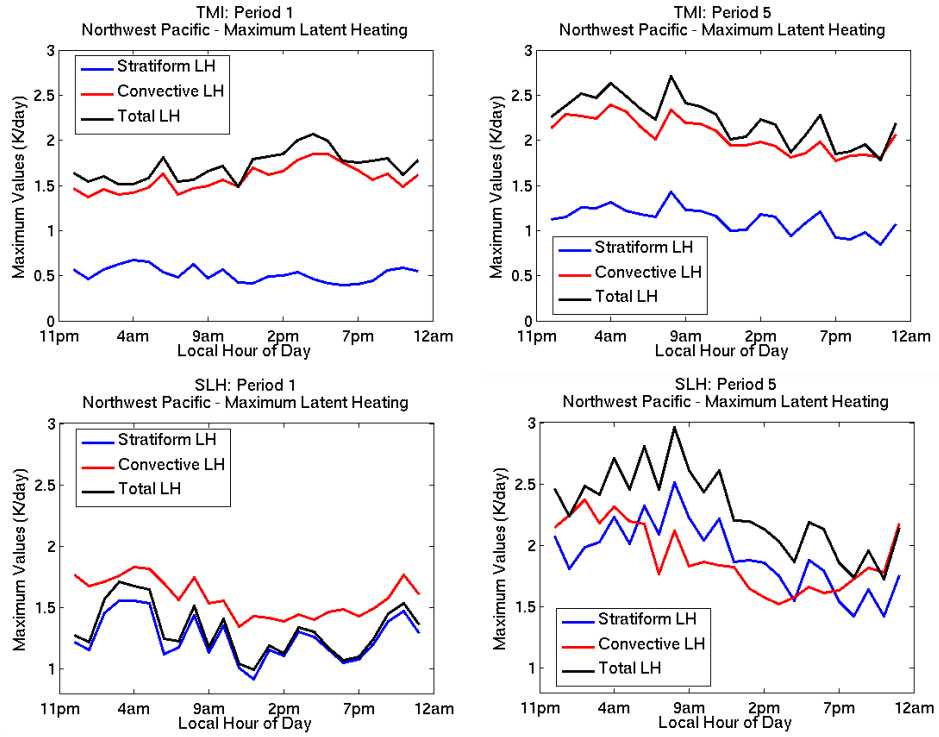

FIGURE E.5: As in Figure A.5 but for the Northwest Pacific region.

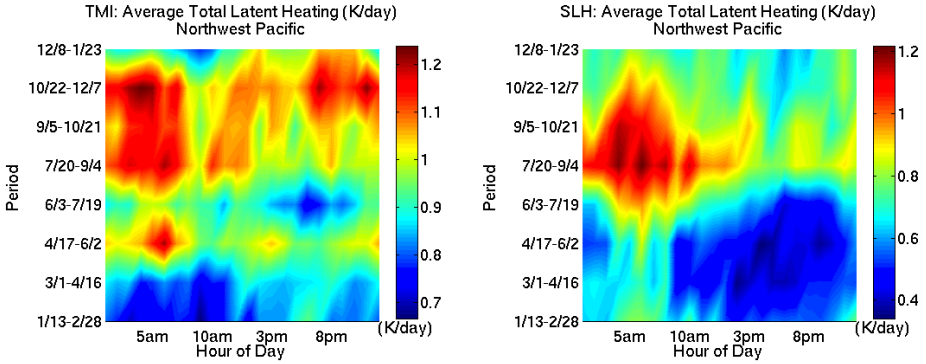

FIGURE E.6: As in Figure A.6 but for the Northwest Pacific region.

Appendix F

Central America

The following plots are all for the Central America boxed region and include 1) Winter and summer diurnal cycle of integrated total latent heating, 2) Winter and summer fourier fits to the diurnal cycle of total integrated latent heating, 3) Seasonal variation of diurnal amplitudes and phases, 4) Winter and summer diurnal cycle of height of maximum latent heating, 5) Winter and summer diurnal cycle of maximum value of latent heating in atmospheric column, and 6) Diurnal and seasonal cycle of integrated total latent heating.

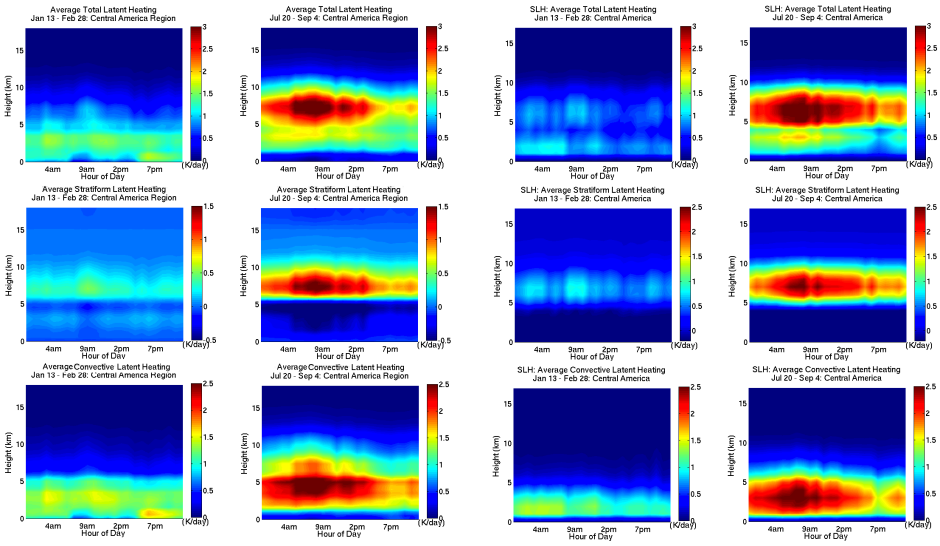

FIGURE F.1: As in Figure A.1 but for the Central America region.

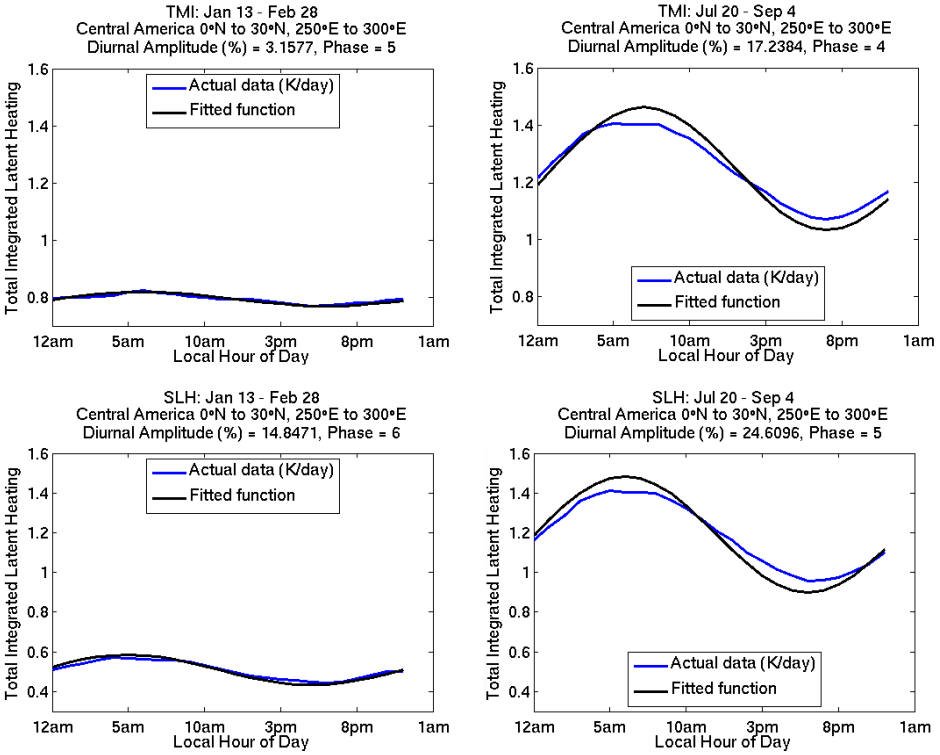

FIGURE F.2: As in Figure A.2 but for the Central America region.

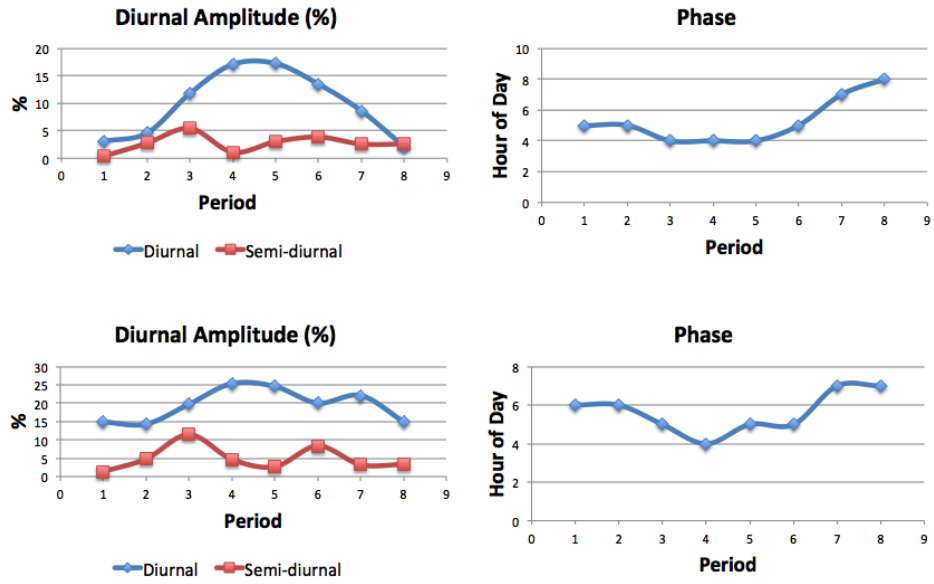

FIGURE F.3: As in Figure A.3 but for the Central America region.

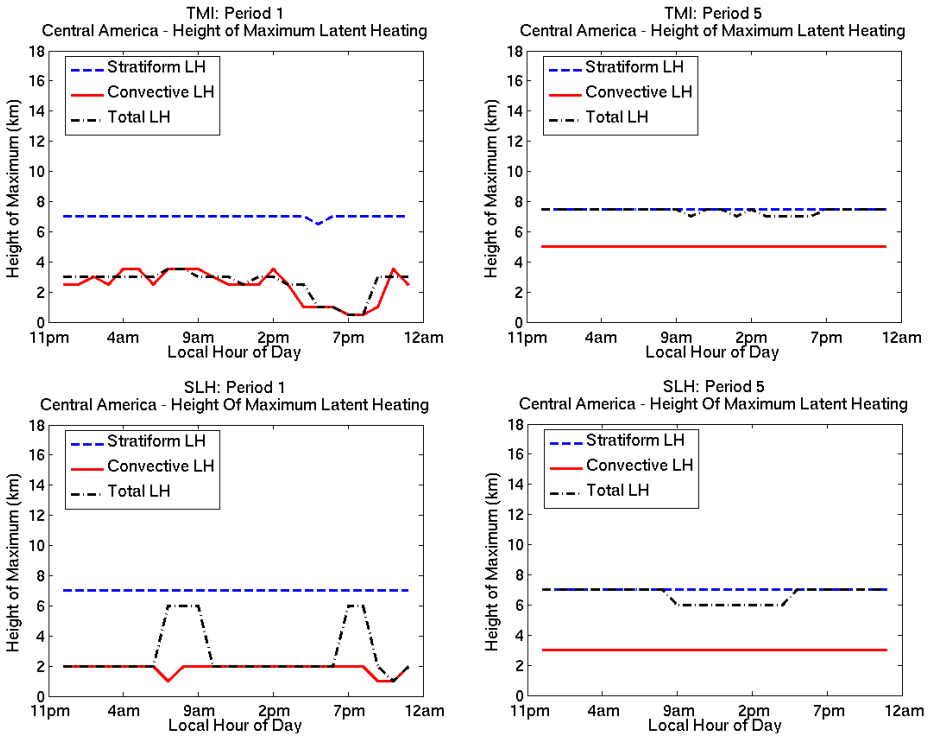

FIGURE F.4: As in Figure A.4 but for the Central America region.

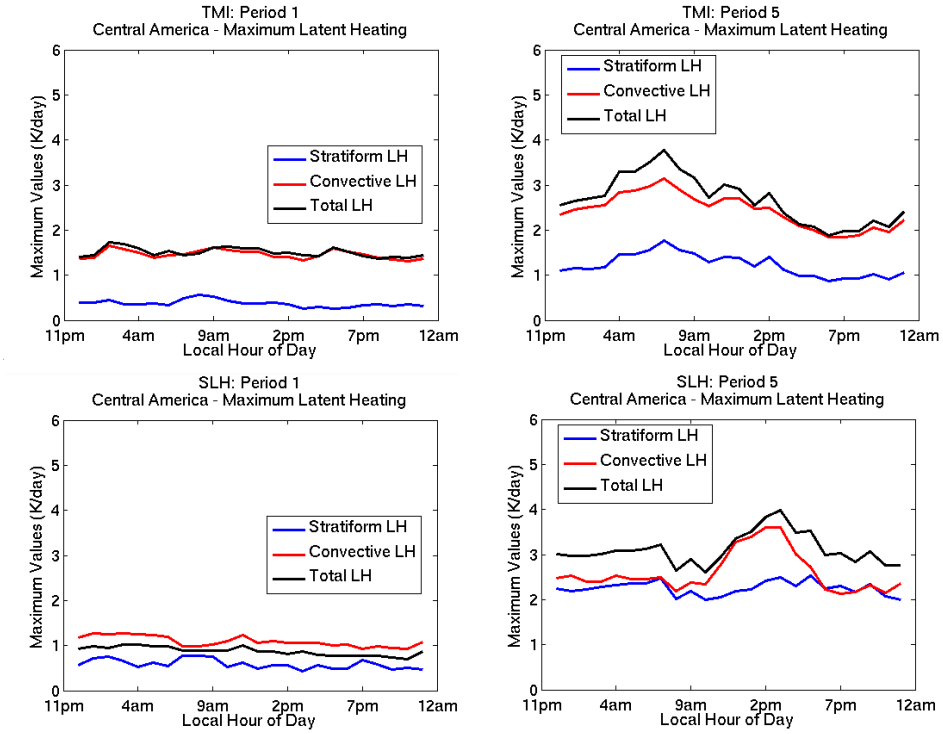

FIGURE F.5: As in Figure A.5 but for the Central America region.

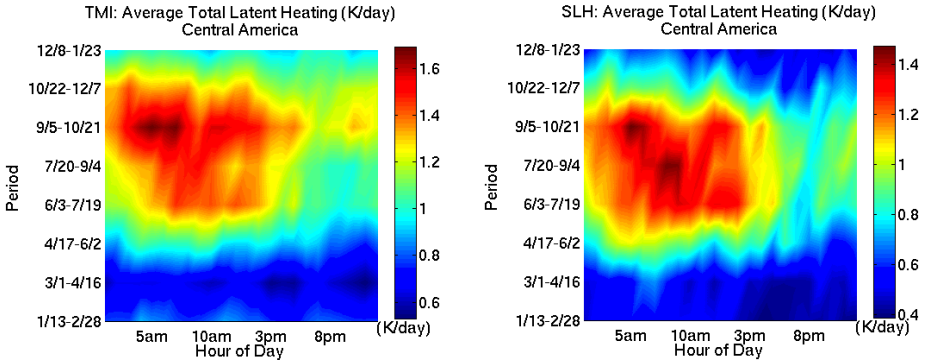

FIGURE F.6: As in Figure A.6 but for the Central America region.

Appendix G

Indian

The following plots are all for the Indian Ocean boxed region and include 1) Winter and summer diurnal cycle of integrated total latent heating, 2) Winter and summer fourier fits to the diurnal cycle of total integrated latent heating, 3) Seasonal variation of diurnal amplitudes and phases, 4) Winter and summer diurnal cycle of height of maximum latent heating, 5) Winter and summer diurnal cycle of maximum value of latent heating in atmospheric column, and 6) Diurnal and seasonal cycle of integrated total latent heating.

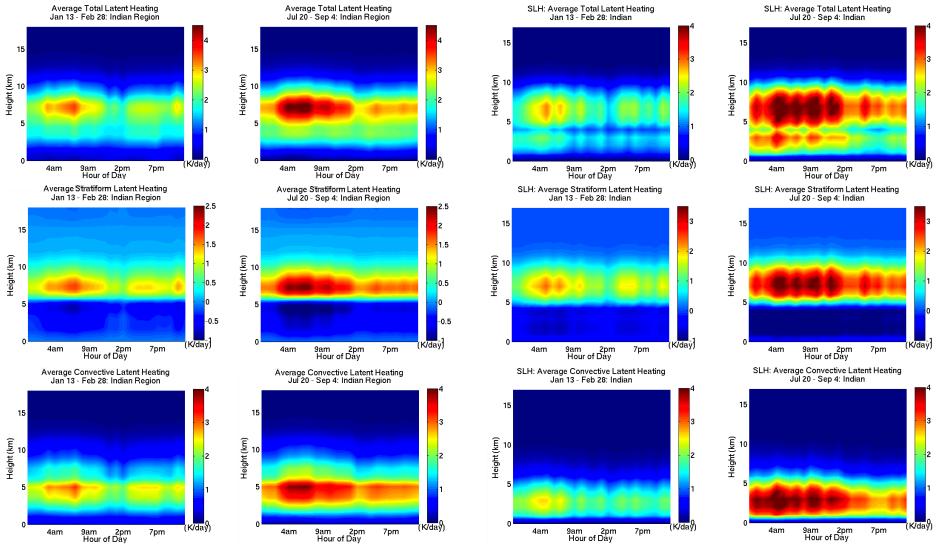

FIGURE G.1: As in Figure A.1 but for the Indian region.

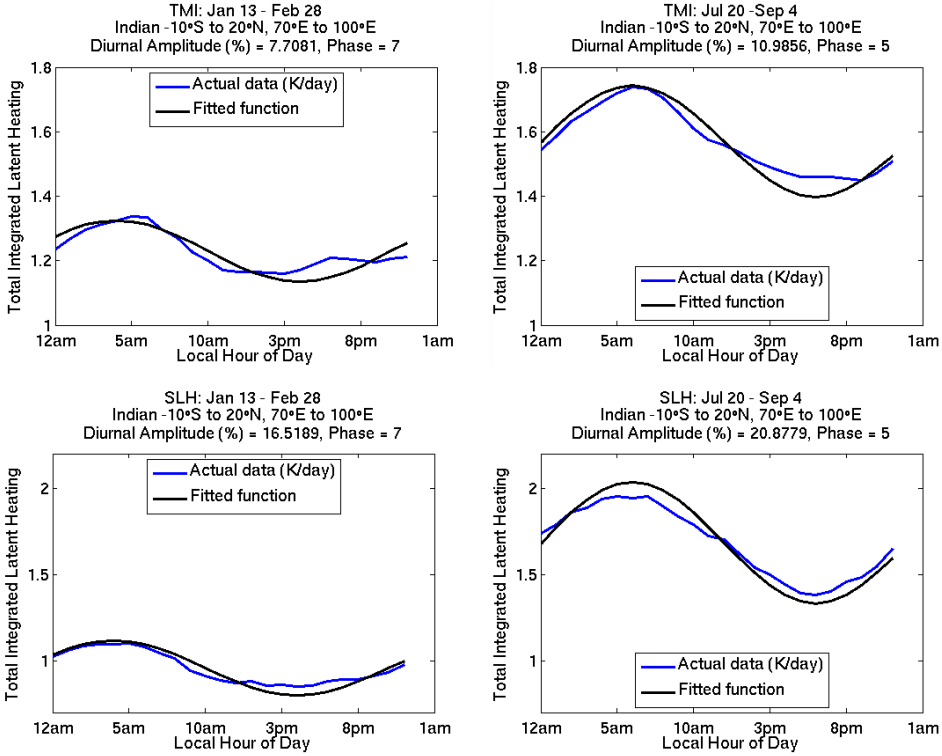

FIGURE G.2: As in Figure A.2 but for the Indian region.

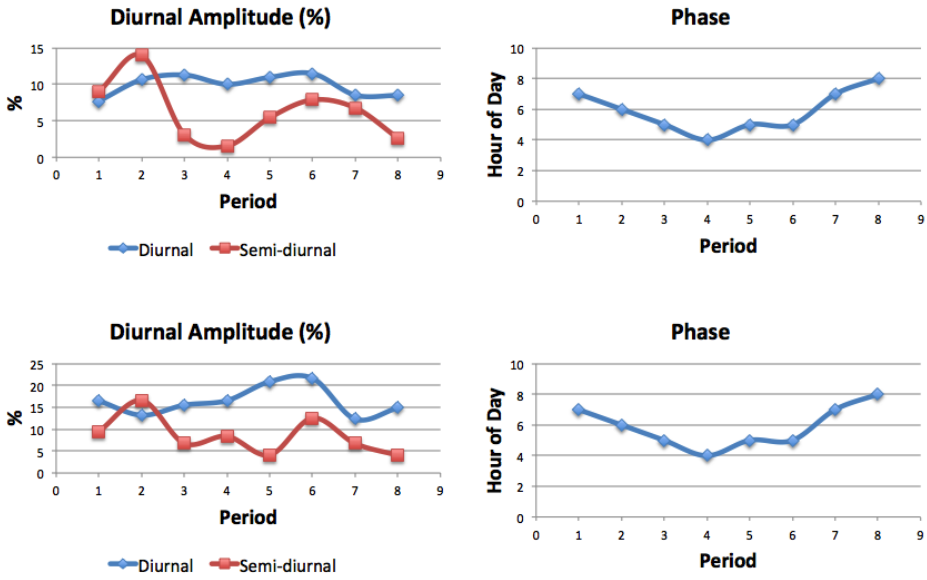

FIGURE G.3: As in Figure A.3 but for the Indian region.

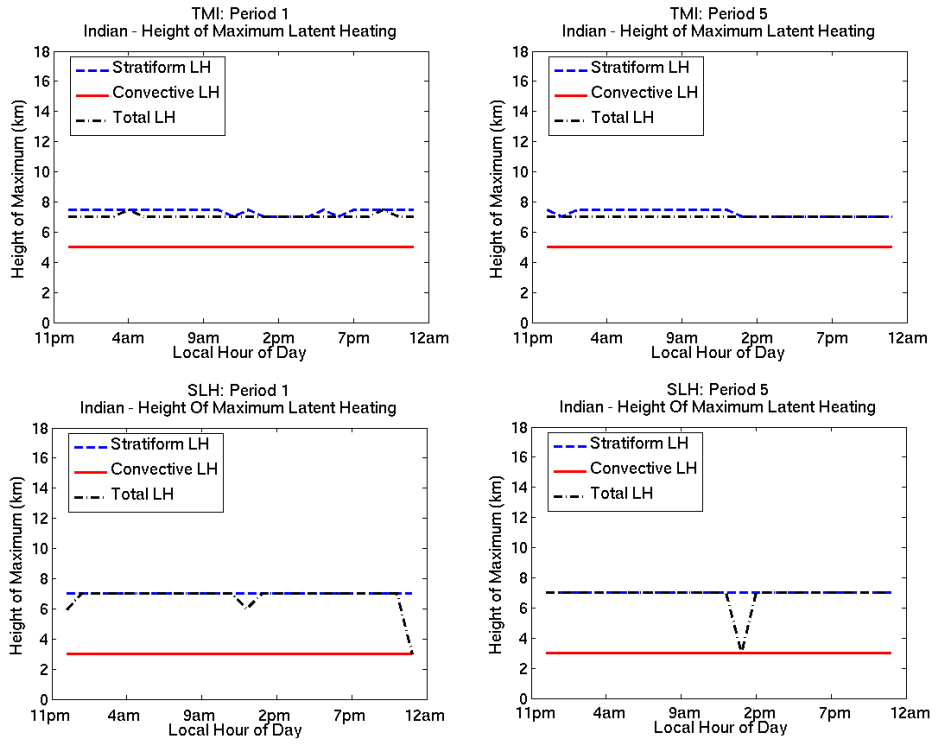

FIGURE G.4: As in Figure A.4 but for the Indian region.

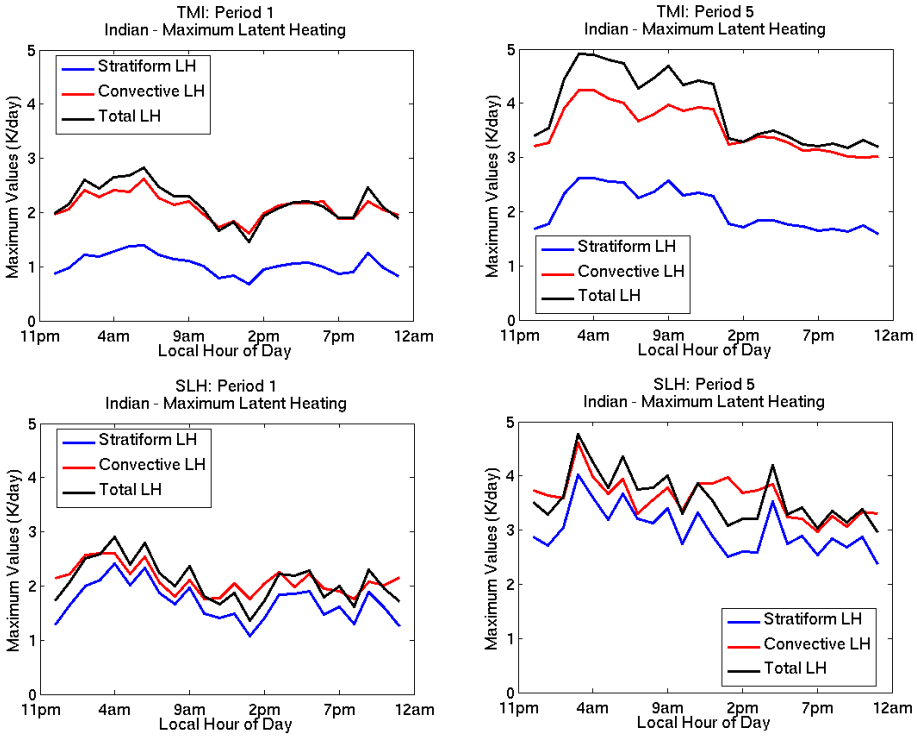

FIGURE G.5: As in Figure A.5 but for the Indian region.

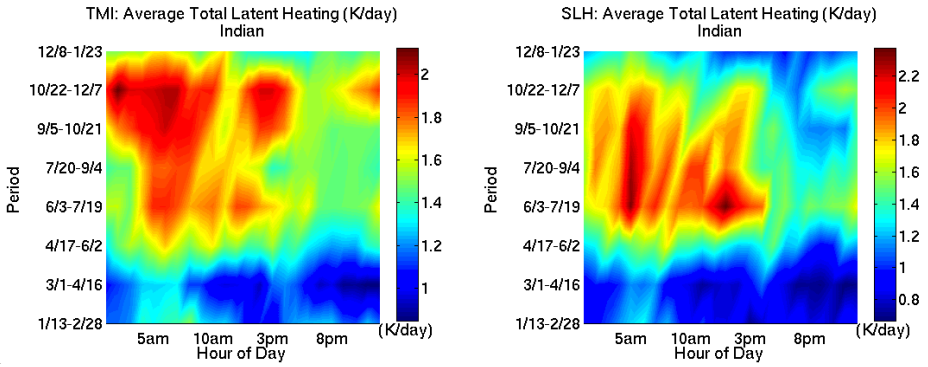

FIGURE G.6: As in Figure A.6 but for the Indian region.

Appendix H

Amazon

* This marks the beginning of land regions

The following plots are all for the Amazon boxed region and include 1) Winter and summer diurnal cycle of integrated total latent heating, 2) Winter and summer fourier fits to the diurnal cycle of total integrated latent heating, 3) Seasonal variation of diurnal amplitudes and phases, 4) Winter and summer diurnal cycle of height of maximum latent heating and maximum value of latent heating in atmospheric column, and 5) Diurnal and seasonal cycle of integrated total latent heating.

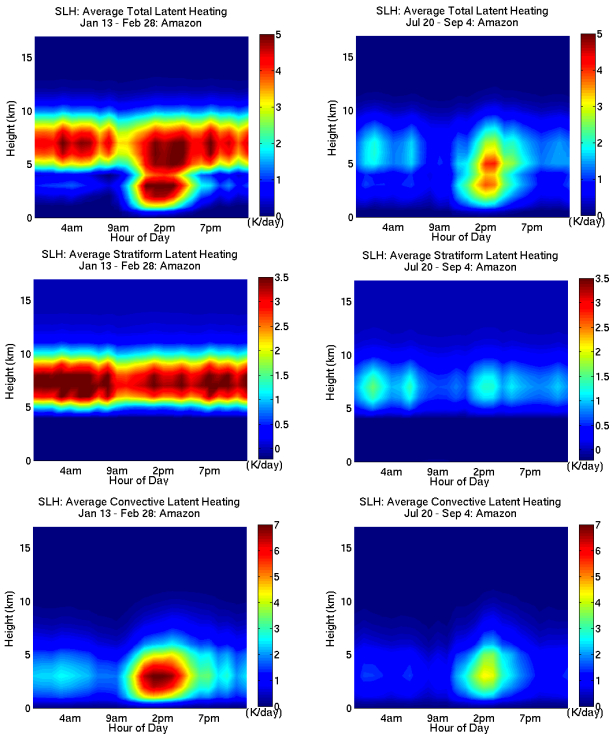

FIGURE H.1: Amazon – 13-year composite of average total *(top)*, stratiform *(middle)*, and convective *(bottom)* vertical latent heating structures in Period 1 and Period 5 for the SLH algorithm *(right)*. Units are in Kelvin per day.

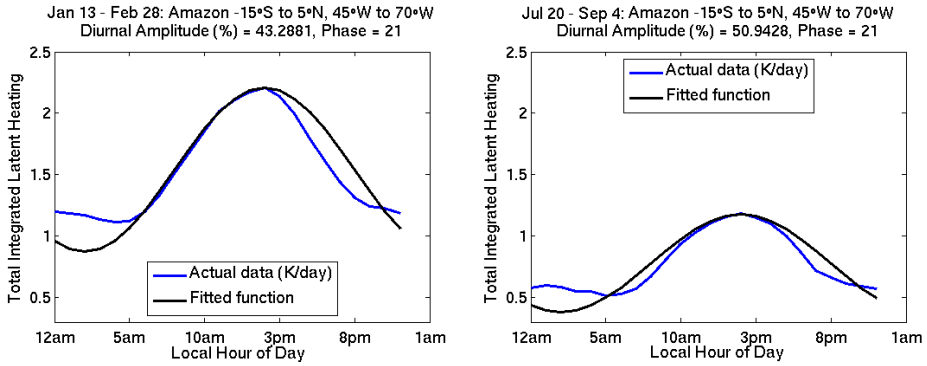

FIGURE H.2: Fourier fit to the diurnal cycle of the SLH integrated heating in the Amazon boxed region for Period 1 *(left)* and Period 5 *(right)*. Actual data is the blue line and the Fourier fit is the black line. Actual data was smoothed in these plots in order to compare to the fit. Included in the title are the latitude and longitude coordinates, the diurnal amplitude percentage, and the phase.

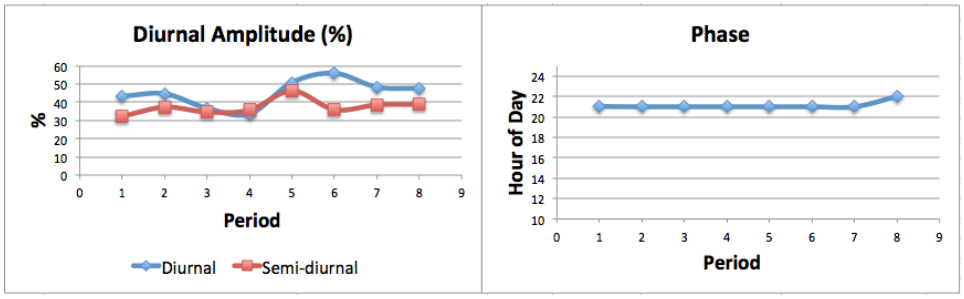

FIGURE H.3: Amazon – Diurnal amplitude percentages and semi-diurnal amplitude percentages *(left)* and phases *(right)* in military time of SLH integrated total heating for each of the eight 47-day periods averaged over 13-year period between 1998 and 2010.

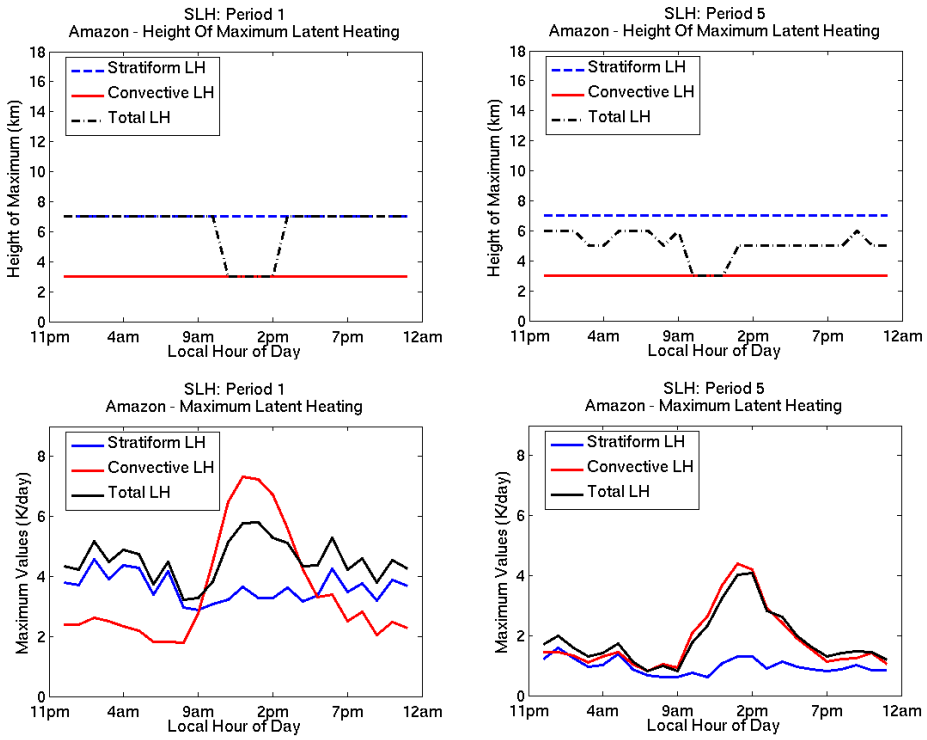

FIGURE H.4: Amazon – Diurnal cycle of height of maximum latent heating (stratiform, convective, and total) *(top)* and maximum values of latent heating (stratiform, convective, and total) through the depth of the atmosphere *(bottom)* for Period 1 *(left)* and Period 5 *(right)* from the SLH algorithm averaged over 13-year period between 1998 and 2010.

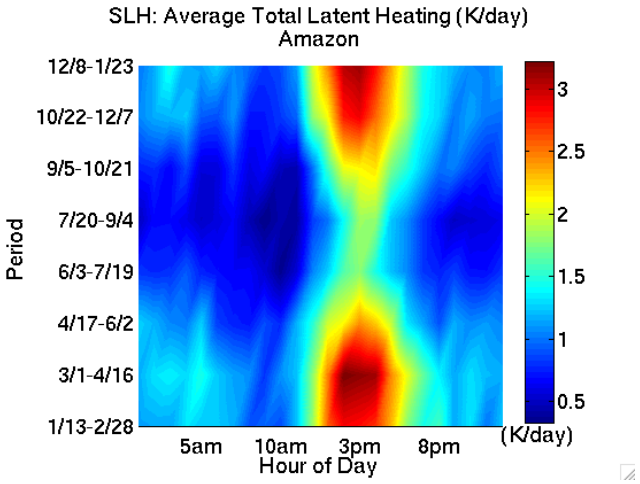

FIGURE H.5: Plots of diurnal cycle and seasonal cycle of integrated total latent heating for the Amazon region from the SLH algorithm with hour of day on the x-axis and seasonal cycle of eight 47-day periods on y-axis.

Appendix I

Congo

The following plots are all for the Congo boxed region and include 1) Winter and summer diurnal cycle of integrated total latent heating, 2) Winter and summer fourier fits to the diurnal cycle of total integrated latent heating, 3) Seasonal variation of diurnal amplitudes and phases, 4) Winter and summer diurnal cycle of height of maximum latent heating and maximum value of latent heating in atmospheric column, and 5) Diurnal and seasonal cycle of integrated total latent heating.

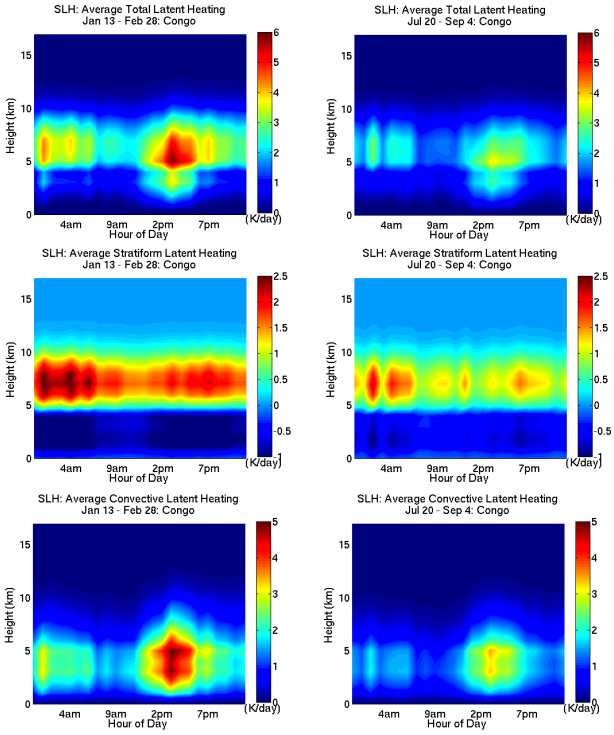

FIGURE I.1: As in Figure H.1 but for the Congo region.

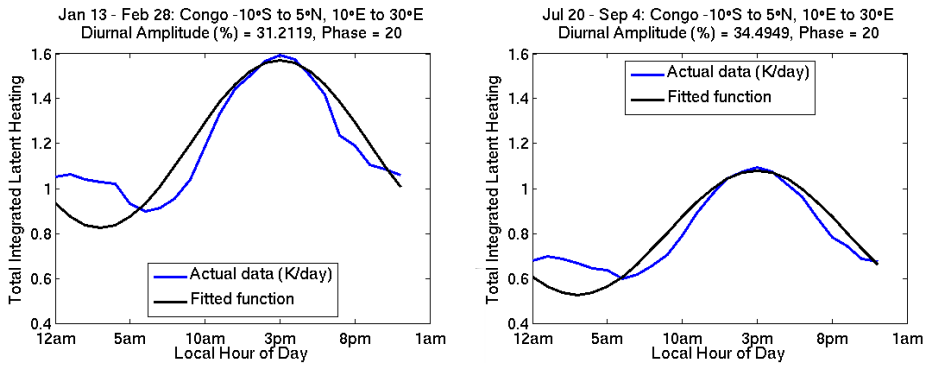

FIGURE I.2: As in Figure H.2 but for the Congo region.

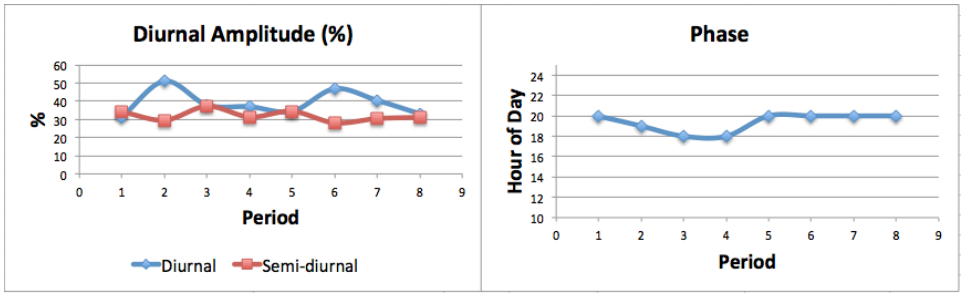

FIGURE I.3: As in Figure H.3 but for the Congo region.

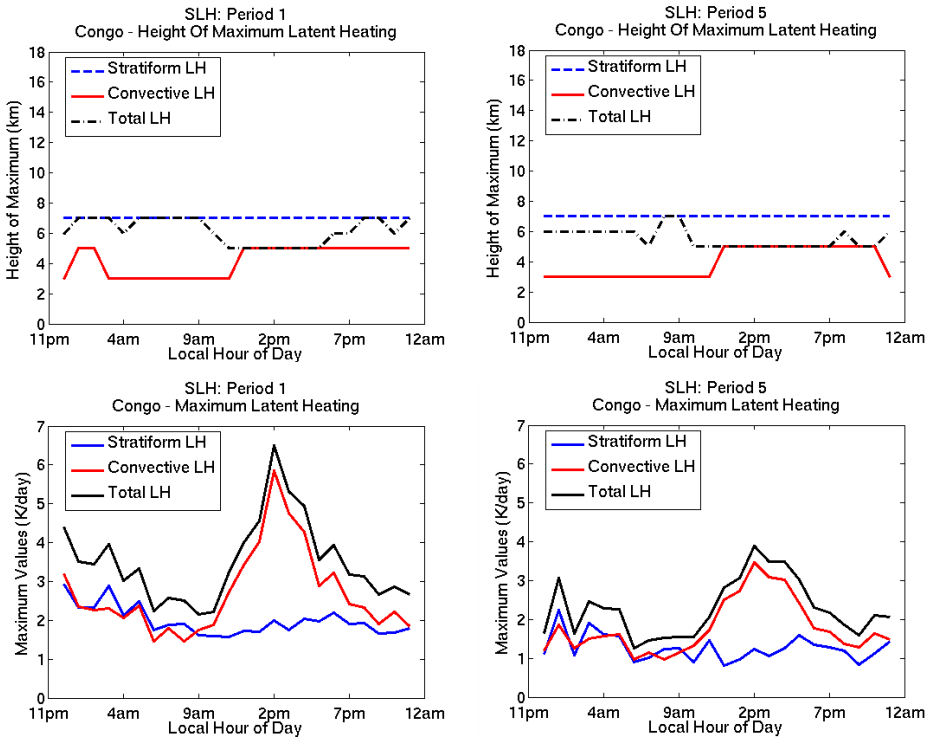

FIGURE I.4: As in Figure H.4 but for the Congo region.

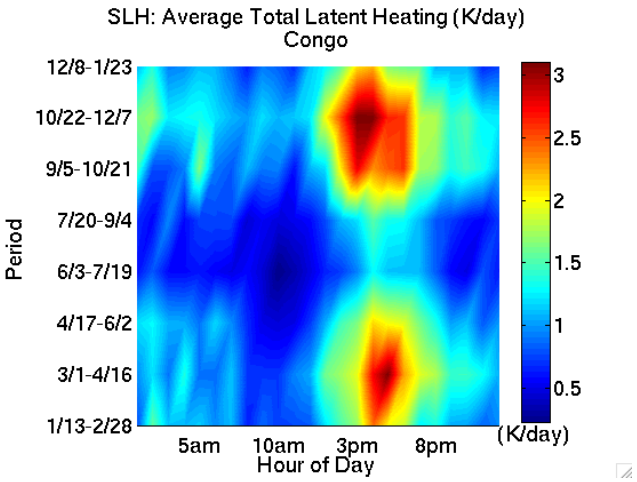

FIGURE I.5: As in Figure H.5 but for the Congo region.

Appendix J

Indian (land)

The following plots are all for the Indian land boxed region and include 1) Winter and summer diurnal cycle of integrated total latent heating, 2) Winter and summer fourier fits to the diurnal cycle of total integrated latent heating, 3) Seasonal variation of diurnal amplitudes and phases, 4) Winter and summer diurnal cycle of height of maximum latent heating and maximum value of latent heating in atmospheric column, and 5) Diurnal and seasonal cycle of integrated total latent heating.

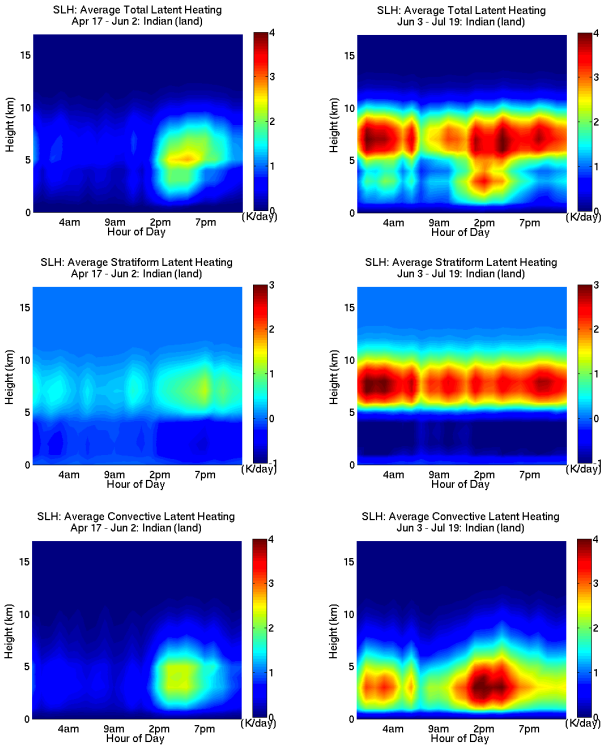

FIGURE J.1: As in Figure H.1 but for the Indian (land) region.

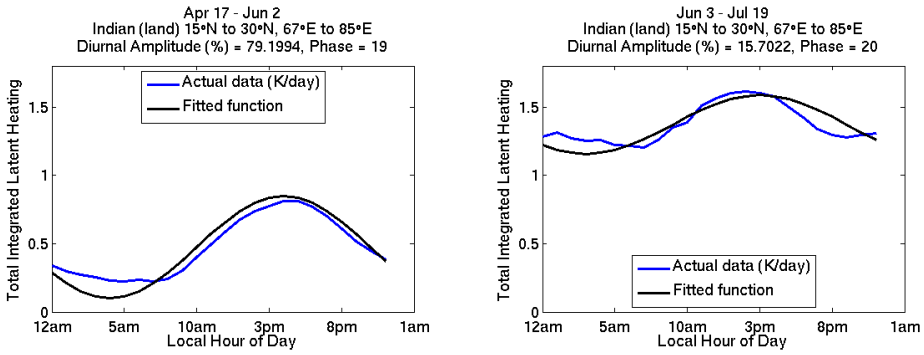

FIGURE J.2: As in Figure H.2 but for the Indian (land) region.

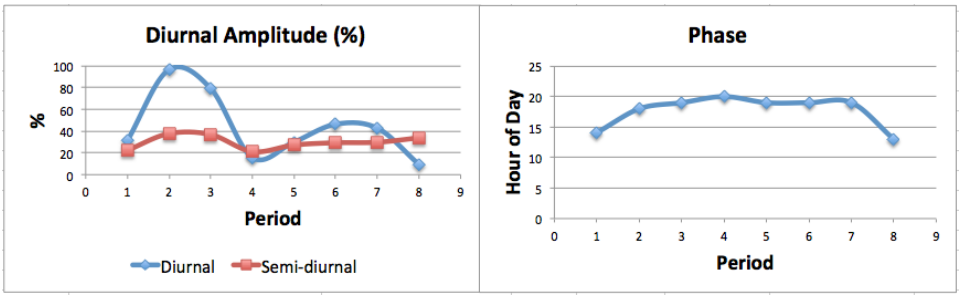

FIGURE J.3: As in Figure H.3 but for the Indian (land) region.

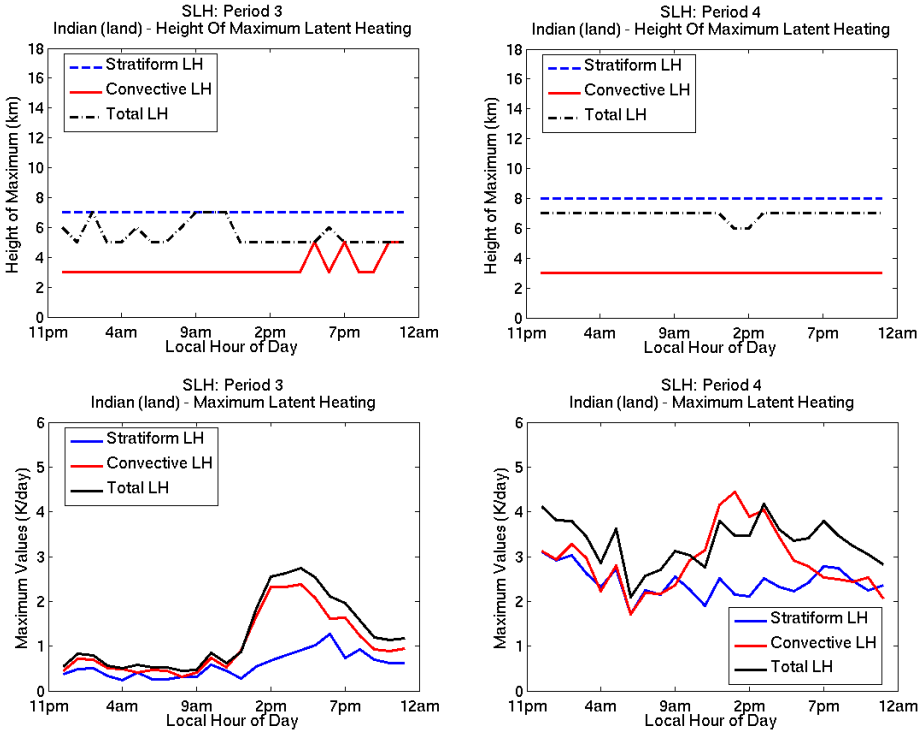

FIGURE J.4: As in Figure H.4 but for the Indian (land) region.

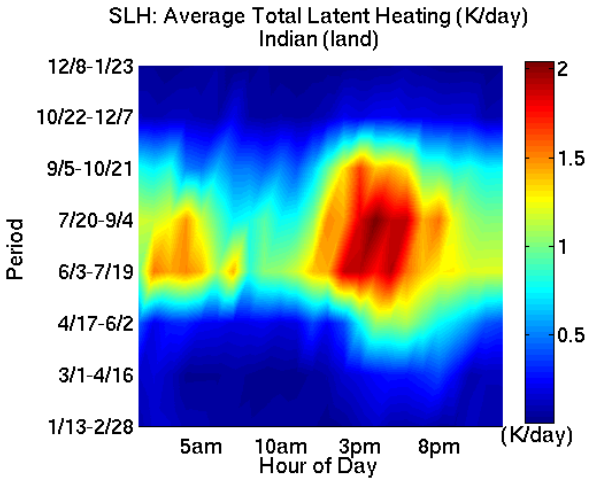

FIGURE J.5: As in Figure H.5 but for the Indian (land) region.

Bibliography

, 2006: Trmm (tropical rainfall measuring mission). URL http://trmm.gsfc.nasa.gov/education_dir/education.html, URL http://trmm.gsfc.nasa.gov/education_dir/education.html.

, 2011: Trmm microwave imager (tmi). URL http://pmm.nasa.gov/node/161, URL http://pmm.nasa.gov/node/161.

Berg, W., C. Kummerow, and C. Morales, 2002: Differences between east and west pacific rainfall systems. *Journal of Climate*, **15**, 3659–3672, doi:http://dx.doi.org/10.1175/1520-0442(2002)015<3659:DBEAWP>2.0.CO;2, URL http://journals.ametsoc.org/doi/pdf/10.1175/1520-0442%282002%29015%3C3659%3ADBEAWP%3E2.0.CO%3B2.

Berg, W., T. L'Ecuyer, and C. Kummerow, 2006: Rainfall climate regimes: The relationship of regional trmm rainfall biases to the environment. *Journal of Climate and Applied Meteorology*, **45**, 434–454, doi:http://dx.doi.org/10.1175/JAM2331.1, URL http://journals.ametsoc.org/doi/pdf/10.1175/JAM2331.1.

Choudhury, A. and R. Krishnan, 2011: Dynamical response of the south asian monsoon trough to latent heating from stratiform and convective precipitation. *Journal of Atmospheric Sciences*, **68**, 1347–1363, doi:http://dx.doi.org/10.1175/2011JAS3705.1, URL http://journals.ametsoc.org/doi/pdf/10.1175/2011JAS3705.1.

Clayson, C. and A. Bogdanoff, 2013: The effect of diurnal sea surface temperature warming on climatological air-sea fluxes. *Journal of Climate*, **24**, 2546–2556, doi:http://dx.doi.org/10.1175/JCLI-D-12-00062.1, URL http://journals.ametsoc.org/doi/pdf/10.1175/JCLI-D-12-00062.1.

DeMoss, J. and K. Bowman, 2007: Changes in trmm rainfall due to the orbit boost estimated from buoy rain gauge data. *Journal of Atmospheric and Oceanic Technology*, **24**, 1598–1607, doi:http://dx.doi.org/10.1175/JTECH2082.1, URL http://journals.ametsoc.org/doi/pdf/10.1175/JTECH2082.1.

Eastman, R. and S. Warren, 2014: Diurnal cycles of cumulus, cumulonimbus, stratus, stratocumulus, and fog from surface observations over land and ocean. *Journal of Climate*, **27**, 2386–2404, doi:http://dx.doi.org/10.1175/JCLI-D-13-00352.1, URL http://journals.ametsoc.org/doi/pdf/10.1175/JCLI-D-13-00352.1.

Foster, M. and A. Heidinger, 2013: Patmos-x: Results from a diurnally corrected 30-yr satellite cloud climatology. *Journal of Climate*, **26**, 414–425, doi:http://dx.doi.org/10.1175/JCLI-D-11-00666.1, URL http://journals.ametsoc.org/doi/pdf/10.1175/JCLI-D-11-00666.1.

Grecu, M. and W. Olston, 2006: Bayesian estimation of precipitation from satellite passive microwave observations using combined radar–radiometer retrievals. *Journal of Applied Meteorology and Climatology*, **45**, 416–433, doi:http://dx.doi.org/10.1175/JAM2360.1, URL http://journals.ametsoc.org/doi/pdf/10.1175/JAM2360.1.

Grecu, M., W. Olston, C. Shie, T. L'Ecuyer, and W. Tao, 2009: Combining satellite microwave radiometer and radar observations to estimate atmospheric heating profiles. *Journal of Climate*, **22**, 6356–6376, doi:http://dx.doi.org/10.1175/2009JCLI3020.1, URL http://journals.ametsoc.org/doi/pdf/10.1175/2009JCLI3020.1.

Hartmann, D., H. Hendon, and R. Houze, 1984: Some implications of the mesoscale circulations in tropical cloud clusters for large-scale dynamics and climate. *Journal of Atmospheric Sciences*, **41**, 113–121, doi:http://dx.doi.org/10.1175/1520-0469(1984)041<0113:SIOTMC>2.0.CO;2, URL http://journals.ametsoc.org/doi/pdf/10.1175/1520-0469%281984%29041%3C0113%3ASIOTMC%3E2.0.CO%3B2.

Hou, A., et al., 2014: The global precipitation measurement mission. *Bulletin of the American Meteorological Society*, **95**, 701–722, doi:http://dx.doi.org/10.1175/BAMS-D-13-00164.1, URL http://journals.ametsoc.org/doi/pdf/10.1175/BAMS-D-13-00164.1.

Jakob, C. and C. Schumacher, 2008: Precipitation and latent heating characteristics of the major tropical western pacific cloud regimes. *Journal of Climate*, **21**, 4348–4364, doi:http://dx.doi.org/10.1175/2008JCLI2122.1, URL http://journals.ametsoc.org/doi/pdf/10.1175/2008JCLI2122.1.

Jiang, X. and coauthors, 2009: Structures associated with the mjo as characterized by trmm estimates, ecmwf reanalyses, and forecasts: A case study during 1998/99 winter. *Journal of Climate*, **22**, 6001–6020, doi:http://dx.doi.org/10.1175/2009JCLI3048.1, URL http://journals.ametsoc.org/doi/pdf/10.1175/2009JCLI3048.1.

Kummerow, C. and coauthors, 2000: The status of the tropical rainfall measuring mission (trmm) after two years in orbit. *Journal of Applied Meteorology*, **39**, 1965–1982, doi:http://dx.doi.org/10.1175/1520-0450(2001)040<1965:TSOTTR>2.0.CO;2, URL http://journals.ametsoc.org/doi/pdf/10.1175/1520-0450%282001%29040%3C1965%3ATSOTTR%3E2.0.CO%3B2.

Lau, K.-M. and L. Peng, 1987: Origin of low-frequency (intraseasonal) oscillations in the tropical atmosphere. part i: Basic theory. *Journal of Atmospheric Science*, **44**, 950–972, doi:http://dx.doi.org/10.1175/1520-0469(1987)044<0950:OOLFOI>2.0.CO;2, URL http://journals.ametsoc.org/doi/pdf/10.1175/1520-0469%281987%29044%3C0950%3AOOLFOI%3E2.0.CO%3B2.

L'Ecuyer, T., H. Masunaga, and C. Kummerow, 2006: Variability in the characteristics of precipitation systems in the tropical pacific. *Journal of Climate*, **19**, 1388–1406, doi:http://dx.doi.org/10.1175/JCLI3698.1, URL http://journals.ametsoc.org/doi/pdf/10.1175/JCLI3698.1.

L'Ecuyer, T. and G. McGarragh, 2010: A 10-year climatology of tropical radiative heating and its vertical structure from trmm observations. *Journal of Climate*, **23**, 519–541, doi:http://dx.doi.org/10.1175/2009JCLI3018.1, URL http://journals.ametsoc.org/doi/pdf/10.1175/2009JCLI3018.1.

L'Ecuyer, T. and G. Stephens, 2002: An uncertainty model for bayesian monte carlo retrieval algorithms: Application to the trmm observing system.

Quarterly Journal of the Royal Meteorological Society, **128**, 1713–1737, doi:10.1002/qj.200212858316, URL http://onlinelibrary.wiley.com/doi/10.1002/qj.200212858316/pdf.

L'Ecuyer, T. and G. Stephens, 2003: The tropical oceanic energy budget from the trmm perspective. part i: Algorithm and uncertainties. *Journal of Climate*, **16**, 1967.

L'Ecuyer, T. and G. Stephens, 2007: The tropical atmospheric energy budget from the trmm perspective. part ii: Evaluating gcm representations of the sensitivity of regional energy and water cycles to the 1998–99 enso cycle. *Journal of Climate*, **20**, 4548–4571, doi:http://dx.doi.org/10.1175/JCLI4207.1, URL http://journals.ametsoc.org/doi/pdf/10.1175/JCLI4207.1.

Ling, J. and C. Zhang, 2013: Diabatic heating profiles in recent global reanalyses. *Journal of Climate*, **26**, 3307–3325, doi:http://dx.doi.org/10.1175/JCLI-D-12-00384.1, URL http://journals.ametsoc.org/doi/pdf/10.1175/JCLI-D-12-00384.1.

Masunaga, H. and T. L'Ecuyer, 2011: Equatorial asymmetry of the east pacific itcz: Observational constraints on the underlying processes. *Journal of Climate*, **24**, 1784–1800, doi:http://dx.doi.org/10.1175/2010JCLI3854.1, URL http://journals.ametsoc.org/doi/pdf/10.1175/2010JCLI3854.1.

Negri, A., T. Bell, and X. Liming, 2002: Sampling of the diurnal cycle of precipitation using trmm. *Journal of Atmospheric and Oceanic Technology*, **19**, 1333–1344, doi:http://dx.doi.org/10.1175/1520-0426(2002)019<1333:SOTDCO>2.0.CO;2, URL http://journals.ametsoc.org/doi/pdf/10.1175/1520-0426%282002%29019%3C1333%3ASOTDCO%3E2.0.CO%3B2.

Nesbitt, S. and E. Zipser, 2003: The diurnal cycle of rainfall and convective intensity according to three years of trmm measurements. *Journal of Climate*, **16**, 1456–1475, URL http://journals.ametsoc.org/doi/pdf/10.1175/1520-0442%282003%29016%3C1456%3ATDCORA%3E2.0.CO%3B2.

Reihl, H. and J. Malkus, 1958: On the heat balance in the equatorial trough zone. 503–537, URL http://snow.atm.ncu.edu.tw/TC/RiehlMalkus1958.pdf.

Schumacher, C., R. Houze, and I. Kraucunas, 2004: The tropical dynamical response to latent heating estimates derived from the trmm precipitation radar. *Journal of Atmospheric Sciences*, **61**, 1341–1358, doi:http://dx.doi.org/10.1175/1520-0469(2004)061<1341:TTDRTL>2.0.CO;2, URL http://journals.ametsoc.org/doi/pdf/10.1175/1520-0469%282004%29061%3C1341%3ATTDRTL%3E2.0.CO%3B2.

Shige, S., Y. Takayabu, W. Tao, and C. Shie, 2007: Spectal retrieval of latent heating profiles from trmm pr data. part ii: Algorithm improvement and heating estimates over tropical ocean regions. *Journal of Applied Meteorology*, **46**, 1098–1124, doi:http://dx.doi.org/10.1175/JAM2510.1, URL http://journals.ametsoc.org/doi/pdf/10.1175/JAM2510.1.

Simpson, J., R. Alder, and G. North, 1988: A proposed tropical rainfall measuring mission. *Bulletin of the American Meteorological Society*, **69**, 278–295, doi:http://dx.doi.org/10.1175/1520-0477(1988)069<0278:APTRMM>2.0.CO;2, URL http://journals.ametsoc.org/doi/pdf/10.1175/1520-0477%281988%29069%3C0278%3AAPTRMM%3E2.0.CO%3B2.

Su, H., J. Jiang, D. Vane, and G. Stephens, 2008: Observed vertical structure of tropical oce.anic clouds sorted in large-scale regimes. *Geophysical Research Letters*, **35 (24.L24704)**, doi:10.1029/2008GL035888.

Tao, W., et al., 2001: Retrieved vertical profiles of latent heat release using trmm rainfall products for february 1988. *Journal of Applied Meteorology*, **40 (6)**, 957–982, URL http://journals.ametsoc.org/doi/pdf/10.1175/1520-0450%282001%29040%3C0957%3ARVPOLH%3E2.0.CO%3B2.

Tao, W.-K. and coauthors, 2006: Retrieval of latent heating from trmm measurements. *Bulletin of the American Meteorological Society*, **87**, 1555–1572, doi:http://dx.doi.org/10.1175/BAMS-87-11-1555, URL http://journals.ametsoc.org/doi/pdf/10.1175/BAMS-87-11-1555.

Tao, W.-K., J. Simpson, C. Sui, B. Ferrier, S. Lang, J. Scala, M. Chou, and K. Pickering, 1993: Heating, moisture, and water budgets of tropical and midlatitude squall lines: Comparisons and sensitivity to longwave radiation. *Journal of Atmospheric Sciences*, **50**, 673–690, doi:http://dx.doi.org/10.1175/1520-0469(1993)050<0673:HMAWBO>2.0.CO;2,

URL http://journals.ametsoc.org/doi/pdf/10.1175/1520-0469%281993%29050%3C0673%3AHMAWBO%3E2.0.CO%3B2.

Taylor, P., 2012: Tropical outgoing longwave radiation and longwave cloud forcing diurnal cycles from ceres. *Journal of Atmospheric Sciences*, **69**, 3652–3669, doi:http://dx.doi.org/10.1175/JAS-D-12-088.1, URL http://journals.ametsoc.org/doi/pdf/10.1175/JAS-D-12-088.1.

* (NEWS Q1 dataset): Atmospheric diabatic heating estimates were generated under the support of the NASA NEWS program (Grecu and Olston, 2006, Grecu et al., 2009, L'Ecuyer and McGarragh, 2010, L'Ecuyer and Stephens, 2003, 2007)